The mechanical behaviour and failure modes of volcanic rocks: a review

Michael Heap, Marie E.S. Violay

To cite this version:

Michael Heap, Marie E.S. Violay. The mechanical behaviour and failure modes of volcanic rocks: a review. Bulletin of Volcanology, 2021, 83 (5), pp.33. 10.1007/s00445-021-01447-2 . hal-03547456

Bulletin of Volcanology (2021) 83: 33
https://doi.org/10.1007/s00445-021-01447-2

REVIEW ARTICLE

The mechanical behaviour and failure modes of volcanic rocks: a review

Michael J. Heap[1] · **Marie E.S. Violay**[2]

Received: 25 November 2020 / Accepted: 2 March 2021 / Published online: 13 April 2021

Abstract

The microstructure and mineralogy of volcanic rocks is varied and complex, and their mechanical behaviour is similarly varied and complex. This review summarises recent developments in our understanding of the mechanical behaviour and failure modes of volcanic rocks. Compiled data show that, although porosity exerts a first-order influence on the uniaxial compressive strength of volcanic rocks, parameters such as the partitioning of the void space (pores and microcracks), pore and crystal size and shape, and alteration also play a role. The presence of water, strain rate, and temperature can also influence uniaxial compressive strength. We also discuss the merits of micromechanical models in understanding the mechanical behaviour of volcanic rocks (which includes a review of the available fracture toughness data). Compiled data show that the effective pressure required for the onset of hydrostatic inelastic compaction in volcanic rocks decreases as a function of increasing porosity, and represents the pressure required for cataclastic pore collapse. Differences between brittle and ductile mechanical behaviour (stress-strain curves and the evolution of porosity and acoustic emission activity) from triaxial deformation experiments are outlined. Brittle behaviour is typically characterised by shear fracture formation, and an increase in porosity and permeability. Ductile deformation can either be distributed (cataclastic pore collapse) or localised (compaction bands) and is characterised by a decrease in porosity and permeability. The available data show that tuffs deform by delocalised cataclasis and extrusive volcanic rocks develop compaction bands (planes of collapsed pores connected by microcracks). Brittle failure envelopes and compactive yield caps for volcanic rocks are compared, highlighting that porosity exerts a first-order control on the stresses required for the brittle-ductile transition and shear-enhanced compaction. However, these data cannot be explained by porosity alone and other microstructural parameters, such as pore size, must also play a role. Compactive yield caps for tuffs are elliptical, similar to data for sedimentary rocks, but are linear for extrusive volcanic rocks. Linear yield caps are considered to be a result of a high pre-existing microcrack density and/or a heterogeneous distribution of porosity. However, it is still unclear, with the available data, why compaction bands develop in some volcanic rocks but not others, which microstructural attributes influence the stresses required for the brittle-ductile transition and shear-enhanced compaction, and why the compactive yield caps of extrusive volcanic rocks are linear. We also review the Young's modulus, tensile strength, and frictional properties of volcanic rocks. Finally, we review how laboratory data have and can be used to improve our understanding of volcanic systems and highlight directions for future research. A deep understanding of the mechanical behaviour and failure modes of volcanic rock can help refine and develop tools to routinely monitor the hazards posed by active volcanoes.

Keywords Volcanic rock · Brittle · Ductile · Uniaxial compressive strength · Tensile strength · Coefficient of friction · Strain localisation

---

Editorial responsibility: U. Kueppers

✉ Michael J. Heap
heap@unistra.fr

✉ Marie E.S. Violay
marie.violay@epfl.ch

[1] Université de Strasbourg, CNRS, Institut Terre et Environnement de Strasbourg, UMR 7063, 5 rue René Descartes, F-67084 Strasbourg, France

[2] École Polytechnique Fédérale de Lausanne (EPFL), Faculté de l'Environnement Naturel, Architectural et Construit (ENAC), Laboratory of Experimental Rock Mechanics (LEMR), Station 18, CH-1015 Lausanne, Switzerland

Introduction

Compared to granite and porous sedimentary rocks, our understanding of the mechanical behaviour and failure modes of volcanic rocks is underdeveloped. One of the main reasons behind this knowledge discrepancy is that discussion and collaboration between the rock deformation and volcanological communities only began in earnest about a decade ago (although we highlight the pioneering early work by Shimada 1986; Shimada et al. 1989; Shimada 2000). Early studies on granite were geared towards understanding earthquakes (e.g. Brace et al. 1966; Byerlee 1967; Scholz 1968; Zoback and Byerlee 1975), as granite was considered a volumetrically important crustal rock, and more recent studies focussed on porous sedimentary rocks (e.g. Menéndez et al. 1996; Wong et al. 1997; Baud et al. 2004) were prompted by their importance as reservoir rocks.

Understanding the mechanical behaviour and failure modes of volcanic rocks represents a significant challenge due to the immense variability of volcanic rocks in terms of, for example, mineralogical composition, porosity, and microstructure (e.g. pore size and shape, crystal size and shape, crystal content, presence of microcracks, presence of glass, alteration) (e.g. Toramaru 1990; Blower et al. 2003; Wright et al. 2009; Shea et al. 2010; Voltolini et al. 2011; Colombier et al. 2017; Cashman 2020). The challenge presented by volcanic rocks is exemplified by a simple comparison between the microstructure of a typical sandstone used in studies of rock deformation (Bentheim sandstone, Germany; Fig. 1a; Louis et al. 2007) and that of a typical extrusive volcanic rock (andesite from Volcán de Colima, Mexico; Fig. 1b; Heap et al. 2020a). The sandstone, which contains 99% quartz and has a porosity of 0.23 and a grain size of 50–500 µm, has a very homogeneous microstructure in comparison to the andesite, which is characterised by heterogeneously distributed pores of different sizes and shapes and phenocrysts of different types, sizes, and shapes (Fig. 1).

The rewards of a deep understanding of the mechanical behaviour and failure modes of volcanic rock include the development or refinement of models designed to, for example, assess volcanic dome or flank stability (e.g. van Wyk de Vries and Francis 1997; Watters et al. 2000; Okubo 2004; Apuani et al. 2005; del Potro and Hürlimann 2008; Rodríguez-Losada et al. 2009; Borselli et al. 2011; Schaefer et al. 2013), the collapse of which can result in the generation of pyroclastic density currents that can be costly both economically and in terms of loss of life (e.g. Glicken 1996; Komorowski et al. 2013; Cole et al. 2015). Following failure, the flow velocity and maximum distance obtained by a volcanic debris avalanche can depend on the frictional properties of volcanic rocks (e.g. Legros et al. 2000; Hürlimann et al. 2000; Brodsky et al. 2003; Sosio et al. 2012; Bernard and van Wyk de Vries 2017; Peruzzetto et al. 2019; Hughes et al. 2020). Laboratory-measured values of tensile strength can inform on the magma overpressures required for intrusion/eruption (e.g. Gudmundsson 2011, 2020). The mechanical properties (e.g. Young's modulus) of volcanic rock layers are also required for models that study dyke and fracture arrest/propagation (e.g. Gudmundsson 2002; Geshi et al. 2012; Forbes Inskip et al. 2020; Gudmundsson 2020) and elastic analytical solutions and numerical models widely used in volcanology to interpret surface ground deformation (e.g. Heap et al. 2020b). Data from deformation experiments performed on volcanic rock can help construct strength profiles for the oceanic crust (e.g. Violay et al. 2012, 2015a) and volcanic edifices (e.g. Bakker et al. 2019; Parisio et al. 2019, 2020). The strength and mechanical properties of volcanic rocks are also of important in the context of geothermal energy exploitation (Siratovich et al. 2016; Eggertsson et al. 2020; Weaver et al. 2020; Heap et al. 2020c; Weydt et al. 2020). Finally, the failure mode of volcanic rocks also controls how their physical properties evolve. For example, brittle deformation can significantly reduce elastic wave velocities and create an elastic wave velocity anisotropy (e.g. Stanchits et al. 2006; Ougier-Simonin et al. 2011; Fortin et al. 2011; Adelinet et al. 2013; Harnett et al. 2018a), factors that should be considered when interpreting seismic tomography at active volcanoes. The brittle (e.g. Walker et al. 2013; Farquharson et al. 2016; Heap and Kennedy 2016) and ductile (e.g. Farquharson et al. 2017) deformation of volcanic rock can increase and decrease permeability, respectively, a metric considered important in dictating whether a particular eruption is explosive (high-

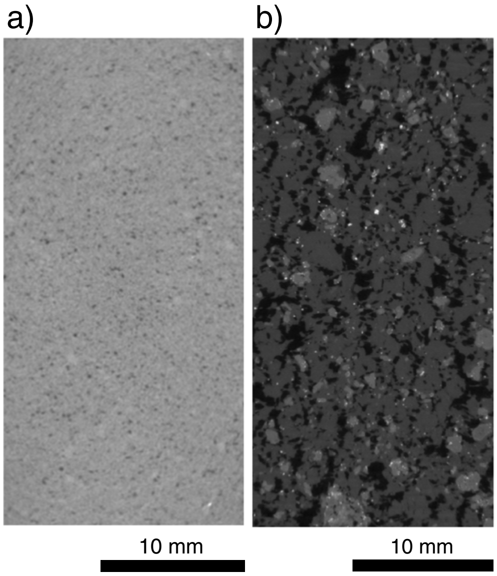

Fig. 1 (**a**) Two-dimensional slice extracted from a three-dimensional X-ray tomographic image (cubic voxels of width 48.8 µm) of Bentheim sandstone (Germany) (from Louis et al. 2007). (**b**) Two-dimensional slice extracted from a three-dimensional X-ray tomographic image (cubic voxels of width 23 µm) of an andesite from Volcán de Colima (Mexico) (from Heap et al. 2020a). The grey level of the voxels corresponds to their density (black = low density; white = high density)

risk) or effusive (lower risk) (e.g. Eichelberger et al. 1986; Mueller et al. 2008; Cassidy et al. 2018).

This review outlines recent advances in our understanding of the mechanical behaviour and failure modes of volcanic rocks. We first define the terms brittle and ductile. We then describe how the mechanical behaviour and failure modes of volcanic rocks are studied in the laboratory. We then present the results of uniaxial compressive strength (UCS) experiments on volcanic rocks, the factors that influence UCS, and micromechanical modelling designed to interpret these data. We then present the results of hydrostatic experiments on volcanic rocks and highlight the differences between brittle and ductile mechanical behaviour using triaxial deformation data (i.e. non-hydrostatic). Brittle failure envelopes and compactive yield caps for volcanic rocks are then compared, and we discuss the influence of porosity and other microstructural attributes on the stresses required for the brittle-ductile transition and shear-enhanced compaction. Microstructural observations showing the operative micromechanisms of deformation are provided for both brittle and ductile behaviour, and we discuss strain localisation in the ductile regime. Our review is focussed on the deformation of volcanic rocks in compression, although we also briefly summarise the tensile strength and frictional properties of volcanic rocks. Finally, we outline the implications of these data for volcanology and avenues for future research.

On the definition of brittle and ductile behaviour

In laboratory studies of rock deformation, the failure mode of a particular sample is often categorised as either brittle or ductile. A great number of rock deformation studies have focussed on finding the experimental conditions (often pressure and temperature) required for the switch from brittle to ductile behaviour (see reviews by Evans et al. 1990; Paterson and Wong 2005; Wong and Baud 2012). This review will describe brittle to ductile behaviour in volcanic rocks, and so it is important to first define how we use these terms. We consider that the relevant scale for assigning the failure mode (brittle or ductile) of a sample deformed in the laboratory is the lengthscale of the sample. In its simplest terms, the hallmark of brittle deformation is the localisation of strain (i.e. the formation of a macroscopic shear fracture), whereas ductility "describes the capacity of a material to deform to substantial strain without the tendency to localise the flow into bands (faults)" (Rutter 1986). This simple definition is somewhat complicated, however, by instances of compaction localisation in the ductile regime (Wong and Baud 2012). In this review, samples that contain compaction localisation features (compaction bands) are considered ductile. The operative micromechanisms of deformation are not considered when assigning failure mode, although brittle behaviour is synonymous with microcracking and frictional sliding. Ductile deformation can proceed via a multitude of cooperative micromechanisms, such as diffusional processes, crystal plasticity, twinning, and even microcracking in the case of cataclastic flow, and the efficiency of these processes depend on, amongst other factors, the experimental temperature and pressure and the imposed strain rate (Evans et al. 1990; Paterson and Wong 2005; Wong and Baud 2012). (We note that ductile deformation driven by microcracking is sometimes referred to as "semi-brittle".) Therefore, based on our definition, the concept of ductility in volcanic materials is not restricted to viscous flow.

Studying mechanical behaviour and failure mode in the laboratory

Rock deformation experiments are, for the most part, performed on cylindrical samples cored from larger blocks. Whereas granite, sandstone, and limestone blocks are typically sourced from quarries, the collection of volcanic materials to study in the laboratory is complicated for a number of reasons. First, collecting large and/or numerous blocks of volcanic rock is often impracticable: (1) blocks often have to be carried long distances (sometimes in challenging terrain), (2) potentially interesting sampling sites can be inaccessible due to concerns of safety, and (3) it can be prohibitively expensive to ship large blocks from volcanoes located in remote areas. Second, volcanoes often represent sites of local cultural significance and so permission and permits must be sought prior to any sample collecting expedition. Third, due to the heterogeneity of volcanic systems, a well-designed experimental study must first decide on the most representative/appropriate sample(s) to address the goal of the study. For example, if the goal is to understand the influence of porosity on the mechanical behaviour of lavas (the term "lava" is used in this review to refer to the cooled deposit of a lava flow), then blocks of lava characterised by different porosities should be collected (whilst trying to minimise other variables such as mineralogical composition, crystal size and content, and pore size and content). However, if the goal of the study is to analyse the stability of a lava dome or volcano flank, then one must first assess which materials are important to sample (e.g. the most volumetrically important rock type). We further note that most volcanic materials sourced for experimental studies are surface or outcrop samples and that samples from boreholes, that best represent the physical state of rock at depth, are rare due to the high cost associated with drilling and retrieving samples.

Once the blocks are in the laboratory, cylindrical samples (typically 10–40 mm in diameter) are cored, cut, and their end-faces are ground flat and parallel. Suggested methods for rock deformation, such as those outlined by the International Society for Rock Mechanics (ISRM), typically advise experimentalists to avoid using samples with a diameter less than 54 mm. However, and due to the aforementioned difficultly in collecting large blocks, preparing large-diameter volcanic rock samples is often not possible. As a result, experimental studies on volcanic rocks typical use cylindrical samples that are 10–40 mm in diameter. We forward here, as also recommended by the ISRM, that using small-diameter samples is acceptable as long as the sample diameter is at least ten times larger than the largest pore or crystal. Due the heterogeneous distribution of stress within a cylindrical sample deformed in uniaxial compression (e.g. Hawkes and Mellor 1970), it is also recommended by the ISRM that cylindrical samples should have a length to diameter ratio of 2.5 to 3. Mogi (2007) found that the uniaxial compressive strength of cylindrical samples (of granite, dolomite, and trachyte) increases at length to diameter ratios above 2.5 (see also Tuncay et al. 2019), and that the influence of this ratio on compressive strength decreased when the samples were deformed under a confining pressure. Due to the paucity of data of this type, especially for volcanic rocks, we provide new experiments, described in the Appendix, designed to explore the influence of the length to diameter ratio on the uniaxial compressive strength of a dry porous trachyandesite. Based on these new data, we recommended here that experimental studies use samples that have a length to diameter ratio of at least 2 and, importantly, that the dimensions of the samples used are reported in published works.

The most common, and most simple, type of experiment employed to study the mechanical behaviour of volcanic rocks is a uniaxial compression experiment (Fig. 2a). In this type of experiment, the cylindrical sample is placed between two steel pistons. The radial pressure on the sample is equal to atmospheric pressure (i.e. the minimum and intermediate principal stresses are both equal to 0.1 MPa) and one of the pistons moves at a constant displacement or loading rate until the sample fails macroscopically (the formation of a macroscopic fracture). Deformation at a constant strain rate of 10^{-5} s^{-1} is common in studies of rock deformation, including those on volcanic rocks. The main metric of interest is the uniaxial compressive strength (i.e. the maximum axial stress the sample sustained before macroscopic failure), but the mechanical data from these tests can also be used to provide values of, for example, static Young's modulus and Poisson's ratio. Axial force is monitored using a load cell and displacement (axial and radial) by linear variable differential transducer(s) (LVDT), strain gauge(s) glued onto the sample, optical/laser displacement transducer(s), and/or by a circumferential strain belt. A recent paper also found that near-infrared spectroscopy can be used as a non-contact technique for measuring strain (Butcher et al. 2019). Force and displacement (corrected for the displacement of the loading chain) are then converted to axial stress and axial strain using the sample dimensions. Uniaxial load frames can also set up to measure, for example, the output of acoustic emissions (AE) (a proxy for microcrack initiation and growth; Lockner 1993) and the evolution of elastic wave velocities (and therefore the evolution of dynamic elastic moduli) during deformation. If equipped with a high-temperature furnace, uniaxial compression experiments can also be performed at high in-situ temperatures.

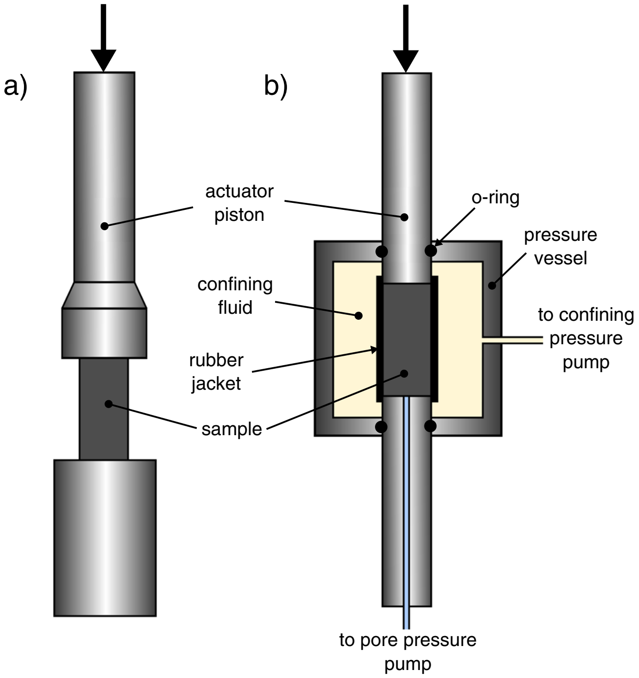

Fig. 2 (**a**) Schematic diagram showing a typical setup for a uniaxial compressive strength experiment. (**b**) Schematic diagram showing a typical setup for a triaxial deformation experiment. Arrows indicate how the upper piston moves to deform the sample in compression. Experimental samples are typically 10–40 mm in diameter. Setup dimensions will vary from machine to machine

Triaxial compression experiments are required for a complete mechanical characterisation of a given material. The cylindrical sample is placed between two steel pistons, as for a uniaxial experiment (Fig. 2b). However, for a triaxial experiment, the sample is sleeved in an impermeable jacket (often nitrile or Viton® for low-temperature experiments and copper or steel for high-temperature experiments) and placed inside a pressure vessel (Fig. 2b). A confining fluid (typically oil or gas) is pumped into the pressure vessel to apply a radial or confining pressure (the minimum and intermediate principal stresses are both equal and are both higher than atmospheric pressure), which is typically controlled by a pressure pump or intensifier. Triaxial experiments can be performed on oven-dry samples without a pressurised pore fluid within their void space, but are often performed on samples saturated with distilled/deionised water or gas that is pressurised and controlled by another pressure pump or intensifier (Fig. 2b). Before performing an experiment on a liquid-saturated (e.g.

distilled/deionised water) sample, it is good practice to leave the saturated sample in a container of the liquid for 48 h prior to loading it into the machine, to allow time for the sample to equilibrate with the liquid. It is common to increase the confining pressure and pore pressure (such that the pore pressure never exceeds the confining pressure) to pre-defined values and keep them constant during the experiment (i.e. during the deformation of the sample) using the aforementioned confining and pore pressure pumps. Before deforming the sample, it is good practice to leave the sample at the target pressures for at least an hour to allow the rock microstructure to equilibrate to the imposed pressure conditions. The sample is then deformed by moving one of the steel pistons at a given displacement or loading rate (often a displacement rate that corresponds to a strain rate of 10^{-5} s^{-1}). Although the typically used laboratory strain rate of 10^{-5} s^{-1} is faster than most geological strain rates (Fagereng and Biggs 2019), we note that the strain rates in volcanic systems are likely very variable. The displacement of the piston and the axial load on the sample are typically measured using the methods described for the uniaxial experiments, and then converted to axial strain (corrected for the displacement of the loading chain) and axial stress using the sample dimensions. If necessary, such as when metal jackets are used, the measurement of force is corrected for the contribution of the jacket at the imposed experimental temperature. By monitoring the movement of the pore pressure intensifier, the change in sample volume or porosity can also be monitored during deformation. Changes in volumetric strain (i.e. sample porosity) during deformation can also be determined using strain gauges glued onto the sample. For experiments performed using a pore fluid pressure, it is important to ensure that the sample is "drained". In other words, that the deformation of the sample does not exceed the time required for the fluid to reach the tips of growing microcracks. If the permeability of the sample is not too low ($>10^{-16}$ m^2), then there should be no drainage issues at the strain rates typically used in the laboratory (10^{-5} s^{-1}); however, this may be an issue for low-permeability volcanic samples and a lower strain rate should perhaps be considered (e.g. 10^{-6} s^{-1}) (Heap and Wadsworth 2016). We highlight that drainage is a separate issue to that of pre-deformation saturation: completely saturated samples will be undrained if they are deformed quicker than fluids can reach growing microcrack tips. Depending on the capability of the system, and the goal of the experiment, deformation can be halted at an axial strain much greater than that required for the formation of a macroscopic shear fracture in a brittle experiment. For experiments at conditions at which the sample is expected to be in the ductile regime, it is prudent to deform the sample to a high axial strain to ensure ductile behaviour. As for the above-described uniaxial experiments, if the kit is available, the output of AE and the evolution of elastic wave velocities can be measured during deformation. Some triaxial deformation devices, such as the "Paterson press" (e.g. Paterson and Olgaard 2000; Violay et al. 2015a), are equipped with a furnace and can deform samples at high in-situ temperatures.

Other types of commonly performed test using a triaxial deformation apparatus include: (1) hydrostatic experiments (i.e. $\sigma_1 = \sigma_2 = \sigma_3$), during which the confining pressure is increased slowly increased whilst monitoring for changes in the porosity and/or elastic wave velocities of the sample and (2) creep experiments, during which the sample is left to deform at a constant differential stress close to its short-term failure stress (e.g. Heap et al. 2011).

It is common in studies of rock deformation to assume a simple effective pressure law, where the effective pressure, P_{eff}, is equal to the confining pressure, P_c, minus the pore fluid pressure, P_p. In this review, as is the case for the vast majority of rock deformation studies, we consider that compressive stresses and strains are positive.

Mechanical behaviour and failure modes of volcanic rock

The uniaxial compressive strength of volcanic rocks

A typical uniaxial stress-strain curve for volcanic rock

Before discussing the influence of the various rock attributes (such as porosity) on the uniaxial compressive strength of volcanic rocks, we will first describe a typical stress-strain curve for volcanic rock deforming in uniaxial compression. A typical uniaxial stress-strain curve for volcanic rock, an andesite from Volcán de Colima, is presented in Fig. 3 (data from Heap et al. 2014a).

First, axial stress is a non-linearly increasing function of axial strain. This stage is often attributed to the closure of pre-existing microcracks that are oriented such that their major-axis is perpendicular or sub-perpendicular to the sample axis. This stage is followed by a quasi-linear stage. The deformation in this stage is often considered to be elastic and static elastic moduli, such as the Young's modulus, can be determined using data from this stage (as indicated in Fig. 3). In the next stage, axial stress is a non-linearly decreasing function of axial strain. The start of this stage marks the stress at which the deformation is no longer elastic and microcracks form, grow, and coalesce. The stress required for the onset of microcracking, also characterised by an uptick in AE activity, is termed *C*' (indicated in Fig. 3). A peak stress (the uniaxial compressive strength of the rock, σ_p; see Fig. 3), preceded by an exponential increase in AE activity and followed by a stress drop, is the last stage and signals the end of the experiment. During this stage, coalesced microcracks conspire to form a macroscopic (i.e. sample-scale) fracture within the sample. Post-mortem microstructural observations on volcanic

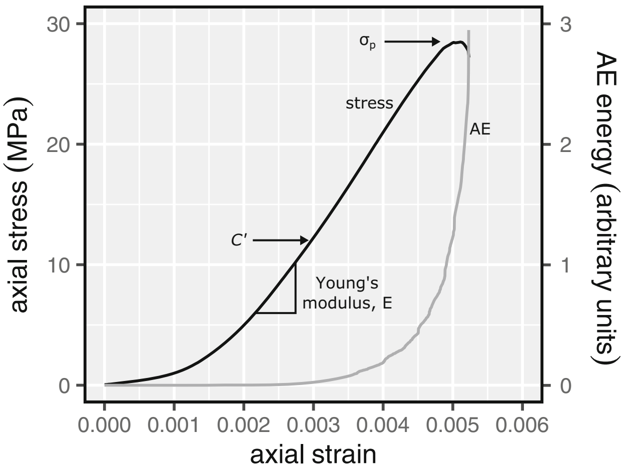

Fig. 3 A typical stress-strain curve, and accompanying acoustic emission (AE) energy, for a volcanic rock deformed under uniaxial compression. This curve is for an andesite from Volcán de Colima with a connected porosity of 0.25 (data from Heap et al. 2014a). The onset of dilational microcracking, *C'*, and the uniaxial compressive strength, σ_p, are labelled on the curve. The region typically used for the calculation of Young's modulus, *E*, is also indicated

samples deformed in uniaxial compression show microcracks emanating from pores and traversing through both groundmass and phenocrysts (Fig. 4). The stress-strain curve for andesite under uniaxial compression shown in Fig. 3 (from Heap et al. 2014a) is qualitatively similar to those for other volcanic rocks, such as basalt (e.g. Schaefer et al. 2013) and dacite (e.g. Coats et al. 2018), and other non-volcanic rocks, such as granite (e.g. Brace et al. 1966; Scholz 1968) and sandstone (e.g. Baud et al. 2014).

Factors that influence the uniaxial compressive strength of volcanic rocks

Due to its first-order importance, uniaxial compressive strength datasets are often plotted as a function of sample porosity. Experimental studies have shown that the uniaxial compressive strength of volcanic rocks decreases as a function of increasing porosity (e.g. Al-Harthi et al. 1999; Pola et al. 2014; Heap et al. 2014b; Schaefer et al. 2015; Mordensky et al. 2018; Coats et al. 2018), as observed for porous sedimentary rocks (e.g. Baud et al. 2014). Figure 5 shows uniaxial compressive strength as a function of porosity for a compilation of volcanic rocks. This compilation includes data for andesite, basalt, dacite, and pyroclastic rocks (e.g. tuffs and welded block-and-ash flow (BAF) deposits). The compilation shown in Fig. 5 does not include samples deformed "wet" (vacuum-saturated with distilled/deionised water), samples that were deformed at strain/loading rates very different from 10^{-5} s^{-1}, samples deformed at high in-situ temperatures, and samples thermally stressed prior to deformation. The influence of these factors is discussed separately below. All of these compiled data are provided in a Microsoft Excel© spreadsheet that accompanies this contribution as Supplementary Material.

The data of Fig. 5 show that, although the uniaxial compressive strength of volcanic rocks decreases nonlinearly as a function of increasing porosity, there is considerable scatter in the data. For example, at a porosity of 0.02, the strength can be as low as ~25 MPa and as high as ~330 MPa (Fig. 5). We also note that the range in strength for a given porosity is reduced as porosity increases; for example, at a porosity of 0.6, strength varies from a couple of MPa to ~50 MPa (Fig. 5).

In order to better understand the data, and the variability in the data, presented in Fig. 5, we plot uniaxial compressive strength as a function of porosity for the four main rock types in our compilation: andesite, basalt, dacite, and pyroclastic rocks (Fig. 6). These plots show that, for all rock types, uniaxial compressive strength is reduced nonlinearly as a function of increasing porosity (Fig. 6). As for the combined dataset (Fig. 5), we observe that the range in strength is high at low-porosity and low at high-porosity for the two most represented rock types, andesite (Fig. 6a) and basalt (Fig. 6b). The trend for dacite, the dataset with the fewest data, is obscured by the paucity of data at low (< 0.1) and high (> 0.3) porosity (Fig. 6c). The data for pyroclastic rocks show two main trends, one defined by the variably welded block-and-ash flow deposits from Mt. Meager (Canada) (Heap et al. 2015a) and one defined by the variably altered Ohakuri ignimbrites (New Zealand) (Heap et al. 2020c) (Fig. 6d).

It is clear from Fig. 6 that the scatter in the compiled dataset (Fig. 5) cannot be explained by differences in rock type. The reasons for this are twofold. Although porosity exerts a first-order control on the uniaxial compressive strength of volcanic rocks (Figs. 5 and 6), (1) it does not consider differences in factors such as hydrothermal alteration, crystal content, and groundmass crystallinity and (2) porosity is a scalar and does not consider the nature of the void space: the proportion of pores and microcracks and their geometrical properties (e.g. pore radius and shape). The influence of these parameters on the uniaxial compressive strength of volcanic rocks is discussed below.

Experiments have shown that hydrothermal alteration can either decrease or increase the strength of volcanic rocks (e.g. del Potro and Hürlimann 2009; Wyering et al. 2014; Frolova et al. 2014; Pola et al. 2014; Mordensky et al. 2018; Farquharson et al. 2019; Heap et al. 2020c; Frolova et al. 2020). Alteration associated with porosity reduction (e.g. dissolution) and/or the formation of clays can reduce strength (e.g. del Potro and Hürlimann 2009; Farquharson et al. 2019; Frolova et al. 2020) and alteration associated with a decrease in porosity (e.g. pore- and crack-filling alteration) can increase strength (e.g. Heap et al. 2020a). For example, at a given porosity, the argillic alteration that characterises Pinnacle Ridge at Mt Ruapehu (New Zealand) appears to decrease the strength of andesite (Fig. 7a; Mordensky et al.

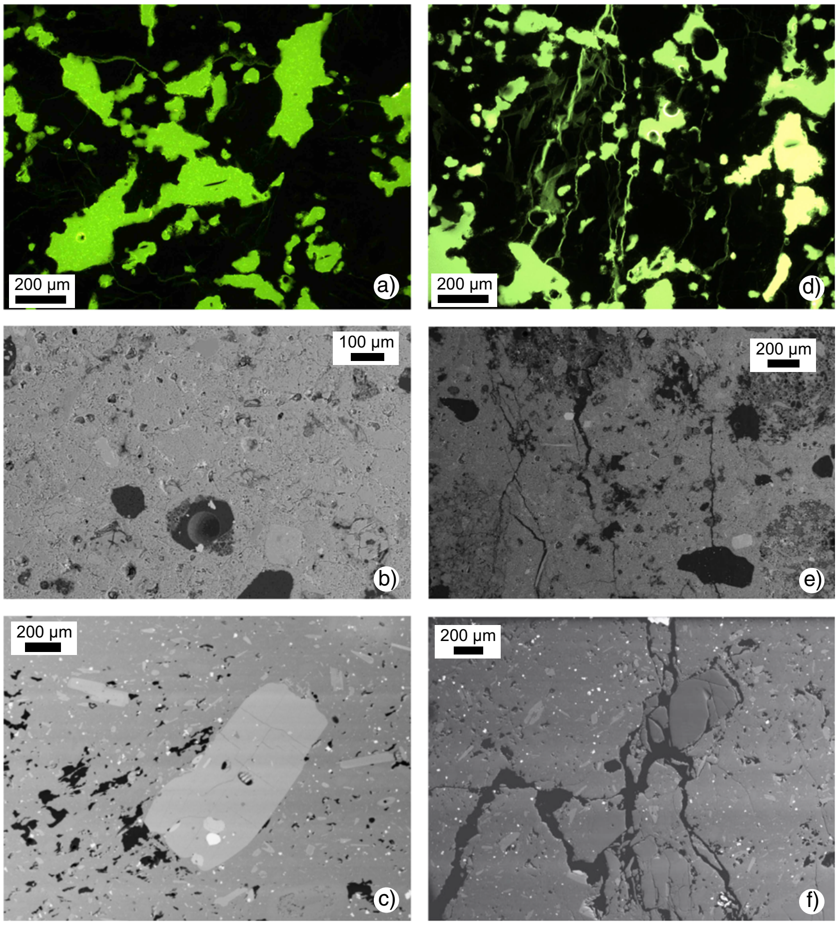

Fig. 4 (**a**) Optical microscope image of intact andesite from Volcán de Colima (Mexico). The thin section was prepared with florescent epoxy and the image was taken using a transmitted florescent light source (the rock is shown in black and the pore space in florescent yellow/green). (**b**) Backscattered scanning electron microscope (SEM) image of intact tuff from Alban Hills (Italy) (from Zhu et al. 2011). (**c**) SEM image of intact dacite from Mt Unzen volcano (Japan) (from Coats et al. 2018). (**d**) Optical microscope image of andesite from Volcán de Colima deformed to failure under uniaxial compression (from Heap et al. 2014a). The thin section was prepared with florescent epoxy and the image was taken using a transmitted florescent light source. (**e**) SEM image of tuff from Alban Hills deformed to failure under uniaxial compression (from Zhu et al. 2011). (**f**) SEM image of dacite from Mt Unzen volcano deformed to failure under uniaxial compression (from Coats et al. 2018)

2018). Indeed, altered low-porosity andesite can be significantly weaker than unaltered andesite with the same porosity (Fig. 7a; Mordensky et al. 2018). Figure 7b shows data for highly-altered samples (that were initially identical) from the Ohakuri ignimbrite (Heap et al. 2020c). The uniaxial compressive strength of samples characterised by adularia/quartz alteration, which precipitated within the pores and reduced the porosity of the original deposit, ranged from ~20 to ~90 MPa, whereas the strength of samples characterised by smectite alteration was ~4–11 MPa (Fig. 7b; Heap et al. 2020c). These data not only highlight that alteration can significantly influence the strength of volcanic rock, but also that the type of alteration is important in dictating whether strength increases or decreases.

Crystals (phenocrysts and microlites) are also considered to influence the uniaxial compressive strength of volcanic rocks: phenocrysts are commonly microcracked and both phenocrysts and microlites introduce heterogeneities that could act as foci for stress concentration. However, recent deformation experiments have suggested that, due to the link between porosity and groundmass crystallinity, it is difficult to properly assess the role of crystallinity on rock strength (Zorn et al. 2018). Numerical modelling, in which all microstructural parameters except phenocryst content can be kept constant, has suggested that the strength of samples with the same porosity decreases as a function of increasing phenocryst content (Heap et al. 2016a).

Microcracks may not contribute much to the porosity of a material, because they are volumetrically small compared to pores, but they can greatly reduce rock strength. The partitioning of the porosity is therefore an important factor not considered in plots of uniaxial compressive strength as a function of porosity (e.g. Figs. 5 and 6). For example, the strength of a volcanic rock with a porosity of 0.02 composed entirely of pores would likely be higher than a rock of the same porosity composed entirely of microcracks. However,

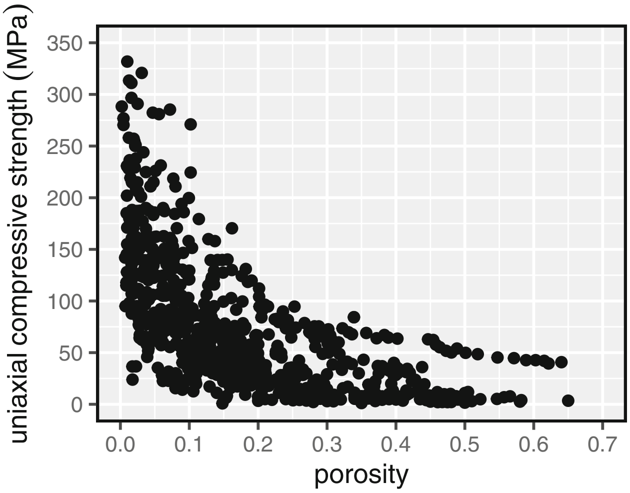

Fig. 5 Uniaxial compressive strength (UCS) as a function of porosity for volcanic rocks (n = 870; these data are provided in a Microsoft Excel© spreadsheet that accompanies this contribution as Supplementary Material). Data from: this study, Behre (1929), Price and Jones (1982), Price (1983), Erdoğan (1986), Erguvanlı et al. (1989), Ayday and Göktan (1990), Martin et al. (1994), Okubo and Chu (1994), Schultz and Li (1995), Topal and Doyuran (1997), Al-Harthi et al. (1999), Topal and Sözmen (2003), Török et al. (2004), Apuani et al. (2005), Yassaghi et al. (2005), Jackson et al. (2005), Tuncay (2009), Erguler and Ulusay (2009), Zhu et al. (2011, 2016), Heap et al. (2012), Yavuz (2012), Karakuş and Akatay (2013), Kendrick et al. (2013a), Heap et al. (2014a), Pola et al. (2014), Siratovich et al. (2014), Heidari et al. (2014), Wyering et al. (2014), Çelik et al. (2014), Karaman and Kesimal (2015), Celik and Ergül (2015), Schaefer et al. (2015), Heap et al. (2015a, 2015c), Montanaro et al. (2016), Zhu et al. (2016), Marmoni et al. (2017), Bubeck et al. (2017), Heap et al. (2018a, 2018b), Coats et al. (2018), Mordensky et al. (2018), Lavallée et al. (2019), Harnett et al. (2019), Heap et al. (2020b), Ryan et al. (2020), Kennedy et al. (2020), Di Muro et al. (2021), and Kendrick et al. (2021)

while systematic studies on the influence of microcracks on the strength of granite exist, conducted by thermally stressing samples to different temperatures to create a suite of samples with different microcrack densities (e.g. Alm et al. 1985; David et al. 2012; Griffiths et al. 2017a), corresponding studies on volcanic rocks have been so far less insightful due to the difficulty in preparing samples characterised by different degrees of microcracking (e.g. Heap et al. 2014a; Schaefer et al. 2015; Coats et al. 2018; Heap et al. 2018a). These experimental studies have shown that some volcanic rocks may not form additional microcracks when thermally stressed in the laboratory. Indeed, the influence of thermal stressing on volcanic rocks may be linked to their original microstructure, as discussed in Daoud et al. (2020). Therefore, although we expect an increase in microcrack density to decrease the uniaxial compressive strength of volcanic rock, it is challenging at present to conclude as such with the available experimental data.

The size and shape of pores is also known to influence the strength of volcanic rock. First, numerical modelling suggests that the strength of volcanic rock, when all other microstructural parameters are equal, decreases as a function of increasing pore radius (Heap et al. 2014b; see also Fakhimi and Gharahbagh 2011). The modelling of Heap et al. (2014b) also suggests that the strength of a sample containing a non-uniform pore radius will be closest in strength to that of the largest pore size end-member. However, corresponding systematic experiments aimed at exploring the influence of pore radius and pore size distribution on the strength of volcanic rocks are absent owing to the difficulty in collecting samples for which all other factors, especially the porosity, are equal. Second, the influence of pore geometry on the strength of volcanic rocks was illuminated by Bubeck et al. (2017), who showed that the strength anisotropy of basalt from Kīlauea (USA) was negligible when the pores were sub-spherical, whereas basalt containing low aspect ratio (the ratio of the minor to the major axis) pores had a uniaxial compressive strength of ~80 and ~40 MPa when deformed parallel and perpendicular to the pore major axis, respectively (see also Griffiths et al. 2017b). Pore size and shape are microstructural parameters not considered in plots of uniaxial compressive strength as a function of porosity (e.g. Figs. 5 and 6).

To conclude, the scatter in the data of Fig. 5 cannot be simply explained by differences in rock type (because a similar scatter is observed for a constant rock type; Fig. 6) and is therefore, primarily, the result of the high variability of volcanic rock samples in terms of hydrothermal alteration, crystallinity, microcrack density, pore radius, and pore shape, amongst other factors. It is unfortunately not possible to plot the uniaxial compressive strength data of Fig. 5 as a function of these parameters, or a variable that combines several of these parameters, primarily because these parameters are rarely quantified in published studies. To assist future data compilations, we urge future laboratory studies to provide as much information as possible on their experimental materials.

Environmental factors such as the presence of water, strain rate, and temperature can also influence the strength of volcanic rocks. The data shown in Figs. 5 and 6 do not include samples deformed wet (i.e. saturated with water), at strain/loading rates very different from 10^{-5} s^{-1}, following thermal stressing, and at high in-situ temperatures. We will now discuss the influence of these factors on the uniaxial compressive strength of volcanic rocks.

Water-weakening, where the dry strength of a rock is higher than its wet strength, has been observed in sedimentary rocks, such as sandstone, and is thought to be the result of the presence of clays and a reduction in specific surface energy, fracture toughness, and internal friction coefficient (e.g. Baud et al. 2000a; Vásárhelyi and Ván 2006; Heap et al. 2019a). For tuffs, Zhu et al. (2011) suggested that water-weakening was largely due to a reduction in fracture toughness, but may be influenced by other microstructural and mineralogical factors. More recently, Heap et al. (2018b) suggested that the presence of clays and zeolites could explain water-weakening in tuffs.

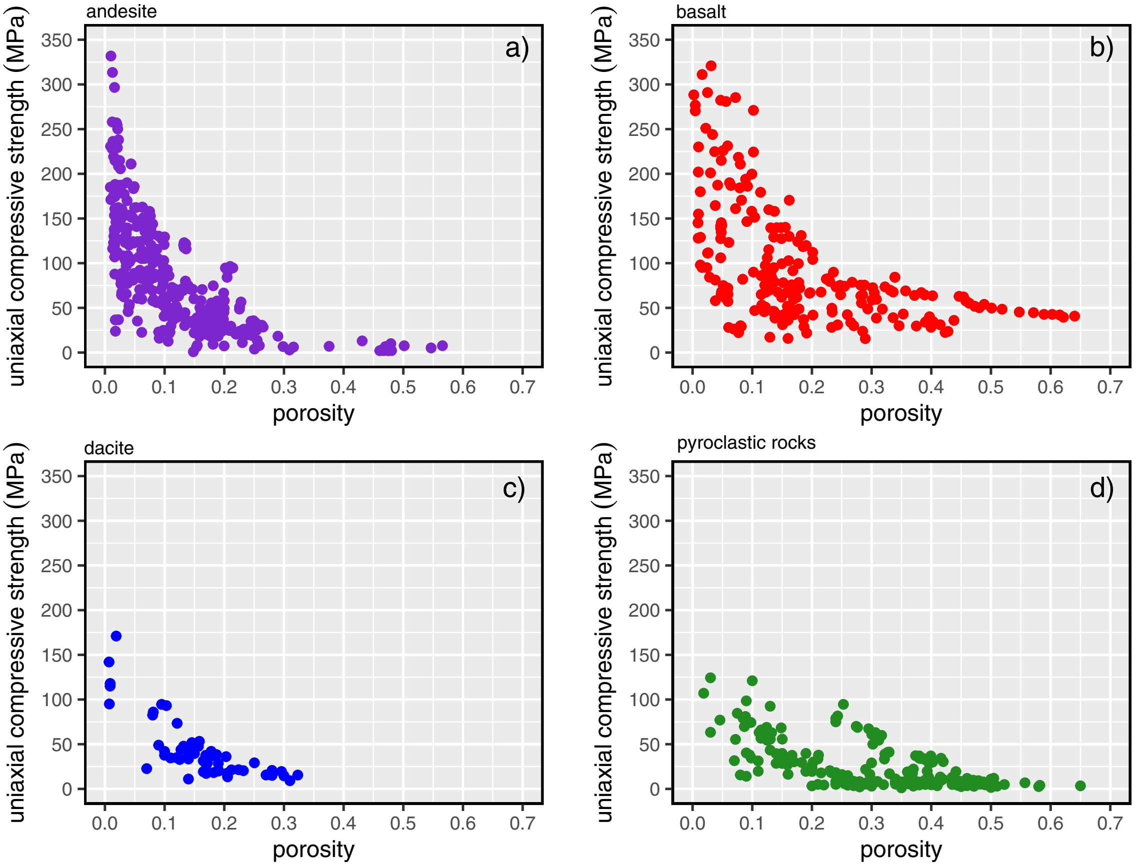

Fig. 6 Uniaxial compressive strength (UCS) as a function of porosity for (**a**) andesite, (**b**) basalt, (**c**) dacite, and (**d**) pyroclastic rocks (these data are provided in a Microsoft Excel© spreadsheet that accompanies this contribution as Supplementary Material). References for the data used in this figure are provided in the caption of Fig. 5

These authors found that large changes between the dry and wet strength of tuff were observed for tuffs containing clays and zeolites, and that this difference was negligible when no clays or zeolites were present. We present in Fig. 8a the ratio of wet to dry strength as a function of porosity for published data for tuffs (compiled in Heap et al. 2018b). Because such data are extremely rare or absent for volcanic rocks other than tuffs, Fig. 8a also shows data unique to this study for two basalts from Mt Etna (Italy), a trachyandesite from Volvic (Chaîne des Puys, France), an andesite from Kumamoto (Japan), two andesites from Volcán de Colima, and a block-and-ash flow from Mt. Meager (data provided in Table 1). These new experiments were performed at a strain rate of 1.0×10^{-5} s^{-1}. Dry samples were vacuum-dried at 40 °C for at least 48 h prior to experimentation, and wet samples were first vacuum-saturated in deionised water and then deformed within a water-filled container. Also included in Fig. 8a are recent data for dacite from Mt Unzen volcano (Japan; Kendrick et al. 2021). The ratio of wet to dry uniaxial compressive strength is 1.09 and 0.96 for the two basalts (basalt 1 and basalt 2, respectively), 0.92 for the trachyandesite, 0.87 for the block-and-ash flow, and 0.56, 0.93, and 1.07 for the three andesites (Kumamoto, andesite 1, and andesite 2, respectively) (Table 1). The ratios calculated for the dacites from Kendrick et al. (2021) are 1.04, 0.81, 0.97, 0.60, and 0.82 (for UNZ1, UNZ9a, UNZ9b, UNZ13, and UN14, respectively; see Kendrick et al. 2021).

The data of Fig. 8a show that there is no systematic variation in water-weakening as a function of porosity. These data also show that, excluding the andesite from Kumamoto and the high-porosity dacite sample, water-weakening appears to be more pronounced in tuffs than in the lavas and block-and-ash flow deposit. As described above, variable clay and zeolite contents for the compiled data for tuffs could explain, in part, the scatter in strength reduction as a function of porosity (Fig. 8a; Heap et al. 2018b). In the absence of the data for three lavas with a ratio above 1 (the low-porosity basalt from Etna, the high-porosity andesite from Volcán de Colima, and one of the dacites from Mt Unzen volcano), one could conclude that lavas also are weaker when wet (Fig. 8a). However, if sample-to-sample variability can explain the > 1 ratio in these three rocks, it can also explain the water-weakening observed in all samples except the andesite from Kumamoto and the high-porosity dacite sample from Mt Unzen volcano. Although we cannot forward a definitive reason for the large observed water-weakening in the andesite from Kumamoto, it may be a

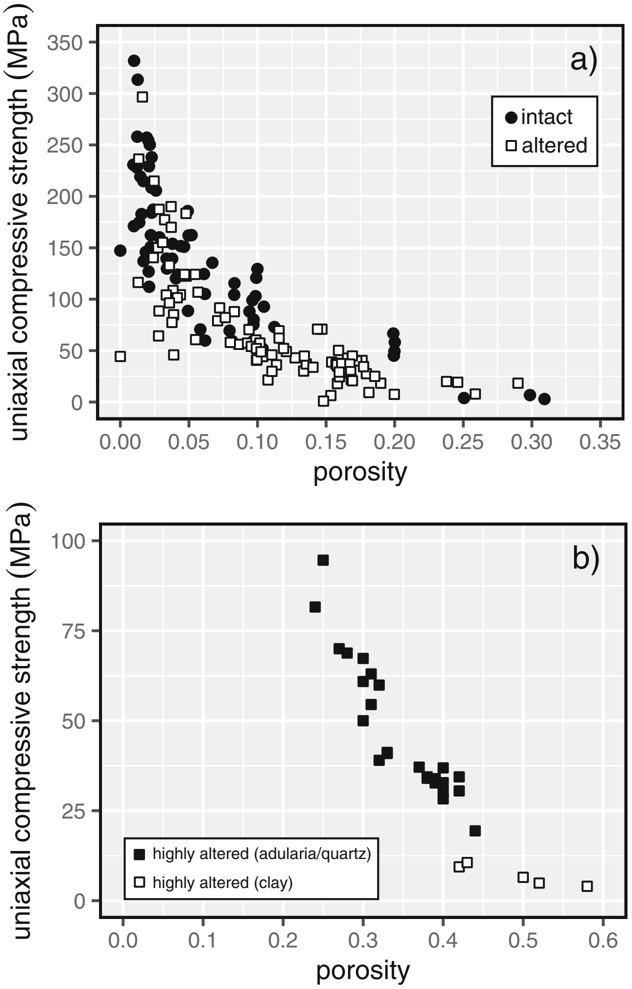

Fig. 7 (**a**) Uniaxial compressive strength (UCS) as a function of porosity for unaltered (black circles) and altered (white squares) andesites (light to advanced argillic alteration) from Mt Ruapehu (New Zealand). Data from Mordensky et al. (2018). (**b**) UCS as a function of porosity for highly altered Ohakuri ignimbrite samples (New Zealand) that display adularia/quartz alteration (black squares) and smectite alteration (white squares). Both of these highly altered samples contain no glass (the original deposit was found to contain 86 wt.% glass). Data from Heap et al. (2020c)

consequence of the large amount of feldspar in this rock (~50%; Nara et al. 2010a), a mineral thought to be responsible for some of the observed water-weakening in sandstone (Baud et al. 2000a). Only one wet experiment was performed on each of the dacites from Mt Unzen volcano. Because sample-to-sample variability was high for these dacites (Kendrick et al. 2021), these data may invite overinterpretation. More experiments are now required to better understand water-weakening in lavas.

The data shown in Fig. 8a suggest that rock completely saturated with water can be weaker than dry rock. However, recent data provided in Hashiba et al. (2019) showed that an andesite with a porosity of 0.17 progressively weakened as the saturation index (the proportion of the porosity saturated with water) increased from almost 0 to 1 (Fig. 8b). In detail, reductions in strength were high up to a saturation index of 0.2 (from ~95 to ~68 MPa), and only decreased by a further couple of MPa as the saturation index was increased to 1 (Hashiba et al. 2019; Fig. 8b). The systematic reduction in strength as a function of increasing saturation index adds confidence to the hypothesis that lavas can be weaker when wet. The data in Fig. 8b also suggest that water-weakening in volcanic rocks may only require partial saturation. More data are now necessary to test this hypothesis.

A reduction in strain rate is known to reduce the uniaxial compressive strength of granites and sandstones (e.g. Paterson and Wong 2005). Laboratory studies have also shown that the strength of dacite (Coats et al. 2018), basalt (e.g. Schaefer et al. 2015), and andesite (Lavallée et al. 2019) decrease as a function of increasing strain rate (in the range 10^{-6} to 10^{-1} s^{-1}). The data from Lavallée et al. (2019), for dry (i.e. room humidity) porous andesite from Volcán de Colima, show a systematic decrease in uniaxial compressive strength, from 60.5 MPa at a strain rate of 10^{-1} s^{-1} to 36.6 MPa at a strain rate of 10^{-6} s^{-1} (Fig. 9). Figure 9 also shows uniaxial compressive strength as a function of strain rate for wet samples of Kumamoto andesite, data unique to this study (Table 2). These samples were first vacuum-saturated in deionised water and then deformed within a water-filled container at strain rates from 10^{-8} to 10^{-4} s^{-1}. Uniaxial compressive strength was reduced from 76.3 MPa at a strain rate of 10^{-4} s^{-1} to 55.1 MPa at a strain rate of 10^{-8} s^{-1} (Fig. 9). The reduction in strength as strain rate decreases considered to be a result of the increased time available for time-dependent processes, such as stress corrosion cracking (Heap et al. 2011), a mechanism that can influence deformation even under ambient laboratory humidity (e.g. Brantut et al. 2013).

The influence of thermal stressing (i.e. transient exposure to high temperature) on the uniaxial compressive strength of volcanic rocks has been reasonably well studied. In tuffs, thermal stressing has been shown to reduce uniaxial compressive strength if they contain minerals that are affected by high-temperatures, such as zeolites (e.g. Heap et al. 2012, 2018c; Fig. 10a). For example, the strength of the Neapolitan Yellow Tuff (Italy) was reduced from ~3.5 MPa to < 1 MPa following exposure to 700 °C (Heap et al. 2012). The strength of green tuff from Mt Epomeo (Ischia Island, Italy) was reduced from ~4.5 to ~1.5 MPa following exposure to 1000 °C (Heap et al. 2018c). However, the strength of tuff that did not contain zeolites was not affected by exposure to a temperature of 1000 °C (Heap et al. 2012; Fig. 10b). These studies concluded that the observed weakening following exposure to high temperature was a result of microcracking and a porosity increase as a result of the dehydroxylation of zeolites and clays. A recent study also showed that smectite dehydration at high temperature (up to 600 °C) reduced the strength of hyaloclastite from the Krafla geothermal reservoir (Iceland; Weaver et al. 2020).

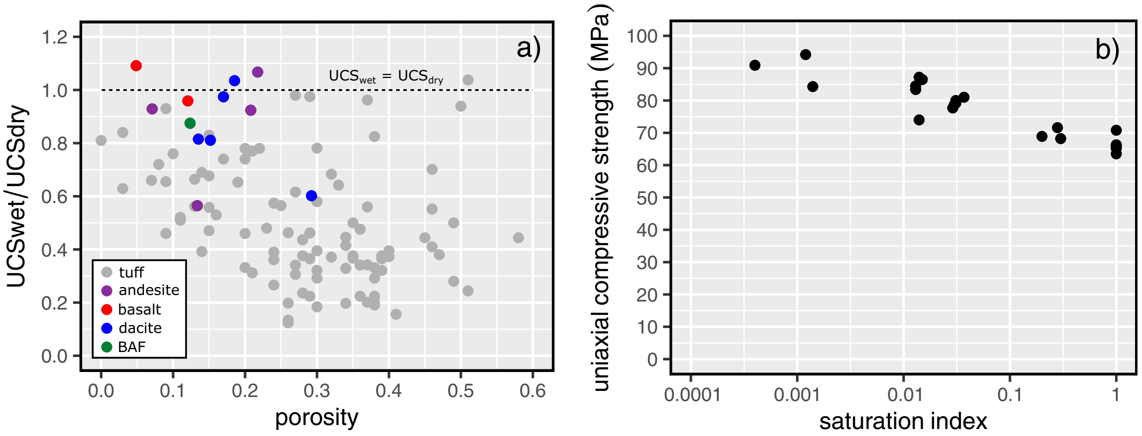

Fig. 8 (**a**) The ratio of wet to dry uniaxial compressive strength (UCS) as a function of porosity. Data for tuff are those compiled in Heap et al. (2018b). References for the tuff data used in this figure are provided in the caption of Fig. 5. Data for lava (basalt, andesite, and trachyandesite) and block-and-ash flow (BAF) are calculated using the averages of the values presented in Table 1 (data unique to this study). Data for dacite from Kendrick et al. (2021). (**b**) UCS as a function of saturation index (proportion of the porosity saturated with water) for Sanjome andesite (porosity = 0.17). Data from Hashiba et al. (2019)

Duclos and Paquet (1991) found that the strength of basalt from the French Massif Central was reduced following exposure to high temperature (Fig. 10d). These authors found that uniaxial compressive strength decreased from ~340 MPa (no thermal stressing) to ~140 MPa following exposure to 1000 °C (Duclos and Paquet 1991; Fig. 10d). However, the majority studies have found that the uniaxial compressive strength of lavas (basalt, andesite, and dacite) is largely independent of thermal stressing temperature, even for samples exposed to 900 °C (e.g. Heap et al. 2009; Kendrick et al. 2013a; Heap et al. 2014a; Schaefer et al. 2015; Coats et al. 2018; Heap et al. 2018a). Uniaxial compressive strength as a function of thermal stressing temperature for andesite from Volcán de Colima (with a porosity of 0.07 to 0.09) is shown in Fig. 10c (the studies of Heap et al. (2014a), Schaefer et al. (2015), and Coats et al. (2018) only measured strength for one thermal stressing temperature). These data show that uniaxial compressive strength was unaffected by thermal stressing temperature. Reasons forwarded to explain this independence include (1) the mineral constituents of these volcanic rocks do not undergo chemical or phase transformations within the studied temperature range, (2) that these volcanic rocks adhere to the Kaiser temperature memory effect, which stipulates that a rock must be exposed to a temperature higher than it has previously seen to impart new microcrack damage, and (3) that thermal expansion is accommodated by the numerous pre-existing microcracks within these materials and, as a result, stresses at the microscale do not exceed the local strength of the mineral constituents.

High in-situ temperatures are also known to influence the uniaxial compressive strength of volcanic rocks. Since the focus of this review is volcanic rocks, not magma, we will restrict our discussion here to samples that failed in a brittle manner and exclude those that deformed viscously. When glassy samples are deformed at high temperature at a strain rate slower than the relaxation timescale of their melt phase, they will deform in a ductile manner (e.g. Lavallée et al. 2013; Kendrick et al. 2013b; Coats et al. 2018). Some laboratory studies have shown that the uniaxial compressive strength of volcanic rocks increases as a function of increasing temperature (e.g. Duclos and Paquet 1991; Benson et al. 2012; Schaefer et al. 2015; Coats et al. 2018; Heap et al. 2018a). For example, the strength of andesite from Volcán de Colima was increased from ~120 MPa at an in-situ temperature of 400 °C to ~133 MPa at an in-situ temperature of 700 °C (Heap et al. 2018a; Fig. 10c) (the studies of Schaefer et al. (2015), and Coats et al. (2018) only measured strength for one high in-situ temperature). The strength of basalt from the French Massif Central increased up to 700 °C and then decreased at temperatures of 800, 900, and 1000 °C (Duclos and Paquet 1991; Fig. 10d). To explain the strengthening at high-temperature, some of these studies hypothesised that pre-existing microcracks, abundant in these materials, closed at high temperature due to mineral expansion, thus strengthening the material. Several experimental studies, however, have shown that the uniaxial compressive strength of volcanic rocks does not change as a function of temperature or decreases at high-temperature. For example, Smith et al. (2011) found that the uniaxial compressive strength of a glass-poor dacite from Mt St Helens (USA) was unchanged as temperature was increased from 25 to 900 °C. Smith et al. (2009), however, showed that the uniaxial compressive strength of andesite from Mt Shasta (USA) was unchanged up to a temperature of 600 °C (~125 MPa) and was reduced to ~90 MPa at a temperature of 900 °C. Similarly, Rocchi et al. (2004) found that the strength of basalts from Mt Etna and Vesuvius (Italy) was unchanged up to 600 °C, decreased at 800 °C, and decreased further at 1000 °C. These same authors showed that the strength of a lava crust

Table 1 Summary of the data unique to this study used to assess the influence of water on the uniaxial compressive strength (UCS) of volcanic rocks. Experiments were performed at a strain rate of 1.0×10^{-5} s^{-1}. Dry samples were vacuum-dried at 40 °C for at least 48 h prior to experimentation, and wet samples were first vacuum-saturated in deionised water and then deformed within a water-filled container. *BAF* block-and-ash flow

Volcano	Rock type	Porosity	Condition	UCS (MPa)
Mt Etna (Italy)	Basalt 1	0.05	Dry	141.7
Mt Etna (Italy)	Basalt 1	0.05	Dry	145.3
Mt Etna (Italy)	Basalt 1	0.05	Dry	134.5
Mt Etna (Italy)	Basalt 1	0.05	Dry	127.5
Mt Etna (Italy)	Basalt 1	0.05	Dry	142.4
Mt Etna (Italy)	Basalt 1	0.05	Wet	155.2
Mt Etna (Italy)	Basalt 1	0.05	Wet	145.4
Mt Etna (Italy)	Basalt 1	0.05	Wet	158.6
Mt Etna (Italy)	Basalt 1	0.05	Wet	144.5
Mt Etna (Italy)	Basalt 2	0.10	Dry	19.7
Mt Etna (Italy)	Basalt 2	0.14	Dry	16.2
Mt Etna (Italy)	Basalt 2	0.14	Dry	17.0
Mt Etna (Italy)	Basalt 2	0.15	Dry	16.6
Mt Etna (Italy)	Basalt 2	0.10	Wet	18.7
Mt Etna (Italy)	Basalt 2	0.07	Wet	18.3
Mt Etna (Italy)	Basalt 2	0.14	Wet	16.1
Chaîne des Puys (France)	Trachyandesite	0.20	Dry	94.6
Chaîne des Puys (France)	Trachyandesite	0.21	Dry	96.4
Chaîne des Puys (France)	Trachyandesite	0.20	Dry	84.2
Chaîne des Puys (France)	Trachyandesite	0.21	Dry	91.1
Chaîne des Puys (France)	Trachyandesite	0.21	Dry	94.8
Chaîne des Puys (France)	Trachyandesite	0.21	Dry	94.7
Chaîne des Puys (France)	Trachyandesite	0.20	Wet	76.3
Chaîne des Puys (France)	Trachyandesite	0.21	Wet	89.4
Chaîne des Puys (France)	Trachyandesite	0.20	Wet	84.9
Chaîne des Puys (France)	Trachyandesite	0.21	Wet	88.2
Chaîne des Puys (France)	Trachyandesite	0.21	Wet	96.6
Chaîne des Puys (France)	Trachyandesite	0.21	Wet	88.0
Volcán de Colima (Mexico)	Andesite 1	0.07	Dry	86.0
Volcán de Colima (Mexico)	Andesite 1	0.07	Dry	80.6
Volcán de Colima (Mexico)	Andesite 1	0.07	Dry	83.3
Volcán de Colima (Mexico)	Andesite 1	0.07	Dry	81.9
Volcán de Colima (Mexico)	Andesite 1	0.07	Dry	76.7
Volcán de Colima (Mexico)	Andesite 1	0.07	Wet	74.8
Volcán de Colima (Mexico)	Andesite 1	0.07	Wet	76.2
Volcán de Colima (Mexico)	Andesite 1	0.07	Wet	78.6
Volcán de Colima (Mexico)	Andesite 1	0.07	Wet	73.6
Volcán de Colima (Mexico)	Andesite 1	0.07	Wet	76.3
Volcán de Colima (Mexico)	Andesite 2	0.21	Dry	24.8
Volcán de Colima (Mexico)	Andesite 2	0.21	Dry	24.9
Volcán de Colima (Mexico)	Andesite 2	0.22	Dry	22.5
Volcán de Colima (Mexico)	Andesite 2	0.22	Dry	20.6
Volcán de Colima (Mexico)	Andesite 2	0.22	Dry	22.5
Volcán de Colima (Mexico)	Andesite 2	0.22	Wet	27.8
Volcán de Colima (Mexico)	Andesite 2	0.21	Wet	29.7
Volcán de Colima (Mexico)	Andesite 2	0.22	Wet	20.7

Table 1 (continued)

Volcano	Rock type	Porosity	Condition	UCS (MPa)
Volcán de Colima (Mexico)	Andesite 2	0.23	Wet	21.5
Volcán de Colima (Mexico)	Andesite 2	0.22	Wet	23.3
Mt Meager (Canada)	BAF	0.11	Dry	56.7
Mt Meager (Canada)	BAF	0.13	Dry	62.8
Mt Meager (Canada)	BAF	0.10	Dry	74.3
Mt Meager (Canada)	BAF	0.11	Dry	63.1
Mt Meager (Canada)	BAF	0.13	Dry	62.9
Mt Meager (Canada)	BAF	0.13	Dry	54.4
Mt Meager (Canada)	BAF	0.12	Dry	68.9
Mt Meager (Canada)	BAF	0.15	Dry	68.3
Mt Meager (Canada)	BAF	0.12	Dry	65.5
Mt Meager (Canada)	BAF	0.11	Dry	66.0
Mt Meager (Canada)	BAF	0.13	Wet	61.1
Mt Meager (Canada)	BAF	0.14	Wet	46.3
Mt Meager (Canada)	BAF	0.14	Wet	52.9
Mt Meager (Canada)	BAF	0.13	Wet	62.7
Mt Meager (Canada)	BAF	0.11	Wet	57.8
Mt Meager (Canada)	BAF	0.12	Wet	59.5
Mt Meager (Canada)	BAF	0.10	Wet	48.0
Mt Meager (Canada)	BAF	0.13	Wet	61.6

sample from Mt Etna decreased at temperatures of 300 °C and above (Rocchi et al. 2004). As discussed in Rocchi et al. (2004), quantities of glass within these samples may explain the observed weakening at high-temperature.

To conclude, experimental studies have shown that (1) the presence of water reduces the strength of tuffs that contain zeolites and clays, but that more experiments are required to understand whether lavas are weaker when wet, (2) decreasing strain rate reduces the strength of volcanic rocks due to the increased time available for time-dependent deformation micromechanisms, (3) thermal stressing decreases the strength of volcanic materials that contain zeolites and/or clays, but that more experiments are required to understand the influence of thermal stressing on the strength of lavas, and (4) high in-situ temperatures can increase the strength of lavas (below their threshold glass transition temperature). Despite the studies outlined above, more data and analyses are now needed to better understand the influence of water, strain rate, thermal stressing temperature, and high in-situ temperature on the strength of volcanic rocks.

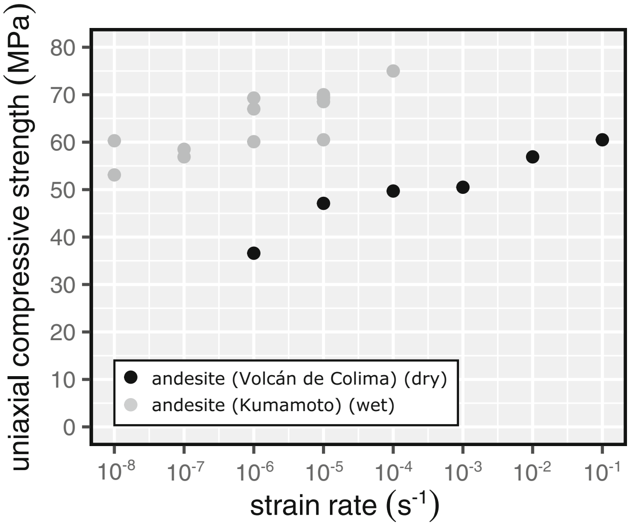

Fig. 9 Uniaxial compressive strength (UCS) as a function of strain rate for andesite from Volcán de Colima (Mexico; data from Lavallée et al. 2019) and Kumamoto andesite (Japan; data unique to this study; Table 2). The andesite from Volcán de Colima was deformed dry and the Kumamoto andesite was deformed wet

Micromechanical modelling: uniaxial compressive strength

Micromechanical models are often employed to gain further insight as to the microstructural attributes that most influence the uniaxial compressive strength of rocks. The two most widely used models were developed for microcracked materials (the “wing-crack” model; Ashby and Sammis 1990), often used for low-porosity rocks, and for materials containing pores (the “pore-crack” model; Sammis and Ashby 1986), often used for high-porosity rocks.

The sliding wing-crack model describes a two-dimensional elastic medium populated with cracks of length $2c$ that are

Table 2 Summary of the data unique to this study used to assess the influence of strain rate on the uniaxial compressive strength (UCS) of volcanic rocks. These samples were first vacuum-saturated in deionised water and then deformed within a water-filled container

Volcano	Rock type	Porosity	Condition	Strain rate (s^{-1})	UCS (MPa)
Kumamoto (Japan)	andesite	0.13	Wet	10^{-8}	60.3
Kumamoto (Japan)	andesite	0.14	Wet	10^{-8}	53.1
Kumamoto (Japan)	andesite	0.13	Wet	10^{-7}	58.5
Kumamoto (Japan)	andesite	0.14	Wet	10^{-7}	56.9
Kumamoto (Japan)	andesite	0.14	Wet	10^{-6}	60.1
Kumamoto (Japan)	andesite	0.13	Wet	10^{-6}	69.3
Kumamoto (Japan)	andesite	0.14	Wet	10^{-6}	67.0
Kumamoto (Japan)	andesite	0.13	Wet	10^{-5}	70.0
Kumamoto (Japan)	andesite	0.13	Wet	10^{-5}	69.3
Kumamoto (Japan)	andesite	0.13	Wet	10^{-5}	69.6
Kumamoto (Japan)	andesite	0.14	Wet	10^{-5}	60.5
Kumamoto (Japan)	andesite	0.14	Wet	10^{-5}	68.5
Kumamoto (Japan)	andesite	0.14	Wet	10^{-4}	75.0
Kumamoto (Japan)	andesite	0.13	Wet	10^{-4}	83.0
Kumamoto (Japan)	andesite	0.13	Wet	10^{-4}	82.1

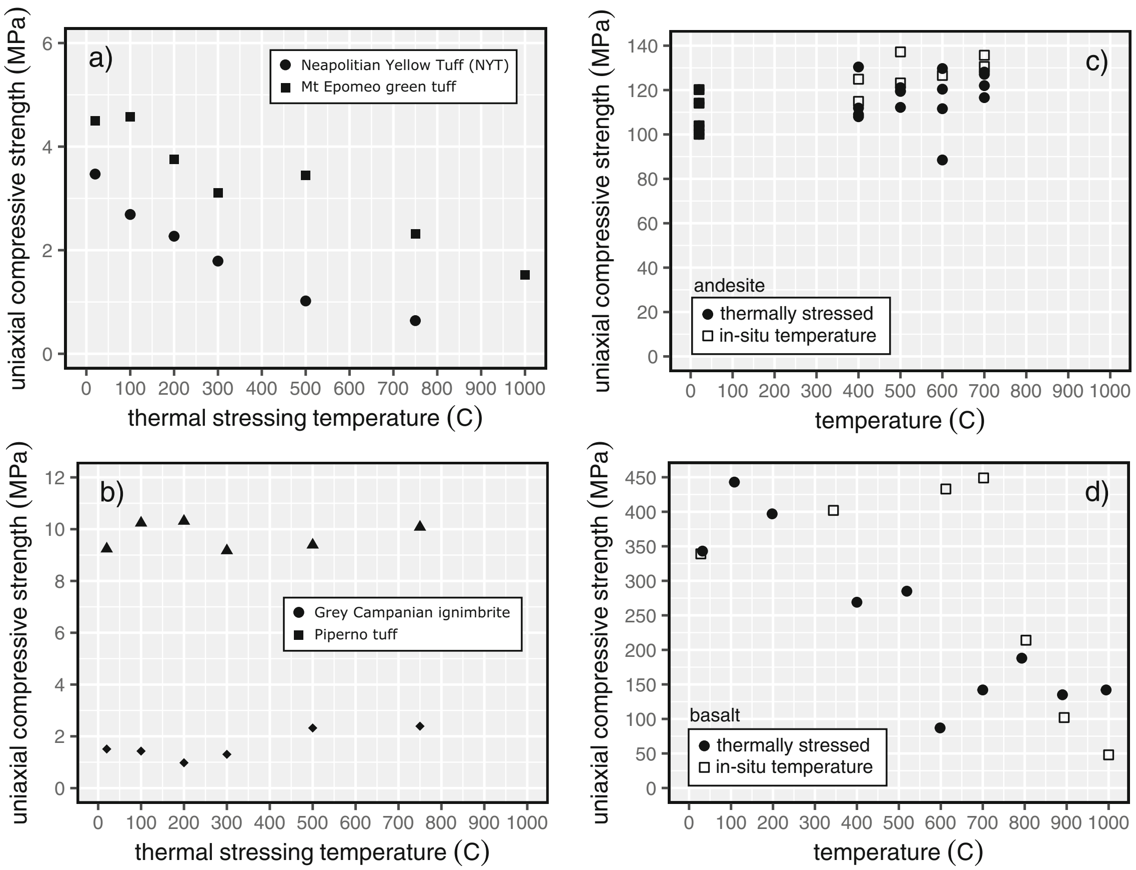

Fig. 10 (**a**) Uniaxial compressive strength (UCS) of tuffs (Neapolitan Yellow Tuff and tuff from Mt Epomeo, both Italy) that contain clays and zeolites as a function of thermal stressing temperature (data from Heap et al. 2012, 2018c). (**b**) UCS of tuffs (Grey Campanian ignimbrite and Piperno tuff, both Italy) that do not contain clays or zeolites as a function of thermal stressing temperature (data from Heap et al. 2012). (**c**) UCS of andesite (Volcán de Colima, Mexico) as a function of thermal stressing temperature (black circles) and in situ temperature (white squares) (data from Heap et al. 2018a). (**d**) UCS of basalt (French Massif Central) as a function of thermal stressing temperature (black circles) and in-situ temperature (white squares) (data from Duclos and Paquet 1991)

aligned at an angle of $\gamma = 45°$ to the maximum principal stress (Fig. 11a). The pore-crack model describes a two-dimensional elastic medium populated with circular pores of a uniform radius, r (Fig. 11b). Once the frictional resistance of the initially closed crack is overcome in the wing-crack model, cracks can propagate to a distance l in a direction parallel to the maximum principal stress when the crack-tip stress reaches the fracture toughness of the material, K_{IC} (Fig. 11a). In the pore-crack model, cracks can propagate to a distance l in a direction parallel to the maximum principal stress when the stress at the tip of a crack on the curved surface of the pore reaches K_{IC} (Fig. 11b). In both models, the cracks eventually grow long enough to interact and ultimately coalesce, resulting in the macroscopic failure of the medium (Fig. 11). Analytical solutions exist for both models. The analytical solution for the wing-crack model can be used to estimate uniaxial compressive strength, σ_p, using the friction coefficient of the sliding crack, μ, the K_{IC} of the material, the crack half-length, c, and an initial damage parameter, D_0, which is a function of the crack angle and density (Baud et al. 2014):

$$\sigma_p = \frac{m}{\sqrt{1+\mu^2}-\mu}\frac{K_{IC}}{\sqrt{\pi c}}{D_0}^{n} \qquad (1)$$

where constants m and n are 1.346 and −0.256, respectively (Baud et al. 2014). In the analytical solution for the pore-crack model, σ_p can be estimated using the pore radius, r, the porosity, ϕ, and K_{IC} of the material (Zhu et al. 2010):

$$\sigma_p = \frac{a}{\phi^b}\frac{K_{IC}}{\sqrt{\pi r}} \qquad (2)$$

where constants a and b are 1.325 and 0.414, respectively (Zhu et al. 2010). Constants a and b are taken from an empirically fitted power law to theoretical predictions of uniaxial compressive strength as a function of porosity (see Zhu et al. (2010) for more details).

The pore-crack and wing-crack models have previously been used to explore the mechanical behaviour of volcanic rocks (e.g. Zhu et al. 2011; Vasseur et al. 2013; Heap et al. 2014a, 2015a, 2016b; Zhu et al. 2016; Coats et al. 2018). The wing-crack model best suits rocks characterised by a microstructure composed of microcracks, usually low-porosity rocks, and the pore-crack model best suits rocks with a microstructure consisting of pores, usually high-porosity rocks. Recent studies that have measured the permeability of volcanic rocks suggest that the porosity at which the microstructure changes from microcrack-dominated to pore-dominated is

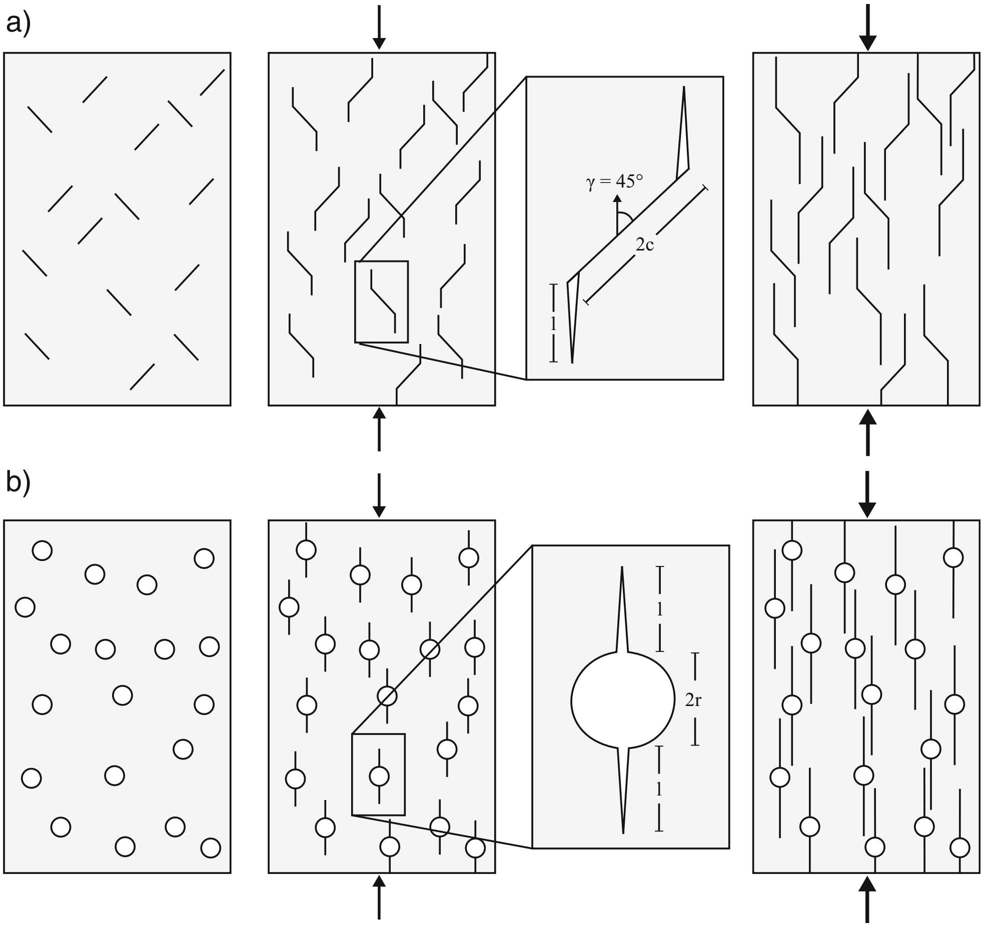

Fig. 11 (**a**) The sliding wing-crack model of Ashby and Sammis (1990), which describes a two-dimensional elastic medium populated with cracks of length $2c$ that are aligned at an angle of $\gamma = 45°$. (**b**) The pore-crack model of Sammis and Ashby (1986), which describes a two-dimensional elastic medium populated with circular pores of a uniform radius, r. Arrows indicate the direction of the maximum principal stress. See text for details

about 0.15 (Heap et al. 2014a; Farquharson et al. 2015; Heap and Kennedy 2016; Kushnir et al. 2016) and so, from these data, we could infer that the wing-crack model should not be used for volcanic rocks with a porosity > 0.15 (further recommendations are described below).

The unknown parameters in the wing-crack (Eq. (1)) and pore-crack (Eq. (2)) models are μ, K_{IC}, c, r, ϕ, and D_0. The average microcrack half-length, c, and the pore radius, r, can be estimated from microstructural observations, and the porosity, ϕ, can be measured in the laboratory (or estimated using image analysis). The friction coefficient for crack sliding, μ, can be estimated using the stress required for the onset of microcracking, C', for a suite of triaxial experiments (Baud et al. 2014):

$$\mu = \frac{d-1}{2\sqrt{d}} \tag{3}$$

where d is the slope of the best-fit linear regression for C' data plotted on a graph of $\sigma_1 - P_p$ as a function of $\sigma_3 - P_p$. Values of μ of 0.5 and 0.55 were estimated for two microcracked basalts from Mt Etna with porosities of 0.047 and 0.05, respectively (Zhu et al. 2016). These values are lower than that estimated for low-porosity granite (μ = 0.71), but within the range estimated for porous sandstones (μ = 0.52–0.67) (Baud et al. 2014).

The initial damage parameter D_0 can be determined using $D_0 = \pi(c\cos\gamma)^2 N_A$, where the mean number of microcracks per unit area, N_A, and the microcrack half-length, c, can be determined using stereological techniques (e.g. Griffiths et al. 2017a). The mean angle of a microcrack to the maximum principal stress, γ, is often assumed to equal 45° in sedimentary (e.g. Baud et al. 2014) and volcanic rocks (e.g. Heap et al. 2014a; Li et al. 2019; Nicolas et al. 2020). Since there is no characteristic microcrack length or number density for volcanic rocks, a rigorous test of whether the wing-crack model can capture the mechanical behaviour of volcanic rock would require that N_A and c are determined for each sample. Although methods exist to automate microcrack analysis (e.g. Griffiths et al. 2017a; Healy et al. 2017), and crack densities can be estimated by inverting elastic wave velocities (e.g. Schubnel et al. 2006), determining microcrack characteristics for a great number of samples will be extremely time-consuming. Alternative methods exist to estimate D_0. First, D_0 can be simply estimated using the wing-crack model (Eq. (1)) if the uniaxial compressive strength and the remaining microstructural parameters are known. D_0 values of 0.14 and 0.16 were estimated using this technique for two microcracked basalts from Mt Etna with porosities of 0.047 and 0.05, respectively (Zhu et al. 2016). Second, D_0 can be estimated using microcrack densities determined using stress-strain data from cyclic stressing experiments (e.g. David et al. 2012; Griffiths et al. 2017a). Third, D_0 can be estimated using the stress required for the onset of microcracking, C' (Fig. 3). According to the wing-crack model, the stress required for the onset of microcracking, $\sigma_{C'}$, should be given by (Ashby and Sammis 1990; Baud et al. 2000a):

$$\sigma_{C'} = \frac{\sqrt{3}}{\sqrt{1+\mu^2}-\mu}\frac{K_{IC}}{\sqrt{\pi c}} \tag{4}$$

Therefore, comparing Eqs. (1) and (4), D_0 can be inferred from $D_0 = 0.777\left(\sigma_{C'}/\sigma_p\right)$. Using this latter technique, Heap et al. (2014a) found values of D_0 of < 0.012 for andesites from Volcán de Colima, values more than an order of magnitude lower than for low-porosity granite (D_0 = 0.13) and porous sandstones and limestones (D_0 = 0.18–0.36) (Baud et al. 2014). These authors concluded that these inferred values of D_0 were too low for these microcracked andesites and, as proposed by Baud et al. (2014), suggested that the microcracks that form at C' may not be those involved in the failure process.

The fracture toughness, K_{IC}, appears in both the wing-crack (Eq. (1)) and pore crack (Eq. (2)) models. We compile here published data for the K_{IC} of volcanic rocks (data are available for basalt, andesite, dacite, and tuff) (Table 3). We also include K_{IC} values for different types of glass and feldspar (microcline, sanidine, and orthoclase) in our compilation. The K_{IC} of other common minerals found in volcanic rocks, such as pyroxene, are, to the authors' knowledge, not yet available. Values of K_{IC} for volcanic rocks vary considerably, from 0.20 to 4.00 MPa.m$^{0.5}$ (Table 3). Although the K_{IC} of volcanic rocks is likely influenced by, for example, porosity and microstructure, we highlight that different techniques and different sample geometries can also lead to different K_{IC} estimations (hence why we report the method used in Table 3). Values of K_{IC} for volcanic rocks are also expected to be influenced by temperature, as discussed in Balme et al. (2004). Increases in K_{IC} are expected as temperature is increased to a couple of hundred degrees Celsius, due to the closure of pre-existing microcracks (see also Meredith and Atkinson 1985), after which K_{IC} is expected to decrease due to thermal microcracking (Balme et al. 2004). Values for glass and feldspar (with the exception of sanidine) are much lower, varying from 0.31 to 1.10 MPa.m$^{0.5}$ (Table 3). Studies that have used the wing-crack and pore-crack models to interpret data for volcanic rocks (e.g. Zhu et al. 2011; Vasseur et al. 2013; Heap et al. 2014a, 2015a, 2016b; Zhu et al. 2016) have used values that represent the K_{IC} of the primary mineral constituent, rather than the K_{IC} of the rock. For example, Zhu et al. (2011) and (2016) used a value of 0.30 MPa.m$^{0.5}$ (that of feldspar) for tuff and basalt, respectively, Vasseur et al. (2013) used a value for glass, 0.70 MPa.m$^{0.5}$, for their sintered glass-bead samples, Heap et al. (2015a) used a value of 0.15 MPa.m$^{0.5}$ for welded block-and-ash flow samples, and Heap et al. (2016b) used 0.2 MPa.m$^{0.5}$ for dacite. The reason for

Table 3 Compiled K_{IC} (fracture toughness) data for volcanic rocks and common volcanic rock-forming minerals. *SR* short-rod method; *DT* double-torsion test; *DC* diametral compression test; *SNDB* straight notched disk bending method; *SENRBB* single edge-notched round bar bending method; *DCL* double cantilever method; *I* indentation method; *CIF* chemically induced fracture method; *MI* microindentation method

Volcano or location	Rock type/mineral	Porosity	K_{IC} (MPam$^{0.5}$)	Error (MPam$^{0.5}$)	Reference	Notes
Seljadur (Iceland)	basalt	0.02	2.17–3.78	0.06–0.42	Balme et al. (2004)	SR; 30–600°C; 1–20 MPa
Vesuvius (Italy)	basalt	0.08	1.50–2.06	0.08–0.10	Balme et al. (2004)	SR; 25-650°C; 1–30 MPa
Mt Etna (Italy)	basalt (core)	0.09	2.18–2.24	0.11	Balme et al. (2004)	SR; 25 °C; 1 MPa
Mt Etna (Italy)	basalt (crust)	0.10	1.29–1.44	0.06–0.07	Balme et al. (2004)	SR; 25 °C; 1 MPa
Preshal More (Scotland)	basalt	-	2.50	0.14	Meredith et al. (1981)	SR
“Britain”	basalt	-	1.8	-	Singh and Pathan (1988)	DC
Ankara (Turkey)	andesite	-	1.00	0.09	Tutluoglu and Keles (2011)	SNDB
Mt Shasta (USA)	andesite	0.07	1.7–4.0	0.2–0.6	Smith et al. (2009)	SR; 25–900°C; dry and wet (wet at 2 MPa)
Kumamoto (Japan)	andesite	0.13	1.66–1.91	0.05–0.21	Nara et al. (2012)	DT; relative humidity 22–87%
Mt Unzen (Japan)	dacite	0.07–0.34	0.3–1.5	-	Scheu et al. (2008)	SR; 500 °C; 0 MPa
Tage (Japan)	tuff	-	0.2–2.75	-	Funatsu et al. (2004)	SENRBB; 25–200°C; 0–9 MPa
-	silica glass	-	0.789–0.798	0.020–0.023	Wiederhorn (1969)	DCL
-	lead alkali glass	-	0.677–0.682	0.011	Wiederhorn (1969)	DCL
-	soda lime glass	-	0.749–0.758	0.011–0.012	Wiederhorn (1969)	DCL
-	aluminosilicate glass	-	0.908–0.913	0.022–0.023	Wiederhorn (1969)	DCL
-	borosilicate glass	-	0.758–0.778	0.010–0.011	Wiederhorn (1969)	DCL
-	microline (001)	-	0.393	-	Atkinson and Avdis (1980)	I
-	microline (010)	-	0.393	-	Atkinson and Avdis (1980)	I
-	microline (110)	-	0.305	-	Atkinson and Avdis (1980)	I
-	sanidine (001)	-	2.72	-	Scheidl et al. (2014)	CIF
-	sanidine (010)	-	2.3	-	Scheidl et al. (2014)	CIF
-	orthoclase (101)	-	0.88	0.13	Broz et al. (2006)	MI
-	orthoclase (101)	-	1.1	0.4	Whitney et al. (2007)	MI

choosing values that represent the rock-forming minerals rather than the rock, which are considerably higher, is that microcracks initiate and propagate within the rock-forming minerals and/or at their grain/crystal boundaries. Strength is also significantly overestimated by the models when the measured values for rocks are used.

The wing-crack model (Eq. (1)) has only been sparingly used in studies on volcanic rocks. For example, Zhu et al. (2016) found that the wing-crack model overestimated the strength of basalts from Mt Etna with porosities of 0.047 and 0.05 by a factor of two. These authors concluded that this discrepancy is likely due to the weakening influence of pores within these materials. Heap et al. (2014a) similarly concluded that, even for a low-porosity andesite (porosity = 0.079), a model that incorporates the influence of both microcracks and pores would be required to describe the observed mechanical behaviour. Because the wing-crack model overestimates the strength of microcracked volcanic rocks with a low porosity, and therefore only a small volume of pores, we suggest, to ensure the absence of pores, that this model should only be used to analyse volcanic rocks with a very low-porosity (<< 0.05). We further note that the wing-crack model contains a number of variables that are difficult to well constrain, especially for volcanic rocks. For example, it is likely that D_0 varies between samples prepared from the same block of volcanic material. We therefore conclude, although the wing-crack model (Eq. (1)) is well-suited to study the mechanical behaviour of microcracked granites, it may not be of considerable use for volcanic rocks, which typically contain pores.

The pore-crack model has been more widely used in studies of the mechanical behaviour of volcanic rocks than the wing-crack model (e.g. Zhu et al. 2011; Vasseur et al. 2013; Heap et al. 2014a, 2015a, 2016b; Zhu et al. 2016; Coats et al. 2018). The reasons for this are twofold. First, studies of the mechanical behaviour of volcanic rocks have thus far largely focused on porous rocks. Furthermore, as highlighted by the studies of Heap et al. (2014a) and Zhu et al. (2016), and described above, even low-porosity volcanic rocks contain pores that influence their mechanical behaviour. Second, the pore-crack model (Eq. (2)) contains fewer variables than the wing crack model (Eq. (1)). Although Eq. (2) can be used to estimate the strength of a particular sample if the porosity, pore radius, and K_{IC} are known, it is more common, and more useful, to see if the pore-crack model can explain the mechanical behaviour of, for example, a suite of rocks of the same rock type or from the same volcano. To do so, Eq. (2) can be used to provide a strength-porosity curve for a value of the term $K_{IC}/\sqrt{\pi r}$ that best describes the data or, and more common, two curves for values of $K_{IC}/\sqrt{\pi r}$ that bracket the experimental data. For example, the values of $K_{IC}/\sqrt{\pi r}$ that bracket our data compilation are 1.5 and 55 MPa (Fig. 12a). The two main reasons why these data cannot be described by a single curve are as follows: (1) these data are for different rock types with different microstructures that are likely characterised by different values of K_{IC} and (2) the samples within the compilation cannot be described by a single pore radius. However, information can still be gleaned from such analysis. For example, if we assume a reasonable minimum and maximum macropore radius of 5 and 500 μm, the range of possible values for K_{IC} is 0.006 and 0.218 MPa.m$^{0.5}$ and 0.059 and 2.180 MPa.m$^{0.5}$, respectively. These ranges for K_{IC} suggest, as stated above, that the representative K_{IC} value for the model is that of the mineral, not the rock (see Table 3). However, since the largest variation in values of K_{IC} is likely related to rock type, it is perhaps sensible to restrict this type of analysis to a single rock type. For example, the compiled data for andesite can be bracketed between $K_{IC}/\sqrt{\pi r}$ values of 3.5 and 40 MPa (Fig. 12b). Possible ranges for values of K_{IC} for andesite, assuming a minimum and maximum macropore radius of 5 and 500 μm, are 0.014 and 0.159 MPa.m$^{0.5}$ and 0.139 and 1.59 MPa.m$^{0.5}$, respectively. Alternatively, if we assume the relevant K_{IC} is that of the mineral constituents (0.7 and 0.3 MPa.m$^{0.5}$ for glass and feldspar, respectively), we can use the available data to provide a range of pore radii that can describe the dataset. If we assume the microcracks are propagating through glass (K_{IC} = 0.7 MPa.m$^{0.5}$), the range of possible pore radii is between 12.7 mm and 97.5 μm. If we assume the K_{IC} of feldspar (K_{IC} = 0.3 MPa.m$^{0.5}$), the range of possible pore radii is between 2.3 mm and 17.9 μm. Even without a thorough microstructural investigation, we can confidently state that the upper limit pore radius estimates using this approach (12.7 and 2.3 mm) are overestimations. However, as stated above, and in published studies, even data

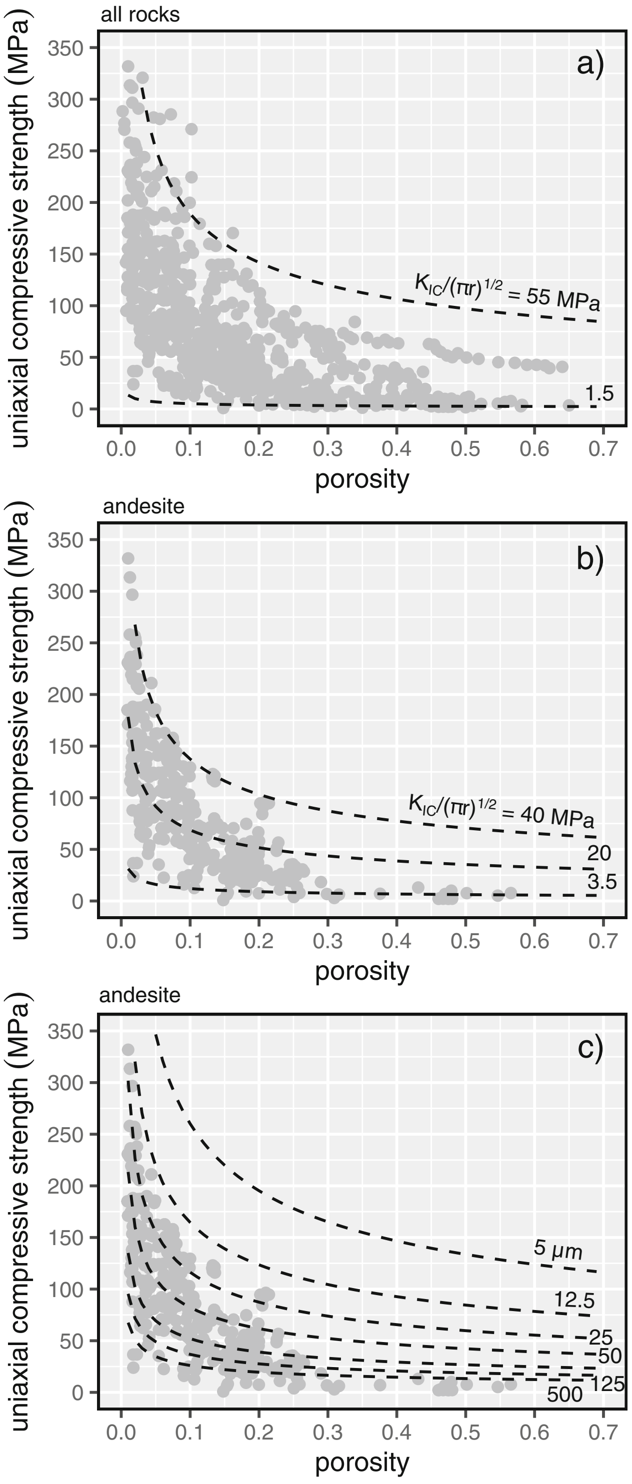

Fig. 12 (**a**) Uniaxial compressive strength (UCS) as a function of porosity for volcanic rocks. Curves were modelled using Eq. (2), using $K_{IC}/(\pi r)^{1/2}$ = 55 and 1.5 MPa (see text for details). (**b**) UCS as a function of porosity for andesite. Curves were modelled using Eq. (2), using $K_{IC}/(\pi r)^{1/2}$ = 40, 20, and 2.5 MPa (see text for details). (**c**) UCS as a function of porosity for andesite. Curves were modelled using Eq. (2), assuming a K_{IC} of 0.3 MPa.m$^{0.5}$ (see text for details). The number next to each curve indicates the pore radius. All these data are provided in a Microsoft Excel© spreadsheet that accompanies this contribution as Supplementary Material). References for the data used in this figure are provided in the caption of Fig. 5

for rocks of the same rock type from the same volcano cannot not described by a single curve defined by the pore-crack model. Therefore, if we assume that the K_{IC} does not differ significantly for a particular rock type, the pore radius must not be constant over the range of porosity studied. This statement is confirmed by microstructural studies: as porosity increases, the pore size also generally increases. We plot in Fig. 12c curves defined by different characteristic pore radii, assuming a constant K_{IC} of 0.3 MPa.m$^{0.5}$. These curves are not inconsistent with andesite samples measured by Heap et al. (2014a) for which the pore radius is well constrained. In the examples provided herein, we have used the values for constants a and b (Eq. (2)) provided by Zhu et al. (2010) (i.e. $a = 1.325$ and $b = 0.414$). To conclude, despite the limitations presented by the pore-crack model, such as assumption of uniform, circular pores and the absence of pre-existing microcracks, insights into the mechanical behaviour of volcanic rocks can be gleaned using this model. Although the formulation of a more complex micromechanical model, described by an elastic medium populated with pores and microcracks or populated with pores with a nonuniform size distribution, is likely required to better capture the mechanical behaviour of volcanic rocks, the pore-crack model of Sammis and Ashby (1986) provides insight invoking only a small number of variables.

The Young's modulus of volcanic rocks

The Young's modulus, or "stiffness", describes the relationship between stress and strain and is therefore an important metric when characterising the mechanical behaviour of a material. The static Young's modulus can be calculated from laboratory stress-strain data (see Fig. 3). Figure 13a shows Young's modulus as a function of porosity for a compilation of volcanic rocks, including andesite, basalt, dacite, and pyroclastic rocks (e.g. tuffs and welded block-and-ash flow deposits). These data are provided in a Microsoft Excel© spreadsheet that accompanies this contribution as Supplementary Material. Figure 13a shows that, similar to the uniaxial compressive strength data (Fig. 5), the Young's modulus of volcanic rocks decreases nonlinearly as a function of increasing porosity and there is considerable scatter in the data. For example, at a porosity of 0.02, the Young's modulus can be as low as ~11 GPa and as high as ~52 GPa (Fig. 13a). As for uniaxial compressive strength, we also note that the range in Young's modulus for a given porosity is reduced as porosity increases (Fig. 13a). Figure 13a also shows that the Young's modulus of a volcanic rock cannot be differentiated solely based on the broad-stroke rock type classifications used here (andesite, basalt, dacite, and pyroclastic rocks) (as discussed in Heap et al. 2020b), although we note that pyroclastic rocks are often characterised by a low Young's modulus (likely due to their high porosity) and that some basalts have a higher Young's modulus than their porosity would suggest. We also provide a plot of Young's modulus as a function of uniaxial compressive strength (Fig. 13b). Figure 13b shows that the Young's modulus of a volcanic rock increases as a function of increasing uniaxial compressive strength. This trend is very well defined for volcanic rocks with a low strength (< 10 MPa) and poorly defined for rock with a strength > 10 MPa (Fig. 13b). The scatter in the data of Fig. 13 is the result of differences in hydrothermal alteration, crystal contact, groundmass crystallinity, and the nature of the void space (proportion of pores and microcracks and their geometrical properties), as discussed above for uniaxial compressive strength (the influence of these factors on Young's modulus are also discussed in the review of Heap et al. 2020b).

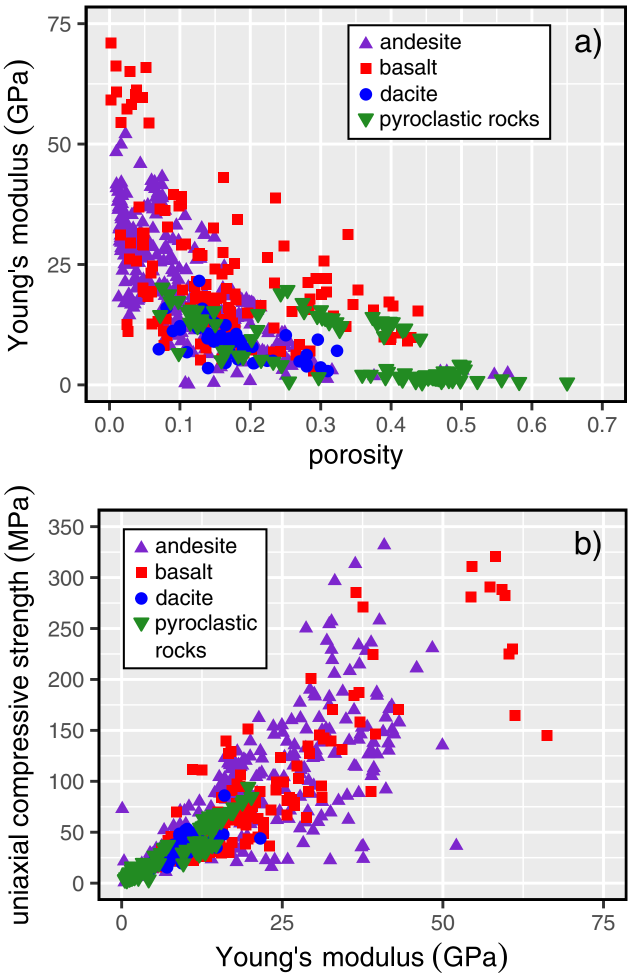

Fig. 13 (**a**) Young's modulus as a function of porosity for volcanic rocks (andesite, basalt, dacite, and pyroclastic rocks). (**b**) Uniaxial compressive strength (UCS) as a function of Young's modulus for volcanic rocks (andesite, basalt, dacite, and pyroclastic rocks). All these data are provided in a Microsoft Excel© spreadsheet that accompanies this contribution as Supplementary Material. References for the data used in this figure are provided in the caption of Fig. 5

The Young's modulus data shown in Fig. 13 are relevant for the sample lengthscale (several tens of centimetres). The

Young's modulus of a volcanic rock mass will, typically, be lower than laboratory-measured values because meso- and macro-scale fractures serve to reduce Young's modulus (as reviewed in Heap et al. 2020b). One method to upscale laboratory measurements of Young's modulus, E_i, to the rock-mass scale is to use the Hoek-Diederichs equation (Hoek and Diederichs 2006):

$$E_{rm} = E_i \left(0.02 + \frac{1}{1 + \exp\left(\frac{60 - GSI}{11}\right)} \right) \qquad (5)$$

where E_{rm} is the rock-mass Young's modulus and GSI is the Geological Strength Index. The GSI is a unitless parameter that depends on the structure of the rock-mass (fracture density) and fracture surface conditions (fracture roughness, weathering, and filling type) (see Heap et al. (2020b) for a GSI chart for volcanic rock-masses). In the absence of a GSI estimate for a particular volcanic rock-mass, Heap et al. (2020b) recommend to use a value of 55. The Young's modulus of volcanic rocks, and the upscaling of Young's modulus to the rock-mass scale, was the subject of a recent review paper (Heap et al. 2020b) and we refer the reader to this contribution for further discussion on the Young's modulus of volcanic rocks and rock-masses.

Mechanical behaviour and failure modes under triaxial conditions

Hydrostatic compaction

The deformation of rock during hydrostatic loading (i.e. $\sigma_1 = \sigma_2 = \sigma_3$) yields valuable mechanical information. The metric of interest in studies of rock deformation is often the effective pressure required for hydrostatic inelastic compaction, termed P^* (e.g. Zhang et al. 1990; Menéndez et al. 1996; Wong and Baud 2012), but the evolution of the volumetric strain (i.e. porosity) during hydrostatic loading can also be used to estimate the microcrack porosity and pore compressibility. Figure 14 shows a graph of porosity reduction as a function of increasing effective pressure for a sample of andesite from Volcán de Colima with a porosity of 0.238. The pore fluid (deionised water) pressure was held at a constant 10 MPa during this experiment, and the porosity change was monitored using a servo-controlled pore fluid pressure pump. The confining pressure was increased in a stepwise manner and the sample was only subject to the next confining pressure increment once the microstructure had equilibrated (i.e. when the porosity had stopped decreasing at a given confining pressure). The decrease in porosity as a function of increasing effective pressure is initially non-linear (Fig. 14), a consequence of the closure of pre-existing microcracks. The microcrack porosity can be estimated using this non-linear portion of the curve, which is about 0.01 for the sample shown in Fig. 14 (see the dashed line). Porosity loss as a function of increasing effective pressure is linear (elastic) until a threshold effective pressure, P^*, where the rate of porosity reduction increases dramatically which, for this sample, occurred at 140–150 MPa (Fig. 14). Microstructurally, this pressure represents that required for the cataclastic collapse of pores within the sample, examples of which are shown in Fig. 15 (see also the pioneering work of Shimada 1986). Experimental studies have shown that the elastic compaction of volcanic rock under hydrostatic conditions results in an isotropic increase in elastic wave velocities (unless the rock is initially anisotropic), considered to be the result of the closure of pre-existing microcracks (e.g. Vinciguerra et al. 2005; Stanchits et al. 2006; Fortin et al. 2011; Nara et al. 2011; Adam and Otheim 2013). Loaiza et al. (2012) showed that the permeability of a sample of trachyandesite from the Açores decreased during the elastic compaction phase (as observed in many other studies; e.g. Vinciguerra et al. 2005, Fortin et al. 2011; Nara et al. 2011; Kolzenburg et al. 2012; Lamur et al. 2017; Heap et al. 2018d; Cant et al. 2018; Kennedy et al. 2020; Eggertsson et al. 2020; Austria and Benson 2020), but then increased following P^*. By contrast, Heap et al. (2014c) found that the permeability of two tuffs from Campi Flegrei (Italy) continued to decrease at pressures above P^*. The deformation of volcanic rock during hydrostatic loading (Fig. 14) is qualitatively similar to that observed for sandstones (e.g. David et al. 1994; Wong et al. 1997; Baud et al. 2006) and limestones (e.g. Vajdova et al. 2004).

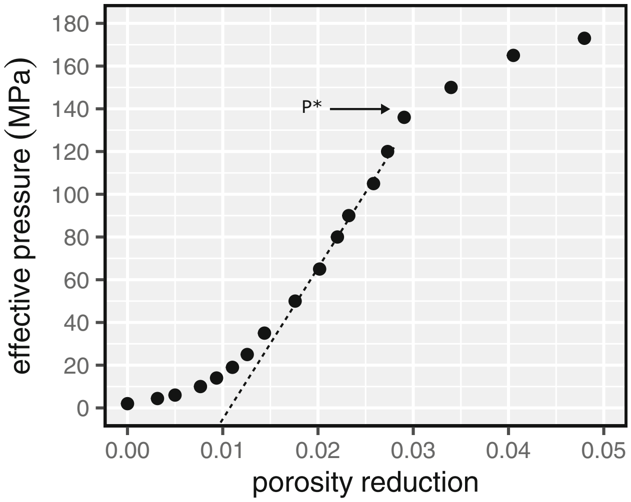

Fig. 14 Porosity reduction as a function of increasing effective pressure for a sample of andesite from Volcán de Colima (Mexico) with a porosity of 0.238. The onset of inelastic compaction, P^*, is indicated on the curve. The initial microcrack porosity within the sample can be estimated by extrapolating the linear elastic portion of the curve to 0 MPa (the dashed line). The microcrack porosity within this sample is about 0.01. Data from Heap et al. (2015b)

Hydrostatic experiments on volcanic rocks are very rare, and are biased towards porous pyroclastic rocks. We compile

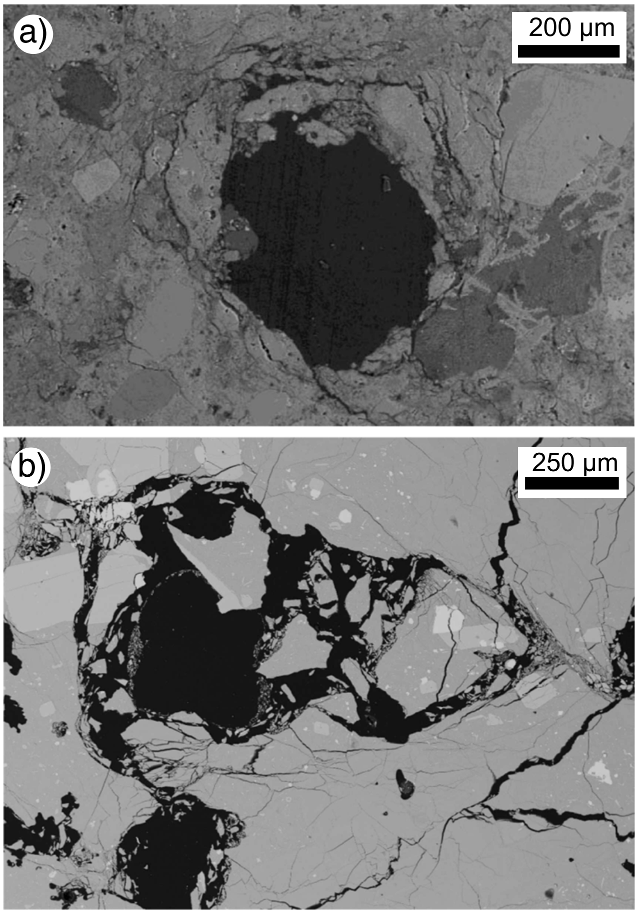

Fig. 15 Scanning electron microscope (SEM) images of a collapsed pore within (**a**) a sample of tuff from Alban Hills (Italy) (from Zhu et al. 2011) and (**b**) a sample of andesite from Volcán de Colima (Mexico) (from Heap et al. 2015b) following hydrostatic compaction beyond P^*

P^* data for volcanic rocks in Table 4. The effective pressure required for P^* is plotted as a function of porosity for volcanic rocks in Fig. 16a (data in Table 4). These data show that the pressure required for P^* decreases non-linearly as a function of increasing porosity, as observed for porous sedimentary rocks (Wong and Baud 2012). For the data shown in Fig. 16a, the reduction in P^* as porosity is increased from 0.07 to 0.35 is large, and reductions as porosity increases above 0.35 are small. Although the same non-linear trend is observed for sedimentary rocks (Wong and Baud 2012), we note here that, for this dataset of volcanic rocks, this porosity also marks the transition from lavas to granular volcanic rocks (Fig. 16a; Table 4). Rock type may therefore play a role in dictating P^* in volcanic rocks, but more experiments are now required to test this hypothesis.

Although the data of Fig. 16a suggests a first-order role for porosity in dictating P^*, other microstructural parameters have been shown to influence P^* in sedimentary rocks, such as grain size, clay content, the presence of bedding, and cementation (e.g. Wong et al. 1997; Tembe et al. 2008). For example, assuming that the pre-existing flaw dimension scales with the grain radius r, the Hertzian contact model of Zhang et al. (1990) implies that P^* scales with the porosity, ϕ, and the grain radius such that $P^* \propto (\phi r)^{-3/2}$. Indeed, the slope of compiled data on a graph of P^* as a function of the porosity multiplied by the grain radius is approximately –3/2 (e.g. Wong et al. 1997; Wong and Baud 1999). However, a Hertzian contact model would only be relevant for granular volcanic rocks, such as tuffs. Unfortunately, (1) the grain radius distribution is often very large in tuffs and it is difficult therefore to provide a grain radius for the above expression and (2) inelastic hydrostatic compaction in tuffs is the result of pore collapse rather than grain crushing (e.g. Zhu et al. 2011). Nevertheless, it is likely that parameters such as grain size and clay content influence P^* in granular volcanic rocks. For example, the P^* of Neapolitan Yellow Tuff, which contains abundant zeolites and clay, is lower than that for the Grey Campanian Ignimbrite (Heap et al. 2014c), despite its higher porosity (Table 4). The P^* of lavas (i.e. non-granular volcanic rocks), however, is likely influenced by pore size, shape, and distribution, factors that vary far more in volcanic rocks than in sedimentary rocks. For example, despite its higher porosity, the P^* of andesite LAH4 is higher than that for andesite C8 (Table 4) and could be explained by its higher average equivalent pore radius (Heap et al. 2014a). The stress required for the onset of P^* is also influenced by the presence of water, as shown for porous sedimentary rocks (e.g. Wong and Baud 2012). So far, experiments have shown that the P^* of tuff from the Alban Hills is reduced from 56 to 28 MPa by the presence of water (Zhu et al. 2011; Fig. 16b; Table 4). More experiments are now required to better understand the influence of porosity, microstructural differences, and the presence of water on P^* in volcanic rocks.

By considering the stresses required to yield a single macropore embedded within an effective medium, and by adopting the Mohr-Coulomb failure criterion, P^* is related to uniaxial compressive strength of the medium, $\sigma_p{}^*$, by (Zhu et al. 2011, 2016):

$$P^* = 2\sigma_p{}^*/3 \tag{6}$$

Figure 16c shows P^* as a function of uniaxial compressive strength for volcanic rocks (Table 4). All of these data plot above the theoretical line delineated by Eq. (6). In other words, the strength of the proposed effective medium overestimates the strength of these volcanic rocks. As pointed out in the studies by Zhu et al. (2011, 2016), this is likely because the pores within volcanic rocks are surrounded by a groundmass or matrix that contains micropores and microcracks that serve to lower the strength of these materials.

To investigate the influence of micropores on the onset of inelastic hydrostatic compaction in porous tuff, Zhu et al. (2011) combined Eq. (6) with that of the pore-crack model (Eq. (2)) to yield:

Table 4 Compiled data for the effective pressure required for the onset of hydrostatic inelastic compaction, P^*. Asterisk indicates an estimated pressure

Volcano	Rock type	Porosity	Condition	P*	Reference
Volcán de Colima (Mexico)	andesite C8	0.17	wet	126	Heap et al. (2015b)
Volcán de Colima (Mexico)	andesite C8	0.17	wet	152	Heap et al. (2015b)
Volcán de Colima (Mexico)	andesite LAH4	0.24	wet	161	Heap et al. (2015b)
Volcán de Colima (Mexico)	andesite LAH4	0.24	wet	150	Heap et al. (2015b)
Açores (Portugal)	trachyandesite	0.18	wet	222	Loaiza et al. (2012)
Volvic (France)	trachyandesite	0.21	wet	250*	This study
Neapolitan Yellow Tuff (Italy)	tuff	0.44	wet	10	Heap et al. (2014c)
Grey Campanian ignimbrite (Italy)	tuff	0.49	wet	15	Heap et al. (2014c)
Whakaari (New Zealand)	tuff	0.31	wet	110	Heap et al. (2015c)
Whakaari (New Zealand)	tuff	0.33	wet	39	Heap et al. (2015c)
Mt Epomeo green tuff (Italy)	tuff	0.43	dry (air)	11	Marmoni et al. (2017)
Alban Hills (Italy)	tuff	0.32	wet	41	Zhu et al. (2011)
Alban Hills (Italy)	tuff	0.36	wet	35	Zhu et al. (2011)
Alban Hills (Italy)	tuff	0.35	wet	28	Zhu et al. (2011)
Alban Hills (Italy)	tuff	0.33	dry (air)	60	Zhu et al. (2011)
Alban Hills (Italy)	tuff	0.36	dry (air)	56	Zhu et al. (2011)
Calico Hills (USA)	tuff	0.22	dry (argon gas)	122	Lockner and Morrow (2008)
Calico Hills (USA)	tuff	0.29	dry (argon gas)	120	Lockner and Morrow (2008)
Calico Hills (USA)	tuff	0.38	dry (argon gas)	44	Lockner and Morrow (2008)
Calico Hills (USA)	tuff	0.43	dry (argon gas)	32	Lockner and Morrow (2008)
Calico Hills (USA)	tuff	0.51	dry (argon gas)	22	Lockner and Morrow (2008)
Mt St Helens (USA)	dacite	0.31	wet	55	Heap et al. (2016b)
Reykjanes (Iceland)	basalt	0.10	wet	400*	Adelinet et al. (2013)
Reykjanes (Iceland)	basalt	0.12	wet	300*	Zhu et al. (2016)
Yakuno (Japan)	basalt	0.07	dry	400	Shimada (2000)
Krafla (Iceland)	Hyaloclastite	0.397	wet	23	Eggertsson et al. (2020)

$$P^* = \frac{0.883}{\phi^{0.414}} S^* \tag{7}$$

where

$$S^* = \frac{K_{IC}}{(\phi_*/\phi)^{0.414}\sqrt{\pi a^*}} \tag{8}$$

where a^* is the average radius of a micropore, ϕ_* is the porosity of the effective medium, and S^* captures the co-operative influence of the fracture toughness, micropore radius, and the partitioning of macro- and microporosity (Zhu et al. 2011). This model describes a dual porosity medium containing a macropore surrounded by micropores. We find that the values of S^* that best bracket the data for compiled data for porous tuffs are ~12 and ~75 MPa (Fig. 16a). For lavas, S^* is between ~100 and ~170 MPa (Fig. 16a). The average micropore radius can then be estimated using $a^* > (K_{IC}/S^*)^2/\pi$ (Zhu et al. 2011). Assuming K_{IC} = 0.3 MPa.m$^{0.5}$ (that for feldspar; Table 3), the average micropore radius for the porous tuffs is between ~5 and ~200 μm, radii not inconsistent with the microstructure of these tuffs (e.g. Zhu et al. 2011; Heap et al. 2014c, 2015c; Marmoni et al. 2017). We note that, if we use a K_{IC} = 0.7 MPa.m$^{0.5}$ (that for glass; Table 3), we retrieve an unrealistic upper average micropore radius estimate above 1 mm. For the lavas (andesite, basalt, dacite), the average micropore radius using the same technique is estimated to be between ~1 and ~3 μm for a K_{IC} = 0.3 MPa.m$^{0.5}$ and between ~5 and ~16 μm for a K_{IC} = 0.7 MPa.m$^{0.5}$. These micropore size predictions are not unreasonable based on pore size distributions for the andesites from Volcán de Colima provided by Heap et al. (2014a). The modelling described above therefore highlights a potentially important role for micropores in controlling the onset of inelastic hydrostatic compaction in volcanic rocks.

Triaxial deformation experiments

Brittle triaxial deformation experiments Stress-strain curves, porosity reduction as a function of strain, and the output of

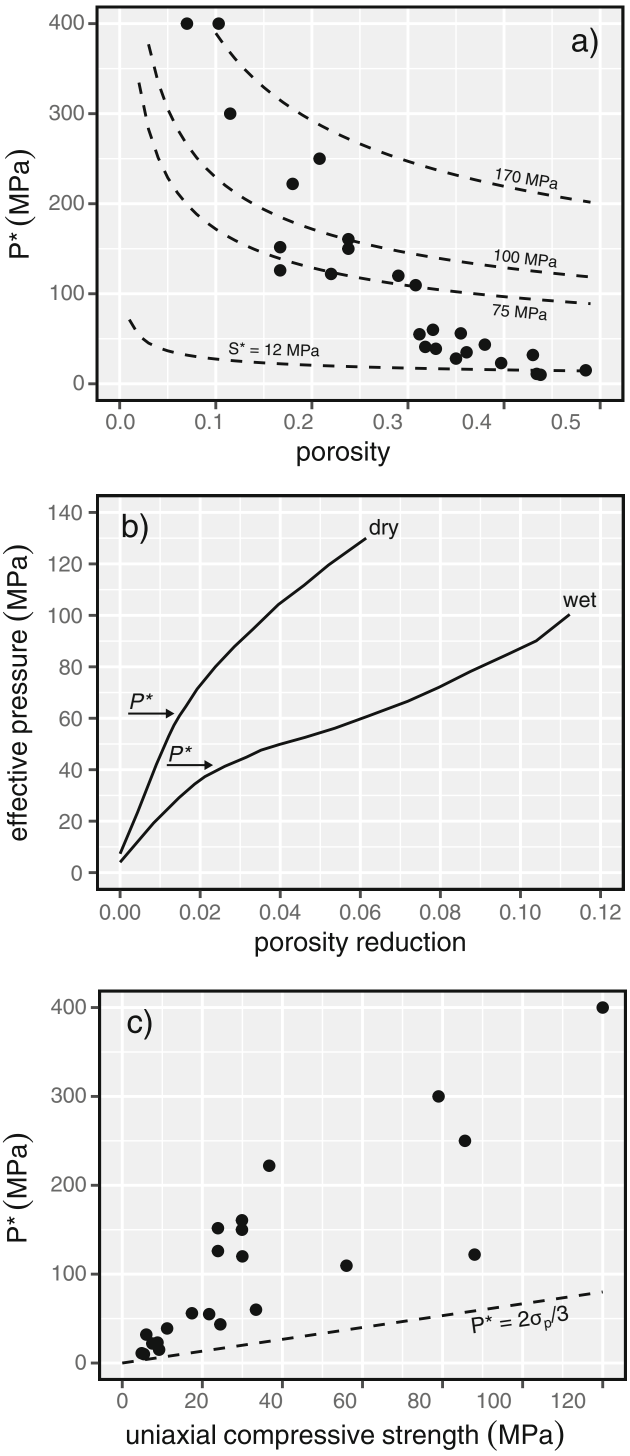

Fig. 16 (**a**) The effective pressure required for the onset of hydrostatic inelastic compaction, P^*, as a function of porosity (data and references provided in Table 4). Dashed curves are drawn using Eq. (8), see text for details. (**b**) Porosity reduction as a function of increasing effective pressure for dry and wet samples of tuff from Alban Hills (Italy). The onset of inelastic compaction, P^*, is indicated on each curve. Data from Zhu et al. (2011). (**c**) The effective pressure required for the onset of hydrostatic inelastic compaction, P^*, as a function of uniaxial compressive strength (data and references provided in Table 4). Dashed curve is that predicted by Eq. (6), see text for details

acoustic emission energy (the area under the received waveform, in arbitrary units) for triaxial deformation experiments performed over a range of effective pressures (up to 140 MPa) are shown in Figs. 17 and 18. So that we can best describe their features, the brittle experiments are provided in Fig. 17 (effective pressures between 0 and 50 MPa) and the ductile experiments in Fig. 18 (effective pressures between 60 and 140 MPa). The data of Figs. 17 and 18, unique to this review, are for a porous trachyandesite from Volvic (Chaîne des Puys, France) with a porosity of 0.208 (see Table 5 for an experimental summary). These samples were deformed at room temperature, under saturated (deionised water) conditions, and at a constant strain rate of 10^{-5} s^{-1}. Differences between hydrostatic ($\sigma_1 = \sigma_2 = \sigma_3$) loading and non-hydrostatic ($\sigma_1 > \sigma_2 = \sigma_3$) loading are best observed on a graph of effective mean stress ($P = (\sigma_1 + 2\sigma_3)/3 - P_p$) as a function of porosity reduction (Fig. 19). Deviations from the curve defined by the hydrostatic experiment indicate the stress required for inelastic behaviour in a particular experiment. Deviations to the left (i.e. increases in porosity) are the result of dilatational microcracking in the brittle field and the stress required for this transition to inelastic behaviour is termed C' (see Wong and Baud 2012). Deviations to the right (i.e. decreases in porosity) are the result of shear-enhanced compaction in the ductile field and the stress required for this transition to inelastic behaviour is termed C^* (see Wong and Baud 2012).

We first remark that the shape of the stress-strain curves for the samples deformed at low pressure (up to 30 MPa; Fig. 17a) are qualitatively similar to the uniaxial stress-strain curve described above (Fig. 3). As effective pressure is increased, the initial non-linear stage of the stress-strain curve shortens and the slope of the stress-strain curve (i.e. the Young's modulus) increases, both due to the closure of microcracks and other defects as effective pressure is increased. The stress-strain curves for the samples deformed at effective pressures of 40, 50, and 60 MPa are noticeably different from those for lower effective pressures (Fig. 17a): the magnitude of the stress drop associated with shear fracture formation is much reduced. Figure 17a also shows that compressive strength increases as a function of increasing effective pressure. Samples at all effective pressures first compacted, due to the closure of pre-existing microcracks and other defects, the rate of which reduced following the onset of dilational microcracking, C' (Fig. 17b). The onset of inelastic behaviour, dilational microcracking, is signalled by the deviation from the hydrostatic experiment (indicating that nonhydrostatic loading has resulted in an increase in sample porosity; Fig. 19) and the onset of AE activity (Fig. 17c). The stress required for the onset of dilational microcracking increased as the effective pressure was increased (Fig. 17b). The samples deformed at an effective pressure up to 30 MPa eventually entered a phase

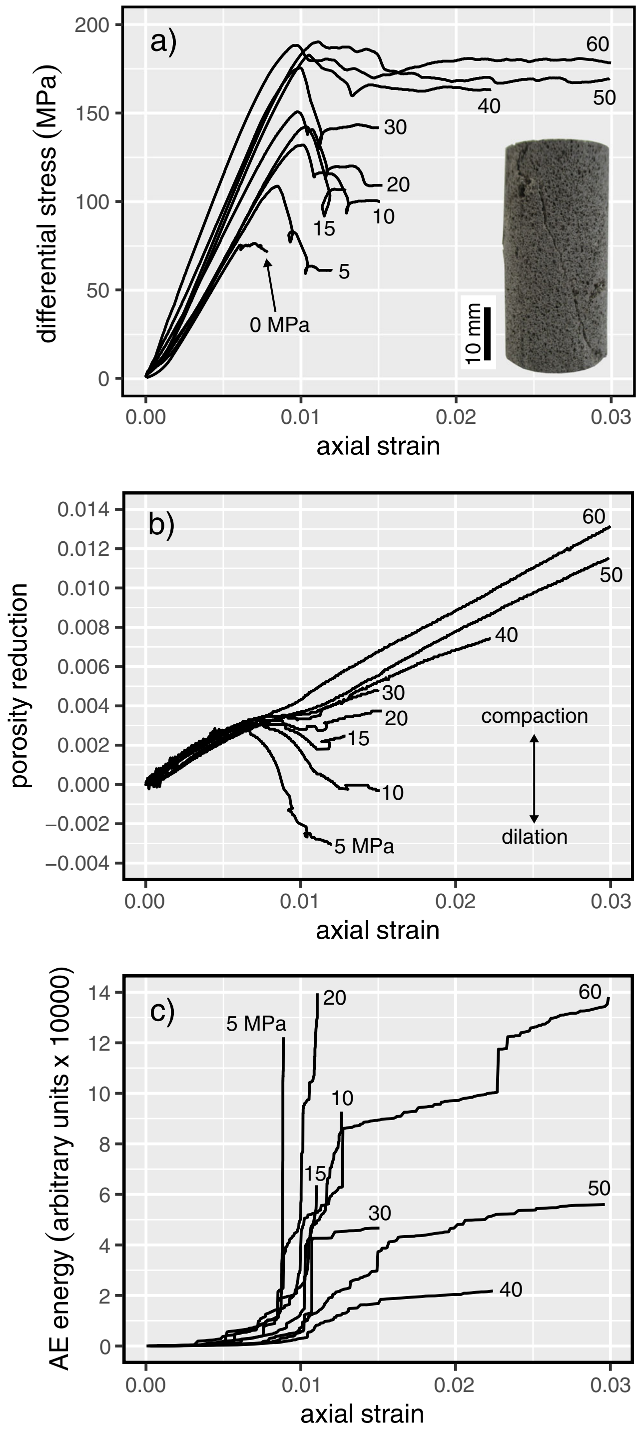

Fig. 17 Triaxial deformation experiments performed on Volvic trachyandesite in the brittle regime. (**a**) Stress-strain curves. The inset shows a post-mortem experimental sample containing a throughgoing shear fracture. (**b**) Porosity reduction as a function of axial strain. (**c**) Output of acoustic emission (AE) energy as a function of axial strain. The number next to each curve indicates the experimental effective pressure

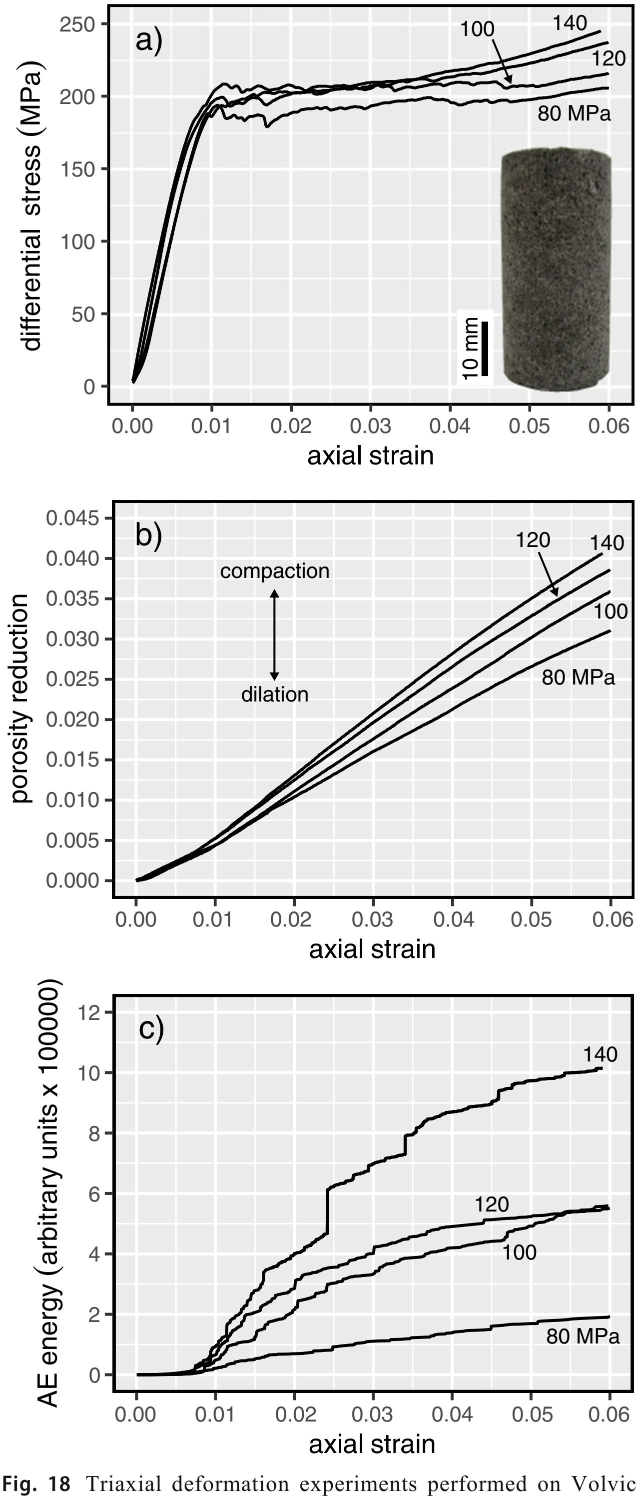

Fig. 18 Triaxial deformation experiments performed on Volvic trachyandesite in the ductile regime. (**a**) Stress-strain curves. The inset shows a post-mortem experimental sample containing compaction bands. (**b**) Porosity reduction as a function of axial strain. (**c**) Output of acoustic emission (AE) energy as a function of axial strain. The number next to each curve indicates the experimental effective pressure

of net dilation. Dilation continued until the end of the experiment for the samples deformed at effective pressures of 5 and 10 MPa; however, samples deformed at effective pressures of 15, 20, and 30 MPa re-entered a phase of net compaction as axial strain increased (Fig. 17b). Samples deformed at effective pressures of 40, 50, and 60 MPa did not enter a phase of

Table 5 Summary of the triaxial experimental data for Volvic trachyandesite (data unique to this study). The peak differential stress maps out the brittle failure envelope and C* (the onset of shear-enhanced compaction) maps of the compactive yield cap

Connected porosity	Confining pressure (MPa)	Pore fluid pressure (MPa)	Effective pressure (MPa)	Effective mean stress, P (MPa)	Peak differential stress (MPa)	Differential stress at C* (MPa)
0.212	15	10	5	41.1	108.3	-
0.211	20	10	10	53.8	131.3	-
0.211	25	10	15	62.5	142.4	-
0.208	30	10	20	70.2	150.7	-
0.209	40	10	30	87.0	171.1	-
0.210	40	10	30	88.5	175.6	-
0.208	50	10	40	100.9	182.8	-
0.211	60	10	50	113.3	190.0	-
0.209	70	10	60	122.8	188.3	-
0.209	90	10	80	137.3	-	172.0
0.213	110	10	100	152.3	-	157.0
0.210	130	10	120	165.3	-	136.0
0.210	150	10	140	178.9	-	116.7

net dilation and, following a slight reduction in the rate of compaction as a function of increasing axial strain, continued to compact until the end of the experiment. The output of acoustic emissions, a proxy for microcrack initiation and growth, accelerated as the samples approached their peak stress (Fig. 17c). In the experiments deformed at effective pressures from 5 to 20 MPa, macroscopic sample failure is marked by a high acoustic emission energy output (Fig. 17c). The acoustic emission energy at the peak stress is less for the samples deformed at effective pressures of 30, 40, 50, and 60 MPa and, following the peak stress, acoustic emission activity continued, but at a reduced rate as a function of increasing axial strain (Fig. 17c). We also highlight that the output of acoustic emission energy increased as the effective pressure was increased from 40 MPa to 60 MPa (Fig. 17c). The triaxial mechanical data for trachyandesite provided in Fig. 17 are qualitatively similar to triaxial data presented for other trachyandesites (e.g. Loaiza et al. 2012; Zorn et al. 2018) and other volcanic rock types, such as basalt (e.g. Stanchits et al. 2006; Heap et al. 2011; Adelinet et al. 2013; Zhu et al. 2016), dacite (e.g. Kennedy et al. 2009; Smith et al. 2011; Kennedy and Russell 2012; Heap et al. 2016b; Ryan et al. 2020), andesite (e.g. Smith et al. 2009; Heap et al. 2015b; Siratovich et al. 2016; Farquharson et al. 2016), and tuff (e.g. Zhu et al. 2011; Heap et al. 2015c) in the brittle regime.

Triaxial deformation experiments on volcanic rocks in which elastic wave velocities were measured in more than one direction highlight that dilatational microcracking and shear fracture formation not only reduce elastic wave velocities, but that they also develop an elastic wave velocity anisotropy (e.g. Stanchits et al. 2006; Ougier-Simonin et al. 2011; Fortin et al. 2011; Adelinet et al. 2013; Harnett et al. 2018a; Li et al. 2019; Austria and Benson 2020). Fortin et al. (2011) showed that, for a low-porosity basalt deformed under an effective pressure of 20 MPa, permeability decreased and then increased as the sample approached macroscopic failure. Farquharson et al. (2016) showed that the permeability of three volcanic rocks (one basalt and two andesites) deformed under an effective pressure of 10 MPa increased as a function of increasing strain. These authors found that the shear band increased in width as a function of increasing strain and that permeability increased by up to three orders of magnitude at inelastic axial strains of about 0.11 (Farquharson et al. 2016). Increases in permeability following shear fracture formation were also reported for andesite from Volcán de Colima deformed at an effective pressure of 10 MPa (Heap et al. 2020a).

Macroscopic failure in the samples of trachyandesite deformed at effective pressures between 0 and 60 MPa was manifest as throughgoing shear fractures (see inset on Fig. 17a) and so, even though differences exist in their stress-strain behaviour, porosity evolution, and AE activity (Fig. 17), all of these experiments are classified as brittle. Fault propagation velocities between 2 and 4 mm.s^{-1} have been estimated using AE locations during the failure of a sample of basalt from Mt Etna deformed at an effective pressure of 40 MPa (Benson et al. 2007). Microstructurally, the shear fractures that typically form during brittle triaxial experiments (Fig. 20) are not dissimilar to those formed under uniaxial compression (Fig. 4), although their angle with respect to the maximum principal stress is increased from sub-parallel (~0°) to ~30° (e.g. Zhu et al. 2016). Although microstructural analysis of deformed sandstone samples has shown that deformation was more localised at higher effective pressures (from 5 to 30 MPa) (e.g. Rizzo et al. 2018), no such analysis currently exists for volcanic rocks. Insights into strain localisation in the brittle regime have been recently provided by digital volume

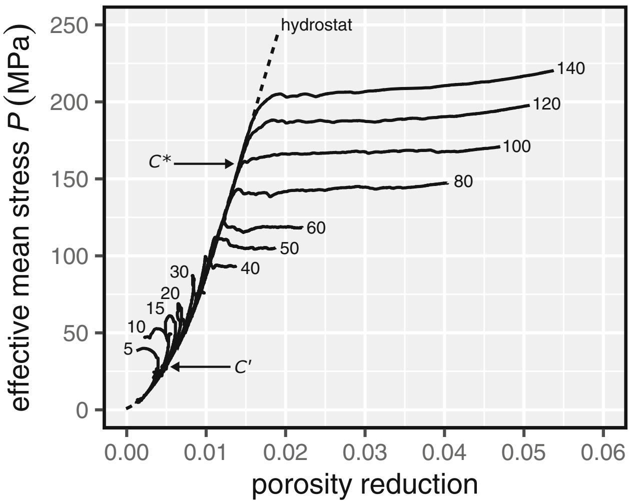

Fig. 19 Effective mean stress as a function of porosity reduction for the triaxial experiments performed on Volvic trachyandesite (the experiments shown in Figs. 17 and 18). The number next to each curve indicates the experimental effective pressure

correlation analysis performed on X-ray tomographic images (McBeck et al. 2019; Heap et al. 2020a). McBeck et al. (2019) analysed the failure of a low-porosity basalt from Mt Etna deformed under an effective pressure of 10 MPa. These authors found that, prior to macroscopic failure, whereas high dilation and shear strains were concentrated within the zone that hosted the largest fracture network at about 50% of the failure stress, high contractive strains concentrated within the other zones of the sample. Heap et al. (2020a) studied the failure of a high-porosity andesite from Volcán de Colima deformed under an effective pressure of 10 MPa. These authors found that the shear fracture was oriented at an angle of 40–45° to the maximum principal stress, formed within a high-porosity zone of the sample, had a width of ~1 mm, and was characterised by an increase in porosity (Fig. 20c; Heap et al. 2020a).

Ductile triaxial deformation experiments The shape of the stress-strain curves for the samples deformed at high pressure (up to 140 MPa; Fig. 18a) are noticeably different to those of the low-pressure experiments (Fig. 17a). There is no stress drop characteristic of shear fracture formation and, following an axial strain of about 0.04, the differential stress increases as a function of increasing strain, a phenomenon termed "strain hardening". There are, however, small stress drops in these stress-strain curves between an axial strain of about 0.01 to about 0.02 (Fig. 18a). These stress drops are typically indicative of the formation of compaction bands (e.g. Baud et al. 2004; Adelinet et al. 2013; Heap et al. 2015b), discussed in more detail below. All of the samples compacted throughout the experiments, the rate of which increased at the onset of inelastic compaction, C* (Fig. 18b). The onset of inelastic behaviour, cataclastic pore collapse, is signalled by the deviation from the hydrostatic experiment (indicating that nonhydrostatic loading has resulted in a decrease in sample porosity; Fig. 19) and the onset of AE activity (Fig. 18c). The porosity loss for a given axial strain (Fig. 18b) and the rate of

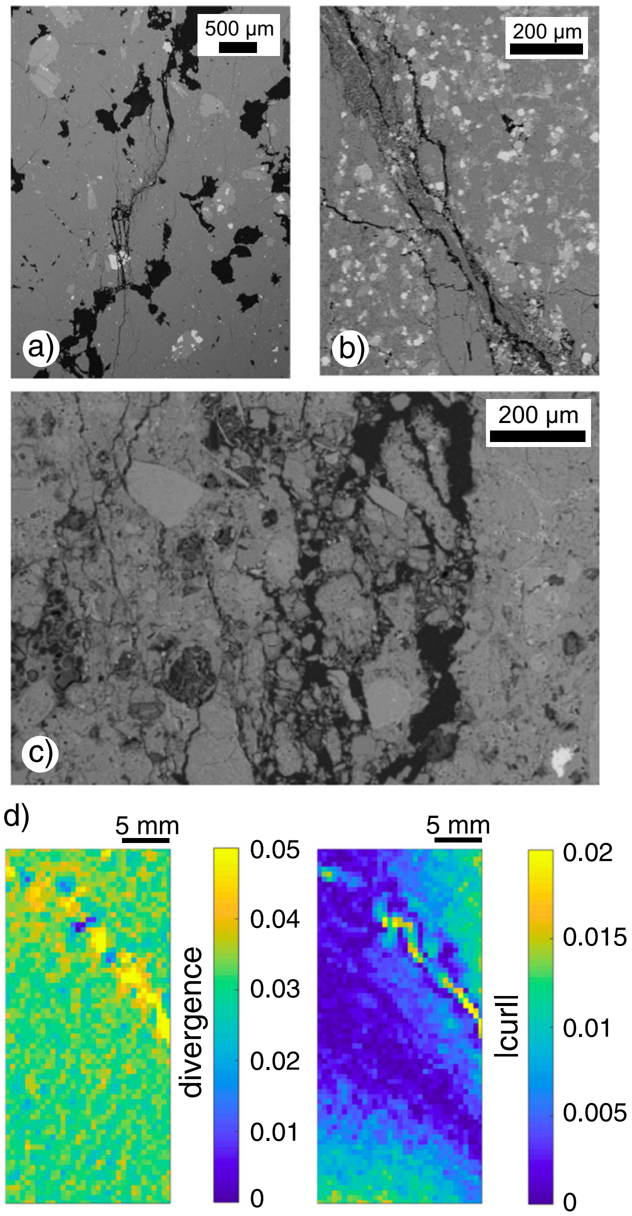

Fig. 20 Brittle microstructures. (**a**) Scanning electron microscope (SEM) image showing a throughgoing shear fracture within a sample of andesite from Volcán de Colima (Mexico) deformed under an effective pressure of 5 MPa (from Heap et al. 2015b). (**b**) SEM image showing a throughgoing shear fracture within a sample of basalt from Mt Etna (Italy) deformed under an effective pressure of 80 MPa (from Zhu et al. 2016). (**c**) SEM image showing a throughgoing shear fracture within a sample of tuff from the Alban Hills (Italy) deformed under an effective pressure of 5 MPa (from Zhu et al. 2011). (**d**) Results of digital volume correlation analysis on a sample of andesite from Volcán de Colima deformed under an effective pressure of 10 MPa (from Heap et al. 2020a). The left and right images show the divergence (volumetric strain) and curl (a proxy for shear strain) of the displacement field, respectively

AE as a function of increasing strain (Fig. 18c) is higher as the effective pressure is increased. The triaxial mechanical data for trachyandesite provided in Fig. 18 are qualitatively similar to triaxial data presented for other trachyandesites (e.g. Loaiza et al. 2012; Zorn et al. 2018) and other volcanic rock types, such as basalt (e.g. Adelinet et al. 2013; Zhu et al. 2016), dacite (e.g. Heap et al. 2016b), andesite (e.g. Heap et al. 2015b; Farquharson et al. 2017), and tuff (e.g. Zhu et al. 2011; Heap et al. 2014c, 2015c) in the ductile regime. Triaxial deformation experiments on basalt deformed in the ductile regime in which P-wave velocities were measured have also showed that P-wave velocity decreased during the elastic phase of the experiment, but then increased following C^* (Adelinet et al. 2013).

Importantly, macroscopic failure in the samples of trachyandesite shown in Fig. 18 (deformed at effective pressures between 80 and 140 MPa) was not manifest as a throughgoing shear fracture (see inset on Fig. 18a). The failure mode of volcanic rocks in the ductile regime can either be distributed (cataclastic grain crushing and/or pore collapse; see pioneering work of Shimada 1986) or localised into compaction bands, as was the case for the trachyandesite from Volvic (see inset in Fig. 18a). Both the formation of compaction bands and cataclastic flow are considered here as ductile behaviour. Cataclastic flow has been observed in samples of porous tuff (Zhu et al. 2011; Heap et al. 2015c) and basalt from Mt. Etna (Zhu et al. 2016; see also Shimada 1986). Failure in these samples deformed in the ductile regime was manifest as the distributed cataclastic collapse of pores (Fig. 21), alongside microcracking in the case of the basalt from Mt. Etna (see Zhu et al. 2016).

Laboratory studies on volcanic rocks have observed compaction bands in porous basalt (Adelinet et al. 2013), porous trachyandesite (Loaiza et al. 2012, this study), porous andesite (Heap et al. 2015b, 2017, 2020a), and porous dacite (Heap et al. 2016b). Compaction bands have therefore been observed in volcanic rocks containing initial porosities of 0.08 (in basalt; Adelinet et al. 2013) to 0.32 (in dacite; Heap et al. 2016b). Compaction bands are planar deformation features characterised by a lower porosity than the surrounding host rock. In detail, the compaction bands formed in these lavas were planes of collapsed pores connected by microcracks that formed sub-perpendicular to the maximum principal stress (examples are shown in Fig. 22). Recently, digital volume correlation analysis performed on X-ray tomographic images of a sample of andesite from Volcán de Colima (before and after deformation under an effective pressure of 50 MPa) highlighted that strain localised into ~1 mm-thick, undulating compaction bands orientated sub-perpendicular to the maximum principal stress with little evidence of shear (Fig. 22c; Heap et al. 2020a). These authors concluded that these compaction bands likely formed following stress drops seen in the mechanical data and formed within the zones of highest porosity, within the large, well-connected porosity backbone of the sample (Heap et al. 2020a). It has been shown previously that the stress drops associated with compaction band growth correspond to upticks in AE activity (e.g. Adelinet et al. 2013; Heap et al. 2015b). Finally, Heap et al. (2020a)

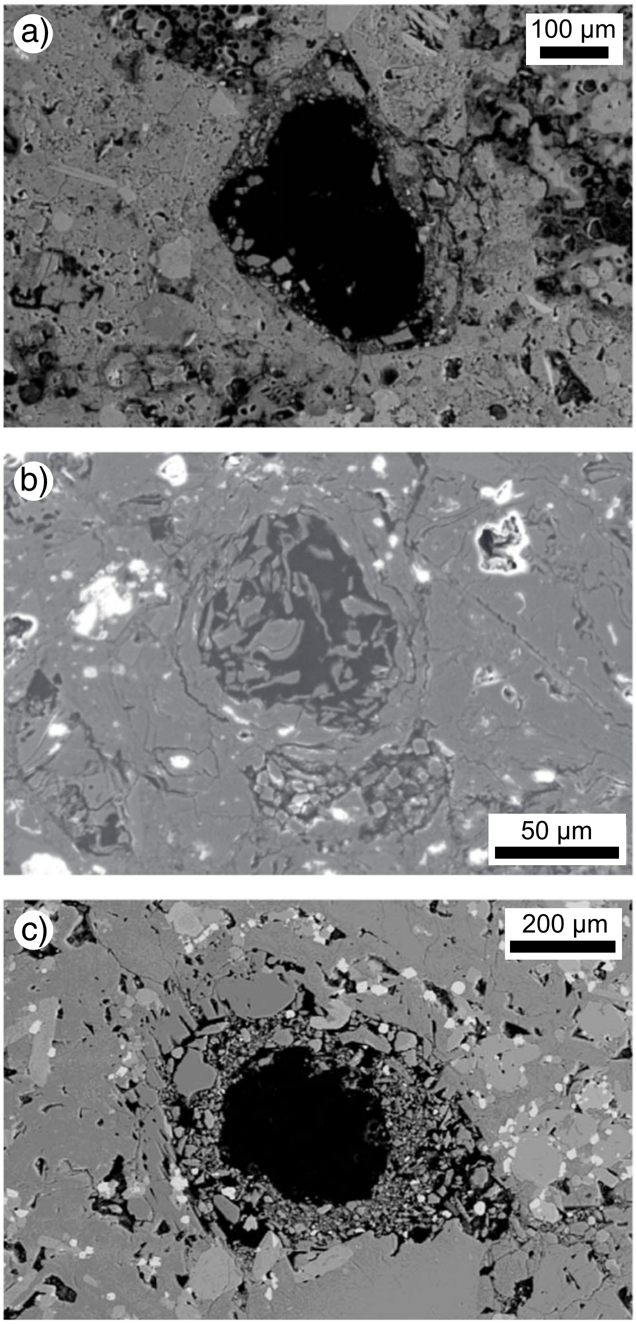

Fig. 21 (**a**) Scanning electron microscope (SEM) image of a collapsed pores within a sample of tuff from Alban Hills (Italy) under an effective pressure of 30 MPa (from Zhu et al. 2011). (**b**) SEM image of a collapsed pores within a sample of tuff from Whakaari volcano (New Zealand) under an effective pressure of 30 MPa (from Heap et al. 2015b). (**c**) SEM image of a collapsed pore within a sample of basalt from Mt Etna (Italy) deformed under an effective pressure of 150 MPa (from Zhu et al. 2016)

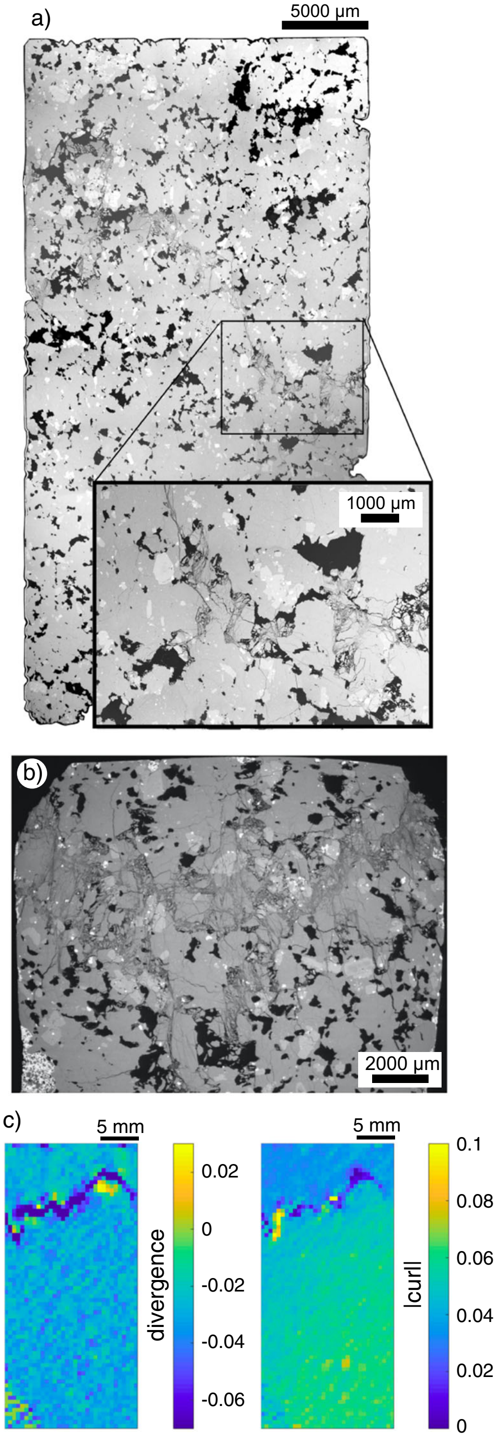

Fig. 22 (**a**) Scanning electron microscope (SEM) map of a sample of andesite from Volcán de Colima (Mexico) deformed under an effective pressure of 50 MPa showing a compaction band (from Heap et al. 2015b). (**b**) SEM image of a sample of andesite from Volcán de Colima deformed under an effective pressure of 30 MPa and a temperature of 400 °C showing a compaction band (from Heap et al. 2017). (**c**) Results of digital volume correlation analysis on a sample of andesite from Volcán de Colima deformed under an effective pressure of 50 MPa (from Heap et al. 2020a). The left and right images show the divergence (volumetric strain) and curl (a proxy for shear strain) of the displacement field, respectively

concluded that, because compaction bands in lavas form as a result of cataclastic pore collapse, it is likely that the thickness of compaction bands in lavas will be close to the pore diameter and that the tortuosity of the band will be governed by the shape of the porosity network. Because porous volcanic materials are often characterised by a complex porosity structure, compaction bands in porous volcanic rocks are very likely to present tortuous geometries, as shown in Fig. 22. Experimental studies have shown that compaction bands can reduce the permeability of volcanic rock by up to one or two orders of magnitude (Heap et al. 2014a; Farquharson et al. 2017; Heap et al. 2020a). Farquharson et al. (2017), for example, showed that the permeability of a porous andesite from Volcán de Colima deformed under effective pressures of 10–70 MPa tends to increase at low strains (< 0.05) and then decrease at higher strains (0.06–0.24). These authors found that permeability can decrease relative to its original value by as much as two orders of magnitude (Farquharson et al. 2017).

Of great interest, because their ability to reduce the permeability of volcanic rocks by up to one or two orders of magnitude (Heap et al. 2014a; Farquharson et al. 2017; Heap et al. 2020a), is why some volcanic rocks develop compaction bands and others do not. The formation of compaction bands in sandstones, for example, requires a relatively homogeneous grain size distribution (e.g. Wang et al. 2008; Cheung et al. 2012). This observation may explain why granular tuffs do not form compaction bands: they typically have a very wide grain size distribution. However, the lavas that been observed to develop compaction bands in the laboratory have a very wide pore size distribution, as can be seen in Fig. 22. Therefore, homogeneity, or at least pore size/shape homogeneity, is not a pre-requisite for compaction band formation in porous lavas. Data and microstructural observations from Heap et al. (2017) suggest that, for samples that develop compaction bands, compaction localisation can be expected at temperatures up to the threshold glass transition. Above the threshold glass transition, these authors showed that porosity loss is distributed throughout the sample (Heap et al. 2017). With the available data, it is not yet clear as to why some volcanic rocks develop compaction bands and others do not, offering an exciting avenue for future research. In contrast to experimental observations, in which compaction bands are observed in lavas but not in tuffs, localised compactional features, to the authors' knowledge, have, so far, only been observed in tuff (e.g. Wilson et al. 2003; Okubo 2014; Cavailhes and Rotevatn 2018) and hyaloclastite (e.g. Gudmundsson 2017) outcrops in the field.

Finally, we highlight that, if a sample is compacted far beyond C^{*}, the sample can undergo a switch from shear-enhanced compaction to dilatational microcracking. This transition is termed $C^{*\prime}$ and marks the limit of inelastic porosity reduction. C^{*}' has been observed in porous sandstones (e.g. Baud et al. 2006) and porous limestones (e.g. Baud et al. 2000b). However, to our knowledge, this phenomenon has only been observed twice in volcanic rock (Heap et al. 2015b; Farquharson et al. 2017). Heap et al. (2015b) showed that C^{*}' occurred in a porous andesite (porosity = 0.155) from Volcán de Colima deformed at an effective pressure of 50 MPa at an axial strain of about 0.13, following a porosity loss of about 0.036. These experiments show that inelastic compaction in volcanic rock will not simply continue until the sample porosity is zero.

Failure envelopes for volcanic rocks One of the most convenient ways in which to compare the mechanical behaviour of a rock is by comparing their brittle failure envelopes and compactive yield caps on plots of differential stress at failure as a function of the effective mean stress, P ("$P-Q$ plots"). In the brittle regime, it is the peak differential stress, Q, that maps out the brittle failure envelope. In the ductile regime, the onset of inelastic compaction, C^{*}, delineates the compactive yield cap. The onset of inelastic compaction under hydrostatic conditions, P^{*}, plots along the x-axis (where Q = 0 MPa) and forms the last point in the yield cap. If the state of stress plots inside the failure envelope/compactive yield cap, the rock is "pre-failure". The rock has failed (or "yielded") if the state of stress plots outside the failure envelope/compactive yield cap (by a shear fracture on the left-hand-side and by inelastic compaction on the right-hand-side). The "top" of the cap therefore represents the stress conditions required for the switch from brittle to ductile behaviour.

We provide in Fig. 23a critical stress data for a range of different volcanic rocks with different porosities and microstructural attributes: trachyandesite from the Açores (Loaiza et al. 2012), two andesites from Volcán de Colima (porosity 0.17 and 0.24; Heap et al. 2015b), dacite from Mt St Helens (porosity 0.32; Heap et al. 2016b), and tuffs from Whakaari volcano (porosity 0.29; Heap et al. 2015c) and Alban Hills (porosity 0.32; Zhu et al. 2011). Because no data exist for porous rhyolite, we supplement these data with new data for rhyolite from Tarawera (porosity 0.39; Taupō Volcanic Zone, New Zealand; data unique to this study; Table 6), data which also act as a high porosity end-member. The dataset is also supplemented by new data for trachyandesite from Volvic (porosity 0.21; data unique to this review; Table 5). The brittle failure envelope and compactive yield caps for volcanic rocks are qualitatively similar to those for porous sedimentary rocks: peak stress increases as a function of increasing effective pressure in the brittle regime, and the stress required for C^{*} decreases as a function of increasing effective pressure in the ductile regime (Fig. 23a).

Data of this nature for sandstone and limestone highlight that, although porosity exerts an importance influence on the stress conditions required for the brittle-ductile transition and shear-enhanced compaction, other microstructural parameters such as grain size also play a role (e.g. Wong and Baud 2012; see also Carbillet et al. 2021). Porosity also exerts an important control on these critical stresses for volcanic rocks: the switch from brittle to ductile behaviour and the compactive yield cap are, in general, at higher stress values for rocks with a lower porosity (Fig. 23a). It is interesting to note, for example, that the dacite from Mt St Helens and the tuff from Alban Hills, rocks with identical average porosities (porosity 0.32), have similar compactive yield caps despite their significant microstructural differences (e.g. lava versus granular pyroclastic rock). However, although the compactive yield cap for the rock with the highest porosity (rhyolite from Tarawera; porosity 0.39) is at the lowest stresses, the least porous rock (andesite C8 from Volcán de Colima; porosity 0.17) is not at the highest stress values (Fig. 23a). The yield caps for the tuff from Whakaari volcano (porosity 0.29), the other andesite from Volcán de Colima (porosity 0.24), the trachyandesite from the Açores (porosity 0.18), and the trachyandesite from Volvic (porosity 0.21) are all at higher stresses (Fig. 23a). Due to their varied microstructures, forwarding a definitive reason or reasons why these samples have yield caps at higher stresses than andesite C8 from Volcán de Colima is not straightforward, although the pore sizes or pore size range of these materials may offer some explanation. For example, the average pore diameters of the tuff from Whakaari volcano (100 μm; Heap et al. 2015c) and andesite LAH4 from Volcán de Colima (200 μm; Heap et al. 2015b) are lower than that of andesite C8 (250 μm; Heap et al. 2015b), and could explain the high stresses of their compactive yield caps despite their higher porosities. Yield caps for samples with greatly different pore sizes or pore shapes, but similar porosities and other microstructural attributes, are now required to better understand the influence of pore size and shape on the switch from brittle to ductile behaviour and the compactive yield cap of volcanic rocks.

The failure envelopes for sandstones and limestones are often elliptical in $P-Q$ stress space, described by (Wong et al. 1997; Wong and Baud 2012):

$$\frac{\left(P/P^{*}-\gamma\right)^{2}}{(1-\gamma)^{2}}+\frac{\left(Q/P^{*}\right)^{2}}{(\delta)^{2}}=1 \tag{9}$$

where for sandstones and limestones, γ = 0.5 and δ varies between 0.5 and 0.7. To better understand the shape of the yield caps for volcanic rocks, we normalise the data to P^{*} (Fig. 23b). If the yield caps are elliptical, as is typical for porous sedimentary rocks, the data should plot within the curves for δ = 0.5 and δ = 0.7 (Eq. (9)). Figure 23b shows that the data for the granular rocks, the tuffs from Whakaari volcano and Alban Hills, plot within these curves, indicating that their yield caps are elliptical. The lavas (andesite and dacite),

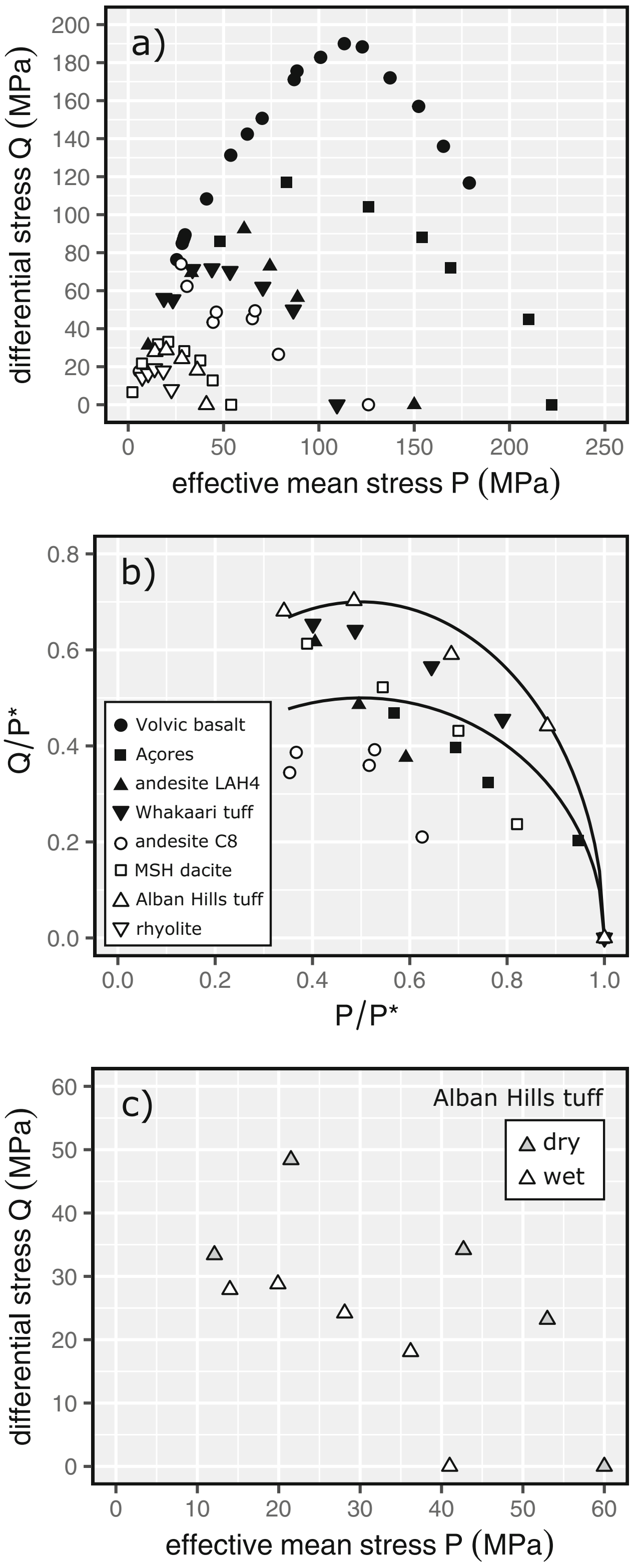

Fig. 23 (**a**) Differential stress as a function of effective mean pressure ("$P-Q$" plot) showing brittle failure envelopes and compactive yield caps for volcanic rocks. (**b**) Differential stress as a function of effective mean pressure, both normalised to P_*. The two curves represent idealised elliptical yield caps (Eq. (9)), assuming $\gamma = 0.5$ and $\delta = 0.5$ and $\delta = 0.7$ (see text for details). (**c**) Differential stress as a function of effective mean pressure showing compactive yield caps for dry and wet tuff from Alban Hills (Italy; data from Zhu et al. 2011)

however, have linear yield caps. Linear yield caps have been previously observed for Bleurswiller sandstone, a porous sandstone that contains porosity clusters (Baud et al. 2015). Baud et al. (2015) suggested that the linear yield caps were the result of the collapse of these pre-existing porosity clusters (volumes of higher porosity than the bulk sample porosity). The linear yield caps for andesite from Volcán de Colima (Heap et al. 2015b) and dacite from Mt St Helens (Heap et al. 2016b) were interpreted by these authors as the result of a high pre-existing microcrack density. Heap et al. (2015b) argued that, for the same increase in effective pressure, the decrease in the differential stress required for C^* will be less for a rock containing microcracks than for an initially microcrack-free rock. This is because the increase in effective pressure will also close pre-existing microcracks and therefore strengthen the rock, resulting in a linear yield cap. Although this hypothesis remains to be tested, we note that the tuffs from Whakaari volcano and Alban Hills, rocks that contain few pre-existing microcracks compared to the lavas, and have elliptical yield caps. However, it is also possible that, similar to Bleurswiller sandstone (Baud et al. 2015), that the linear yield caps for these lavas is a result of a heterogenous distribution of porosity. It is difficult to forward a definitive reason for the linear shape of the yield caps of the tested lavas and more data are now required to explore the aforementioned hypotheses.

Porosity and microstructural parameters such as pore size and shape are not the only factors that can influence the mechanical behaviour of volcanic rocks under triaxial conditions: alteration and environmental factors such as the presence of water, temperature, and strain rate can also play a role. For example, triaxial experiments have showed that andesites from Mt Ruapehu characterised by intermediate and advanced argillic alteration were brittle and ductile, respectively, under the same effective pressure (Fig. 24a and b; Mordensky et al. 2019). The experiments of Mordensky et al. (2019) highlight that the failure mode (brittle or ductile) can be modified by alteration alone: highly altered rocks deformed in a ductile manner at an effective pressure of 10 MPa, and moderately altered rocks deformed in a brittle manner (Fig. 24a and b; Mordensky et al. 2019). Deformation experiments performed by Siratovich et al. (2016) also highlight that alteration can greatly influence the mechanical behaviour of andesite under triaxial conditions. Recently, Nicolas et al. (2020) deformed samples of andesite that had been altered in the laboratory for 1 month at a confining pressure of 20 MPa and temperatures of 80, 180, and 280 °C. These authors found that alteration decreased the strength of andesite under triaxial conditions and concluded that microcrack-filling smectite alteration reduced the coefficient of friction and therefore the strength of the studied andesite (Nicolas et al. 2020).

As for uniaxial compressive strength (Fig. 8), the presence of water can also influence the mechanical behaviour of

Table 6 Summary of the triaxial experimental data for Tarawera rhyolite (New Zealand; data unique to this study). The peak differential stress maps out the brittle failure envelope and C^* (the onset of shear-enhanced compaction) maps of the compactive yield cap

Connected porosity	Confining pressure (MPa)	Pore fluid pressure (MPa)	Effective pressure (MPa)	Effective mean stress, *P* (MPa)	Peak differential stress (MPa)	Differential stress at C* (MPa)
0.37	12.5	10	2.5	7.3	14.5	-
0.37	15	10	5	10.5	16.4	-
0.39	17.5	10	7.5	13.8	19.0	-
0.40	22.5	10	12.5	18.4	-	17.8
0.39	30	10	20	13.8	-	8.0

volcanic rocks deformed under triaxial conditions. For example, Fig. 23c shows yield caps for dry and wet tuff from Alban Hills (data from Zhu et al. 2011). The yield cap for the samples deformed dry are at higher stresses than those deformed wet (Fig. 23c). Reasons for the reduction in C^* and P^* in the presence of water include a reduction in fracture toughness, the presence of calcite, a reduction in friction, and the presence of zeolites and clays (Zhu et al. 2011). Based on uniaxial compressive strength data (Fig. 8), it is likely that weakening in the ductile field is more pronounced in tuffs than in lavas. An aqueous pore fluid phase can also influence the mechanical behaviour of rock by promoting time-dependent stress corrosion reactions (Brantut et al. 2013). Experiments designed to study this mechanism, termed brittle creep experiments, have been performed on tuff (e.g. Martin et al. 1997; Ma and Daemen 2006; Ye et al. 2015) and basalt (Heap et al. 2011). Time-dependent brittle creep experiments have shown that rock can fail under a constant stress below its short-term failure stress (the maximum differential stress the rock can withstand during a constant strain rate experiment). Experiments on basalt from Mt Etna show that the rate of deformation during brittle creep is highly dependent on the applied differential stress and the effective pressure (Heap et al. 2011). More experiments (constant strain rate and creep experiments) are now necessary to understand the influence of water on the strength of volcanic rocks under triaxial conditions.

Below the threshold glass transition, temperature can also influence the mechanical behaviour of volcanic rock under triaxial conditions. Figure 23c and d shows triaxial data for low-porosity basalt deformed under an effective pressure of 100 MPa and temperatures from 600 to 950 °C (data from Violay et al. 2015a). Unlike the uniaxial compressive strength tests performed under high in-situ temperatures, which showed that strength increased as a function of increasing temperature (Fig. 10d), the data shown in Fig. 24c show that temperature decreases compressive strength under triaxial conditions (see also Bakker et al. 2019). Strength decreased from ~900 to ~260 MPa, and the porosity reduction as a function of axial strain decreased as temperature increased from 600 to 950 °C (Fig. 23c and d). These authors interpreted the observed weakening as the result of the increasing contribution of plastic deformation mechanisms, alongside microcracking (Violay et al. 2012, 2015a). Such plastic deformation mechanisms are not operative in the absence of a confining pressure, explaining the discrepancy between the influence of temperature on the compressive strength of volcanic rock under uniaxial and triaxial conditions. The mechanical data shown in Fig. 24c are qualitatively similar to data presented for dacite from Mt St Helens in Smith et al. (2011), and we note that ductile behaviour was observed in basalt deformed at very high confining pressures (1000 MPa) and high temperatures (675 to 875 °C) (Hacker and Christie 1991). Although high-temperature experiments have been performed on porous andesite from Volcán de Colima (Heap et al. 2017) in the ductile regime, selecting accurate values for C^* was unfortunately not possible for these data. Finally, we note that Li et al. (2019) found that the strength of andesite from Guadeloupe under triaxial conditions (confining pressure = 15 and 30 MPa) increased following exposure to 930 °C for 2 h. For example, compressive strength at a confining pressure of 30 MPa increased from ~340 (no thermal stressing) to ~500 MPa (thermally stressed to 930 °C) (Li et al. 2019). These authors attributed this increase in strength to the healing of microcracks at high temperature (Li et al. 2019).

The vast majority of triaxial deformation experiments performed on volcanic rocks were performed at strain rates ~10^{-5} s^{-1}. Increasing and decreasing the strain rate at pressures and temperatures that do not activate plastic deformation mechanisms will likely increase and decrease strength due to the decrease and increase in the time available for stress corrosion cracking, respectively (e.g. Brantut et al. 2013). Under these pressure and temperature conditions, it is perhaps unlikely that a reduction in strain rate would prompt a change from brittle to ductile behaviour. For example, low-porosity basalt was still brittle when deforming at a strain rate of ~10^{-9} s^{-1} under a constant stress at room temperature (Heap et al. 2011). At higher pressures and temperatures (but still below the threshold glass transition), reductions in strain rate can not only dramatically influence rock strength and mechanical behaviour, but can also promote ductility (e.g. Rocchi et al. 2003; Violay et al. 2012).

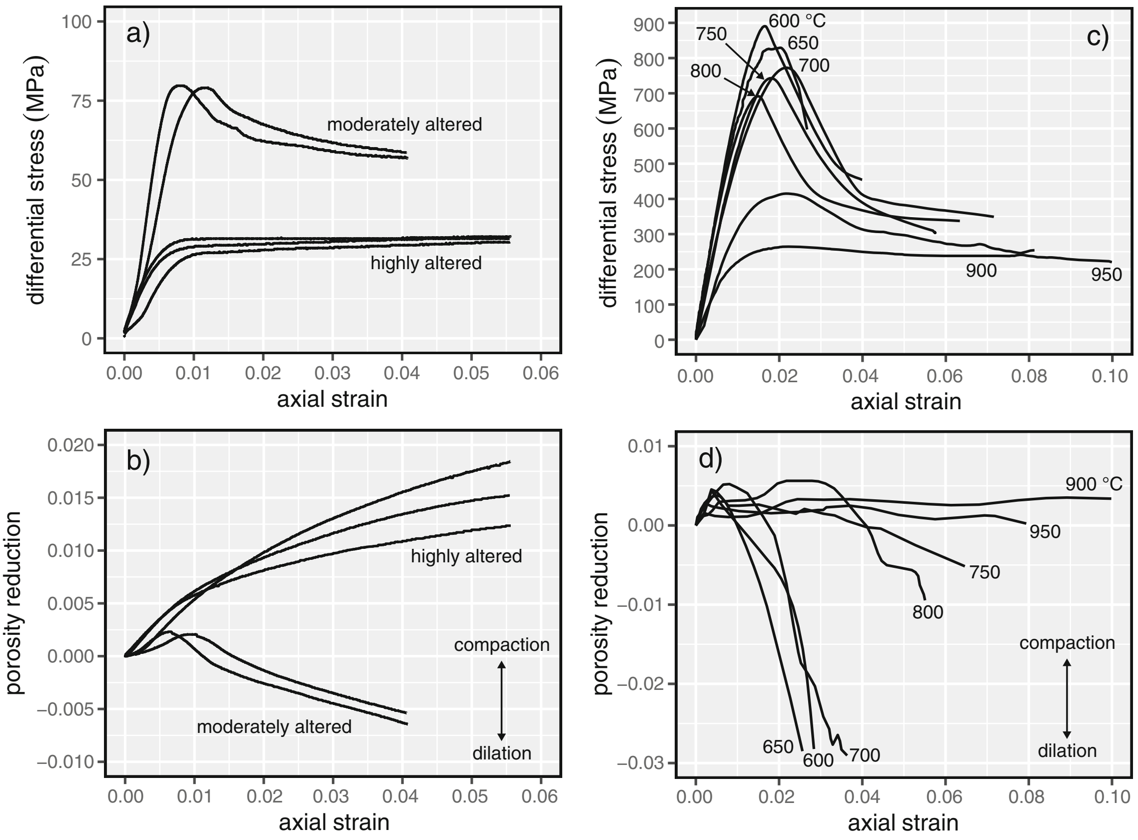

Fig. 24 Stress-strain curves (**a**) and porosity change as a function of axial strain (**b**) for samples of andesite from Mt Ruapehu deformed under an effective pressure of 10 MPa (from Mordensky et al. 2019). Plotted are two curves for moderately altered andesite and three curves for highly altered andesite. Stress-strain curves (**c**) and porosity change as a function of axial strain (**d**) for samples of basalt deformed under an effective pressure of 100 MPa at different temperatures (from Violay et al. 2015a). The number next to each curve indicates the experimental temperature

A better understanding the influence of the presence of water, temperature, and strain rate on the mechanical behaviour of volcanic rocks under triaxial conditions requires new systematic experimental studies.

The tensile strength of volcanic rocks

The tensile strength of volcanic rocks is an important parameter in, for example, eruption forecasting (e.g. Gudmundsson 2011; Browning et al. 2015; Zhan and Gregg 2019; Gudmundsson 2020) and volcano deformation models (Holohan et al. 2017). There are a number of methods to measure the tensile strength of materials in the laboratory (Perras and Diederichs 2014). The most common method employed in studies on volcanic rocks is the Brazilian disc method (loading a cylindrical sample diametrically in compression), which provides the indirect tensile strength. We summarise the tensile strength of volcanic rocks as a function of porosity in Fig. 25. All these data are provided in a Microsoft Excel© spreadsheet that accompanies this contribution as Supplementary Material. The data of Fig. 25 show that, similar to uniaxial compressive strength (Fig. 5), the tensile strength of volcanic rocks decreases nonlinearly as a function of increasing porosity, and that there is considerable scatter in the data. Tensile strength decreases from ~27 MPa at a porosity of ~0 to ~0.5 MPa at porosities above 0.3 (Fig. 25). The tensile strength of volcanic rocks (Fig. 25) is about 1/10 of their compressive strength (Fig. 6), in accordance with data for other rock types (e.g. Paterson and Wong 2005; Hoek and Brown 2019). We also note that the range in tensile strength for a given porosity is reduced as porosity increases (Fig. 25). For example, tensile strength at a porosity of 0.04 varies from ~2 to ~18 MPa and only varies by a couple of MPa at porosities greater than 0.3 (Fig. 25). As for the uniaxial compressive strength of volcanic rocks (Fig. 6) and Young's modulus (Fig. 13), there appears to be no dependence of rock type on the tensile strength of volcanic rocks (Fig. 25). The scatter in the data shown in Fig. 25, as discussed above for the uniaxial compressive strength of volcanic rocks, is likely due to microstructural differences (e.g. pore size and shape) and differences in alteration and/or weathering. Experiments have also shown that the tensile strength of volcanic rocks is reduced in the presence of water (e.g. Wedekind et al. 2013; Hashiba and

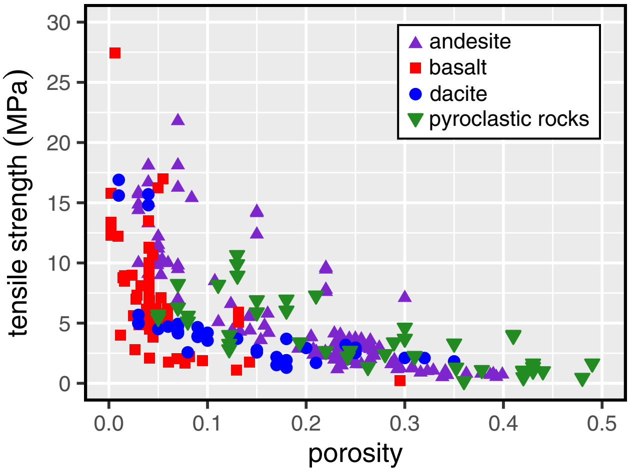

Fig. 25 Tensile strength as a function of porosity for volcanic rocks (n = 277; these data are provided in a Microsoft Excel© spreadsheet that accompanies this contribution as Supplementary Material). Data from: Tuğrul and Gürpinar (1997), Gupta and Rao (2000), Chen et al. (2004), Ersoy and Atici (2007), Kılıç and Teymen (2008), Nara et al. (2010b), Kahraman and Yeken (2010), Graue et al. (2011), Lavallée et al. (2012a), Heap et al. (2012), Wedekind et al. (2013), Karakuş and Akatay (2013), Hashiba and Fukui (2015), Siratovich et al. (2015), Fener and Ince (2015), Ündül and Er (2017), Yavuz et al. (2017), Lamb et al. (2017), Malik et al. (2017), Aldeeky and Al Hattamleh (2018), Zorn et al. (2018), Hornby et al. (2019), Harnett et al. (2019), Moon and Yang (2020), Yasar and Komurlu (2020), Kendrick et al. (2021)

Fukui 2015), although more data are now required to confirm these results. We highlight that the tensile strength reported in Fig. 25 (and in the accompanying Microsoft Excel© spreadsheet) are relevant for the sample lengthscale (several tens of centimetres) and, depending on their intended use, may require upscaling. For example, using the Hoek-Brown failure criterion (Hoek and Brown 2019) and the Rock Mass Rating (RMR; a unitless parameter that classifies the quality of a rock-mass; Bieniawski 1989), Schultz (1995) estimated the upscaled tensile strength of basalt with an average laboratory-measured tensile strength of about 15 MPa to be between 0.1 and 2.5 MPa.

Frictional properties of volcanic rocks

Reliable estimates of the frictional properties of volcanic materials are required to model, for example, volcanic flank collapse (e.g. Hürlimann et al. 2000; Sosio et al. 2012; Peruzzetto et al. 2019). Since debris avalanches can be characterised by very high flow velocities, frictional properties must be investigated over a wide range of slip velocity, from mm/s to m/s. In the last decades, rock friction properties have been investigated using triaxial apparatuses using a saw-cut configuration (e.g. Jaeger 1959; Byerlee 1967; Handin 1969) and under biaxial conditions using a double-direct shear configuration (e.g. Dieterich 1972; Mair et al. 2002; Collettini et al. 2014). Slip velocities and total displacements using these configurations are low (typically μm/s) and short (typically a few mm), respectively. A rotary shear apparatus, however, can achieve slip velocities and total displacements more typical of volcanic environments (e.g. Shimamoto 1994).

In Fig. 26a, we summarise 164 friction experiments performed on cohesive and non-cohesive volcanic rocks (andesite, basalt, dacite, and volcanic ash). All these data are provided in a Microsoft Excel© spreadsheet that accompanies this contribution as Supplementary Material. The steady state friction coefficient is ~0.4–0.8 at low velocity (<< 1 m/s) (Fig. 26a), in agreement with Byerlee's rule (Byerlee 1978). The friction coefficient decreases in all rock types at slip velocities greater than 0.1 m/s (Fig. 26a). The reduction in friction coefficient at high slip velocities is the result of mechanical and/or thermally activated weakening mechanisms. For example, a significant reduction in friction coefficient was observed in basalt (e.g. Violay et al. 2014), andesite (e.g. Lavallée et al. 2012b; Kendrick et al. 2014), and dacite (e.g. Hornby et al. 2015) as a result of frictional melting.

We show the evolution of the peak and steady state friction coefficient as a function of normal stress in Fig. 26b and c, respectively. The steady-state coefficient in Fig. 26c is reported only for slip velocities higher than 1 m/s and slip distances larger than few centimetres. Figure 26b shows that the peak friction coefficient for volcanic rocks is almost independent of the applied normal stress (e.g. Byerlee 1978). The normal stress, however, has a large effect on the steady state friction coefficient of volcanic materials (cohesive rocks and ash) (Fig. 26c). For example, the data for basalt are well described by a power law of the form $\mu_{ss} = 1.06 \times \sigma_n{}^{-0.77}$, where μ_{ss} is the steady state friction coefficient and σ_n is the normal stress. The power law dependence of the steady state friction coefficient and on the normal stress is typical of melt lubrication (e.g. Persson 2000; Di Toro et al. 2006; Niemeijer et al. 2011). Moreover, we highlight that the amount of displacement needed to reach steady state friction decreases with increasing the normal stress (Violay et al. 2014, 2015b). Interestingly, at a given effective normal stress, the amount of displacement needed to reach steady state friction increases in the presence of water as a result of a delay in the initial weakening mechanism (the flash melting of the asperities) (Violay et al. 2014).

Implications for volcanology

Deformation experiments on volcanic rocks are not only important for providing constraints for large-scale modelling, but have also provided important insight as to the mechanisms influencing the wide array of measurements and observations that have become routine at active volcanoes. We provide here examples of how laboratory experiments have and can be used to improve our understanding of volcanic systems. Some of the salient conclusions, based on the work discussed within

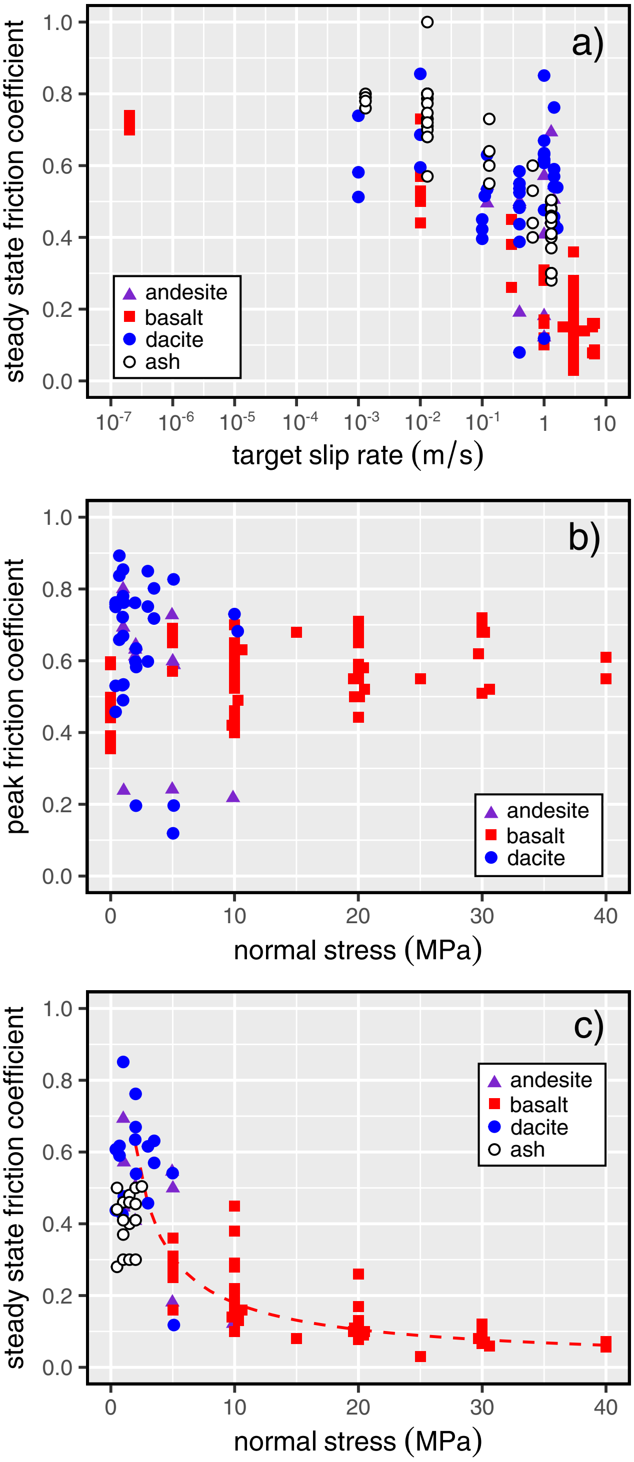

◀ **Fig. 26** (**a**) Steady-state friction coefficient as a function of target slip rate for cohesive (andesite, basalt, and dacite) and non-cohesive (volcanic ash) volcanic materials (*n* = 164; these data are provided in a Microsoft Excel© spreadsheet that accompanies this contribution as Supplementary Material). (**b**) Peak friction coefficient as a function of normal stress for cohesive volcanic rocks (andesite, basalt, and dacite). (**c**) Steady-state friction coefficient as a function of normal stress for cohesive (andesite, basalt, and dacite) and non-cohesive (volcanic ash) volcanic materials. Steady-state friction coefficient is only reported for slip velocities higher than 1 m/s and slip distances larger than a few centimetres. Best-fit power law for the basalt data is shown as a dashed red curve. Data from: Lavallée et al. (2012b), Kendrick et al. (2014), Lavallée et al. (2014), Violay et al. (2014, 2015b), Hornby et al. (2015), Zhang et al. (2017), Giacomel et al. (2018), and Ikari et al. (2020)

this review, are also summarised in the cartoon presented as Fig. 27.

The collapse of the flank or dome of a volcano represents a significant hazard. In the case of the 1980 eruption of Mt St Helens, for example, the collapse of the North face of the volcano not only generated an enormous landslide (of approximately 2 km^3), but also rapidly unloaded the volcanic edifice, resulting in hydrothermal blasts and a Plinian eruption with a 20 km-high column (Lipman and Mullineaux 1982). Flank/dome stability assessments at active volcanoes is therefore an important component of risk analysis. Methods that assess volcano stability using either the GSI (e.g. Apuani et al. 2005; del Potro and Hürlimann 2008; Rodríguez-Losada et al. 2009; Borselli et al. 2011; Schaefer et al. 2013; Dondin et al. 2017) or RMR (e.g. Watters et al. 2000; Okubo 2004) require laboratory-measured values of UCS (provided in the Microsoft Excel© spreadsheet that accompanies this contribution as Supplementary Material). Other methods, such as the columns limit-equilibrium slope stability analysis (e.g. Reid et al. 2000, 2001; Reid 2004; Ball et al. 2018), require the cohesion and the angle of internal friction of the rock, both of which can be determined from suites of triaxial deformation experiments. Models of lava dome growth and collapse also require input parametres for the physical and mechanical properties of volcanic rocks (e.g. Harnett et al. 2018b; Walter et al. 2019). To aid future modelling studies, we provide in Table 7 a compilation of values of cohesion and the internal angle of friction for a range of volcanic rocks (andesite, basalt, dacite, and tuff), calculated from published triaxial data. We note, however, that these values should be upscaled using, for example, the GSI and the generalised Hoek-Brown failure criterion (Hoek and Brown 2019) before they are used in large-scale models. Figure 28 presents cohesion and internal friction angle for volcanic rocks (Table 7) as a function of porosity. These data show that cohesion and internal friction angle both decrease as a function of increasing porosity (Fig. 28). An empirical fit to the cohesion data as a function of porosity (Fig. 28a), for example, would permit estimations for the laboratory-scale cohesion of volcanic rocks for a given porosity. Once slope failure has occurred, the flow velocity and maximum distance obtained by a volcanic debris avalanche can be modelled using the frictional properties of volcanic rocks (e.g. Hürlimann et al. 2000; Sosio et al. 2012; Peruzzetto et al. 2019), data compiled in the Microsoft Excel© spreadsheet that accompanies this contribution as Supplementary Material (see also Fig. 26).

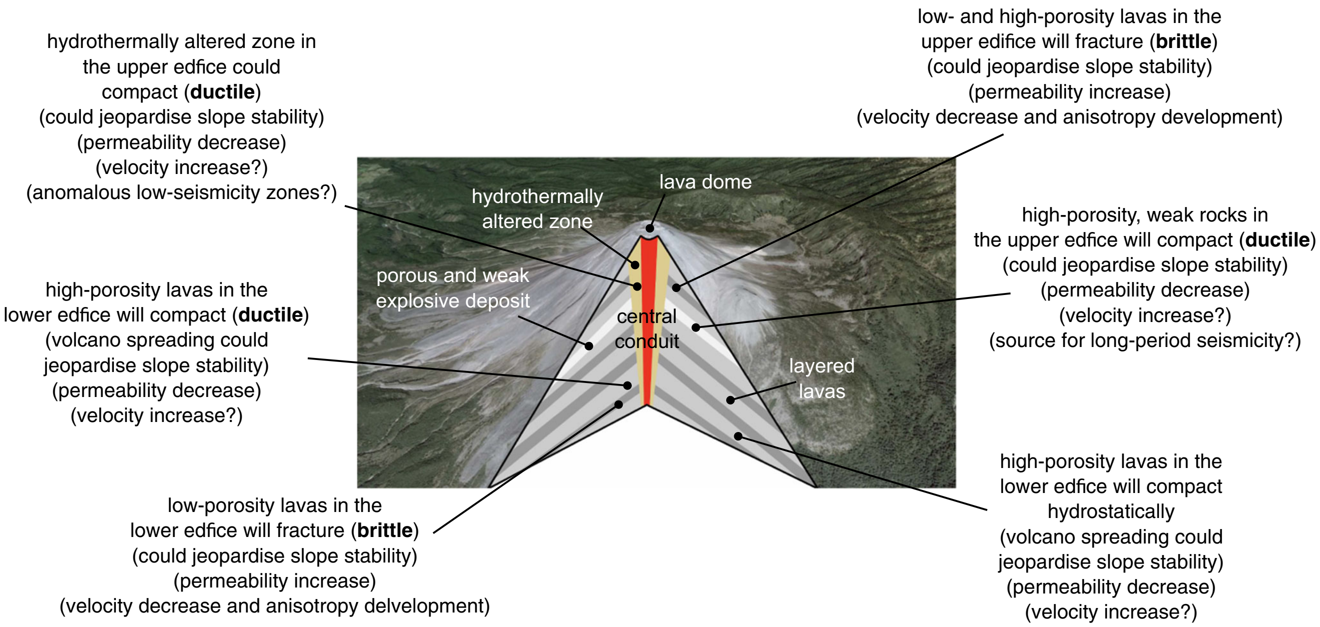

Fig. 27 Cartoon cross-section of a typical stratovolcano highlighting mechanical behaviour and failure modes for volcanic rocks within a volcanic edifice, and the influence of such mechanical behaviour on slope stability, permeability, elastic wave velocities, and seismicity (updated from Heap et al. 2015b)

Laboratory deformation experiments contribute more than just providing values for slope stability modelling, however. A detailed understanding of the factors that promote the ductility of the rocks forming a volcanic edifice, thought to facilitate edifice spreading and destabilisation (e.g. van Wyk de Vries and Francis 1997; van Wyk de Vries and Matela 1998; Borgia et al. 2000; van Wyk de Vries et al. 2001; Cecchi et al. 2004), can also be gleaned through laboratory experiments. For example, triaxial deformation experiments showed that high-porosity tuff from Mt Epomeo (Italy) was ductile at very low effective pressure (i.e. depth), a behaviour thought to facilitate slope instability at Mt Epomeo (Marmoni et al. 2017). A common theme to the discussed models of volcano spreading, instability, and collapse is a weak or ductile layer,

Table 7 Laboratory-scale cohesion and internal angle of friction for a range of volcanic rocks (andesite, basalt, dacite, and tuff), calculated from published triaxial data

Volcano or area	Rock type	Porosity	Cohesion (MPa)	Internal angle of friction (°)	Reference for triaxial data
Volcán de Colima (Mexico)	andesite B5	0.08	26.0	46.2	Heap et al. (2015b)
Volcán de Colima (Mexico)	andesite A5	0.11	30.1	37.3	Heap et al. (2015b)
Rotokawa geothermal field (New Zealand)	andesite	0.10	30.6	34.2	Siratovich et al. (2016)
Ruapehu (New Zealand)	andesite (altered)	0.27	6.5	15.4	Mordensky et al. (2019)
Déhaies (Guadeloupe, France)	andesite	0.02	65.5	36.8	Li et al. (2019)
Mt Etna (Italy)	basalt	0.04	46.5	46.7	Heap et al. (2011)
Mt Etna (Italy)	basalt EB_I	0.05	36.9	50.2	Zhu et al. (2016)
Mt Etna (Italy)	basalt EB_III	0.05	38.9	44.3	Zhu et al. (2016)
Açores (Portugal)	trachyandesite	0.18	28.9	16.6	Loaiza et al. (2012)
Volvic (France)	trachyandesite	0.21	21.8	39.5	this study
Mt St Helens (USA)	dacite MSH2	0.18	27.5	24.6	Heap et al. (2016b)
Mt St Helens (USA)	dacite	0.06	40.4	50.0	Kennedy and Russell (2012)
Mt St Helens (USA)	dacite SH325-1	0.10	28.7	46.3	Smith et al. (2011)
Chaos Crags (USA)	dacite	0.12	23.5	37.1	Ryan et al. (2020)
Whakaari volcano (New Zealand)	dacite (altered)	0.06	24.8	44.1	Heap et al. (2015c)
Whakaari volcano (New Zealand)	tuff	0.30	9.6	37.9	Heap et al. (2015c)

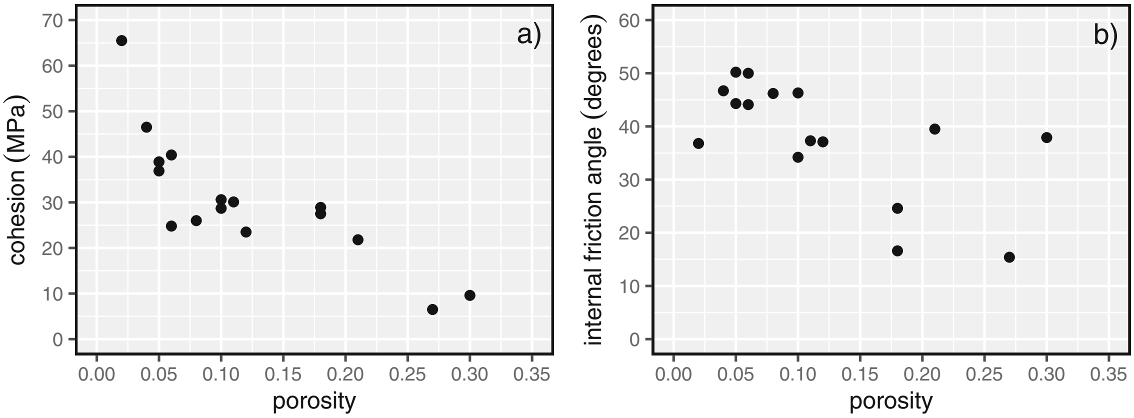

Fig. 28 (**a**) Laboratory-scale cohesion as a function of porosity for a range of volcanic rocks (andesite, basalt, dacite, and tuff). (**b**) Laboratory-scale internal friction angle as a function of porosity for a range of volcanic rocks (andesite, basalt, dacite, and tuff). Values of cohesion and internal angle of friction were calculated from published triaxial data (Table 7)

often the result of hydrothermal alteration. Laboratory studies have shown, for example, hydrothermal alteration can weaken (e.g. Pola et al. 2014; Wyering et al. 2014; Frolova et al. 2014, 2020) and promote ductility (Mordensky et al. 2019) in volcanic rocks (Figs. 7a and 24a). The perceived importance of a weak hydrothermally altered zone on volcano stability highlights the monitoring hydrothermal alteration using geophysical techniques, both spatially and temporally, is an important consideration in hazard assessments at active volcanoes (e.g. Ball et al. 2013, 2015; Rosas-Carbajal et al. 2016; Byrdina et al. 2017; Ahmed et al. 2018; Darmawan et al. 2018; Ghorbani et al. 2018; Kereszturi et al. 2020). Muon tomographic surveys (e.g. Rosas-Carbajal et al. 2017) could also be used identify porous zones that may be susceptible to ductile deformation. Furthermore, when combined with laboratory strength measurements, techniques such as electrical tomography (e.g. Rosas-Carbajal et al. 2016), muon tomography (e.g. Rosas-Carbajal et al. 2017), and hyperspectral imaging (e.g. Kereszturi et al. 2020) could provide strength estimates for a volcanic edifice or dome (e.g. Revil et al. 2020).

The tensile strength of volcanic rocks (Fig. 25; data available in the accompanying Microsoft Excel© spreadsheet) is an important parameter in volcano deformation (Holohan et al. 2017) and eruption forecasting modelling (e.g. Gudmundsson 2011; Browning et al. 2015; Zhan and Gregg 2019; Gudmundsson 2020). For example, robust measurements of tensile strength are required to estimate the magma overpressure required to propagate magma-filled fractures (e.g. Gudmundsson 2006) and estimations of the volume of a magma chamber (e.g. Gudmundsson 1987; Browning et al. 2015). Measurements of fracture toughness (Table 3) can also be used to assess magma overpressures required to propagate magma-filled fractures (e.g. Dahm 2000; Rivalta et al. 2015; Kavanagh et al. 2017), although Rivalta et al. (2015) note that the upscaling of fracture toughness to the field scale remains to be resolved. The material toughness of volcanic rocks, which can be calculated from the fracture toughness, Poisson's ratio, and the Young's modulus, can also be used to model the propagation of fractures and dykes (e.g. Gudmundsson 2009, 2012). We also compiled data for the Young's modulus of volcanic rocks (Fig. 13; data available in the accompanying Microsoft Excel© spreadsheet), useful for models of fracture/fracture propagation and arrest (e.g. Gudmundsson 2002; Geshi et al. 2012; Douma et al. 2019; Forbes Inskip et al. 2020; Gudmundsson 2020) and in ground deformation modelling (Heap et al. 2020b and references therein).

Data from triaxial deformation experiments performed on volcanic rock can help construct strength profiles and provide depths for the brittle-ductile transition for the oceanic crust (e.g. Violay et al. 2012) and volcanic edifices (e.g. Bakker et al. 2019; Parisio et al. 2019). Bakker et al. (2019), for example, use experimental data for two materials chosen to represent the edifice at Mt Etna to derive empirical constitutive equations to describe how pressure, temperature, and strain rate change rock strength. These authors used these equations to construct a strength profile for Mt Etna and concluded that the brittle-ductile transition predicted by their approach is not dissimilar to the maximum depth typically observed for seismicity at Mt Etna (Bakker et al. 2019).

The failure mode of volcanic rocks controls how their physical properties evolve. Triaxial deformation experiments, for example, have shown that brittle deformation not only reduces elastic wave velocities, but also creates an elastic wave velocity anisotropy (e.g. Stanchits et al. 2006; Ougier-Simonin et al. 2011; Fortin et al. 2011; Adelinet et al. 2013; Harnett et al. 2018a). Data for elastic wave velocity evolution during ductile deformation are rare, however. Adelinet et al. (2013) showed that P-wave velocity decreased during the elastic phase of the experiment, but then increased following C^{*}. Seismic tomography and velocity changes at volcanoes has been used to detect for the presence and the movement of fluids and magma (e.g. Husen et al. 2004; Patanè et al. 2006; Koulakov et al. 2013; Brenguier et al. 2014; de Landro et al. 2017). An understanding of how the elastic wave velocities of volcanic rocks change in response to changes in stress during laboratory experiments can therefore assist in the interpretation of seismic tomography and velocity changes at active volcanoes.

The permeability of a volcanic system is considered important in dictating whether a particular eruption is explosive (high-risk) or effusive (lower risk) (e.g. Eichelberger et al. 1986; Mueller et al. 2008; Cassidy et al. 2018; Heap et al. 2019b). Triaxial deformation experiments on volcanic rocks have shown that brittle deformation can increase permeability (e.g. Fortin et al. 2011; Farquharson et al. 2016; Heap et al. 2020a) and ductile deformation can decrease permeability (e.g. Heap et al. 2014a; Farquharson et al. 2017; Heap et al. 2020a). Therefore, highly-stressed low-porosity rocks in the upper and lower edifice will fracture, creating pathways for fluids that serve to lower overpressures and reduce the likelihood of an explosive eruption. Highly-stressed high-porosity rocks will fracture in the upper edifice, tempering explosivity; however, high-porosity rocks will compact in the lower edifice, reducing host-rock permeability and inhibiting the outgassing of the conduit-dwelling magma. An understanding of the processes that result in increases and decreases to permeability, and how to identify when and where these processes are operative at active volcanoes (using, for example, gas emission data; e.g. Edmonds et al. 2003), could lead to a better understanding of explosive-effusive transitioning at active volcanoes. Laboratory experiments have shown, for example, that the mechanical behaviour of volcanic rock (brittle or ductile) is an important consideration when interpreting radon anomalies at volcanoes (e.g. Mollo et al. 2011).

Seismicity is often used a tool to monitor and forecast volcanic eruptions (e.g. McNutt 1996; McNutt and Roman 2015). One of the most widely used models used in eruption forecasting is the Failure Forecasting Method (FFM; Voight 1988, 1989; Kilburn and Voight 1998; Kilburn 2003; Bell et al. 2011a, 2011b; Lavallée et al. 2008). Evaluating or fine-tuning this method, or similar methods (e.g. Vasseur et al. 2015, 2017), can be achieved using laboratory data. For example, if slow or subcritical crack growth is considered as an important pre-cursor for dynamic rupture within a volcanic edifice (e.g. Kilburn 2003; Kilburn and Voight 1998; Kilburn 2012), information can be perhaps gleaned from the accelerations to failure seen in time-dependent brittle creep experiments on volcanic rocks (e.g. Heap et al. 2011). Laboratory experiments can also be used to better understand the physical processes that result in volcano seismicity (e.g. Benson et al. 2008, 2010; Fazio et al. 2017; Clarke et al. 2019; Rowley et al. 2020). Benson et al. (2008) showed, using triaxial experiments on basalt from Mt Etna, that rapid post-failure decompression triggered low-frequency events. These microseismic events were considered similar to, and therefore may explain the origin of, long-period seismicity recorded at active volcanoes (Benson et al. 2008). More recently, experiments have shown that microseismic events during the deformation of weak volcanic rock are also spectrally indistinguishable from long-period and tremor seismicity (Rowley et al. 2020), supporting the hypothesis that long-period seismicity is not necessarily an indicator of the presence or migration of fluids, but instead indicates upper-edifice deformation (Bean et al. 2014). Finally, Mordensky et al. (2019) concluded, based on triaxial experiments on altered andesites from Mt Ruapehu, that advanced argillic alteration could create an anomalous shallow ductile zone that could influence the expression of pre-eruptive seismicity.

Concluding remarks and future work

The mechanical behaviour and failure modes of volcanic rock are qualitatively similar to sedimentary rocks (Wong and Baud 2012): low-porosity volcanic rocks develop shear fractures (examples shown in Fig. 20) at low- and high-pressure, and high-porosity volcanic rocks develop shear fractures (examples shown in Fig. 20) at low-pressure and deform by cataclastic flow accompanied by shear-enhanced compaction at high-pressure. Compaction localisation in the form of compaction bands can also develop in porous volcanic rocks (examples shown in Fig. 22), as seen in porous sedimentary rocks (e.g. Baud et al. 2004). However, although these behaviours are qualitatively similar, the mechanical behaviour and failure modes of volcanic rock are complicated by their varied and complex microstructure (as emphasised in Fig. 1). Indeed, volcanic rocks are much more complex than sedimentary rocks: their porosity can vary from almost 0 to almost 1, they often contain both microcracks and pores, their pore shapes are more complex and their pore size distributions are much wider than most sedimentary rocks, they can contain crystals characterised by different shapes, sizes, and size distributions, they can be granular or characterised by a groundmass that hosts pores and crystals, their compositions and glass contents can vary, and they are often variably affected by hydrothermal alteration.

Understanding how these attributes, and others, influence the mechanical behaviour and failure modes of volcanic rock is not yet well understood. For example, it is unclear as to why compaction bands, features that can greatly reduce the permeability of volcanic rocks (e.g. Heap et al. 2014a; Farquharson et al. 2017; Heap et al. 2020a), form in some volcanic rocks but not others (discussed in Heap et al. 2020a). Hydrothermal alteration, ubiquitous to many volcanoes, can increase or decrease the porosity of volcanic rock, potentially leading to either a decrease or an increase in rock strength, respectively. However, although some experimental studies highlight that hydrothermal alteration reduces rock strength (e.g. Wyering et al. 2014; Frolova et al. 2014; Farquharson et al. 2019), due to dissolution and mineral replacement, certain types of alteration (e.g. the precipitation of strong or cementing minerals) could increase strength (e.g. Heap et al. 2020c) and have not received as much attention in experimental studies. In short, we do not yet fully understand the influence of alteration on the mechanical behaviour of volcanic rocks or the timescales required, despite its perceived importance in dictating volcano stability (e.g. López and Williams 1993; van Wyk de Vries et al. 2000; Reid et al. 2001). Furthermore, where we should expect alteration leading to net dissolution (porosity increase) and net precipitation (porosity decrease) in a volcano, and how this impacts volcano stability, is understudied (Ball et al. 2015).

One of the most important directions for future research is the integration of laboratory data and field-scale geophysical/geochemical data to create tools to rapidly provide robust hazard assessments at active volcanoes. For example, electrical tomography (e.g. Rosas-Carbajal et al. 2016) or hyperspectral imaging (e.g. Kereszturi et al. 2020) data could be fine-tuned to provide volcanic flank/dome strength profiles that can then be quickly integrated into stability models to provide on-site hazard assessments. To achieve such a goal, laboratory data also require upscaling to the rock-mass or volcano-scale, another topic that requires attention. Although studies have used the GSI or RMR to provide estimates for the strength of volcanic rock-masses (e.g. Watters et al. 2000; Okubo 2004; Apuani et al. 2005; del Potro and Hürlimann 2008; Rodríguez-Losada et al. 2009; Borselli et al. 2011; Schaefer et al. 2013), the complexity of volcanic rocks and volcanic rock-masses suggests that more work is required, and especially experiments at the in-situ pressure and temperature conditions, to better adapt these engineering approaches to volcanic systems.

To conclude, although great advancements have been made in our understanding of the mechanical behaviour and failure modes of volcanic rock, and in our understanding of how these data can be used to better understand volcanoes and volcanic hazards, there are many fruitful avenues for future work that build on the insights reviewed herein.

Appendix

We provide here new data to explore the influence of the length to diameter ratio on the uniaxial compressive strength of dry porous trachyandesite (from Volvic, Chaîne des Puys, France). Cylindrical samples were prepared to a diameter of 20 mm and to lengths between 20 and 55 mm (Table 8). These samples were first vacuum-dried at 40 °C and their connected porosities were calculated using their bulk sample volume and the connected volume measured by a helium pycnometer. The samples were then deformed uniaxially constant strain rate of 1.0 × 10^{-5} s^{-1} until macroscopic failure. A lubricating wax was applied to the end-faces of the samples to avoid problems associated with friction between the sample and the pistons during loading. Our data show that, although the uniaxial compressive strength appears largely unaffected by the length to diameter ratio, the mechanical behaviour of the samples with the lowest length to diameter ratios (1.0 and 1.25) is clearly affected (Fig. 29b). The concave up (typically associated with microcrack closure) and concave down (i.e. strain hardening) portions of these stress–strain curves are exaggerated with respect to the other experiments, and the strain at failure is overestimated (Fig. 29a). Although these data are influenced by the lower experimental reproducibility of volcanic rocks compared to rocks such as granite, they do highlight problems associated with using low length to diameter ratios. It is recommended here that experimental studies use samples that have a length to diameter ratio of at least 2 and, importantly, that the dimensions of the samples used are reported in published works.

Table 8 Uniaxial compressive strength of samples of Volvic trachyandesite (France) prepared to different length to diameter ratios. Sample diameter was 20 mm in all cases

Length/diameter ratio	Uniaxial compressive strength (MPa)
1	95.2
1.25	87.1
1.5	98.4
1.75	101.2
2	94.6
2.25	93.6
2.5	96.1
2.75	105.1

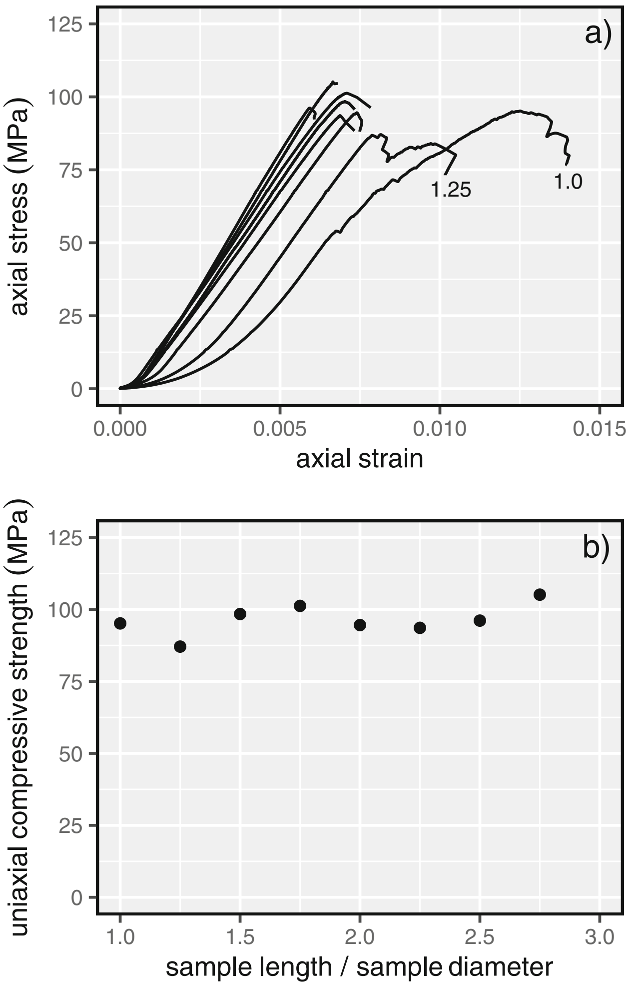

Fig. 29 (**a**) Uniaxial stress–strain curves for samples of trachyandesite from Volvic (France) that have different length to diameter ratios. The number next the two outlying curves indicates the length to diameter ratio. (**b**) Uniaxial compressive strength (UCS) as a function of sample length to sample diameter ratio (the same experiments shown in panel (**a**)). Data in Table 8

Abbreviations UCS, uniaxial compressive strength; LVDT, linear variable differential transducer; AE, acoustic emissions; σ_1, maximum compressive principal stress; σ_2, intermediate compressive principal stress; σ_3, minimum compressive principal stress; P_{eff}, effective pressure; P_c, confining pressure; P_p, pore fluid pressure; C', onset of dilatational microcracking; σ_p, peak uniaxial compressive stress; $2c$, initial crack length in the wing-crack model; γ, crack angle (to the maximum principal stress) in the wing-crack model; r, pore radius in the pore-crack model; l, crack propagation distance in the wing- and pore-crack models; K_{IC}, fracture toughness (critical stress intensity factor); μ, friction coefficient of the sliding crack in the wing-crack model; D_0, initial damage parameter; ϕ, porosity; m and n, constants in the wing-crack analytical solution; a and b, constants in the pore-crack analytical solution; N_A, mean number of microcracks per unit area; E_i, intact Young's modulus (sample scale); E_{rm}, rock-mass Young's modulus; GSI, Geological Strength Index; P^*, onset of hydrostatic inelastic compaction; $\sigma_p{}^*$, uniaxial compressive strength of an effective medium; a^*, the average radius of a micropore in an effective medium; ϕ_*, the porosity of an effective medium; S^*, a factor that captures the cooperative influence of the fracture toughness, micropore radius, and the partitioning of macro- and microporosity; P, effective mean stress; C^*, onset of inelastic compaction; $C^{*\prime}$, onset of dilation following compaction; Q, differential stress; RMR, Rock Mass Rating; μ_{ss}, steady-state friction coefficient; σ_n, normal stress; FFM, failure forecasting method

Supplementary Information The online version contains supplementary material available at https://doi.org/10.1007/s00445-021-01447-2.

Acknowledgements This review would not have been possible without the many discussions the first author has had with Patrick Baud, as well as conversations with many other scientists over the years. Ben Kennedy is thanked for providing the rhyolite from Tarawera. We also thank Thierry Reuschlé, Manon Lincker, and Bertrand Renaudié. Figures were prepared using open source software R Studio, ggplot, and Inkscape. Marie Violay acknowledges support from European Research Council (ERC) grant BEFINE (757290). We thank two reviewers and the associate editor for comments that helped improve this manuscript.

Author's contribution M.J. Heap wrote the first draft of the manuscript and prepared the figures. M.E.S. Violay compiled the frictional property data; all other data were compiled by M.J. Heap. New experimental data were collected by M.J. Heap. Both authors discussed, and agreed upon, the content of the paper.

Funding Open Access funding provided by EPFL Lausanne.

Data availability Data are available in Tables 1–8 and in the Microsoft Excel© spreadsheet that accompanies this contribution as Supplementary Material.

Code availability We used no custom codes in this work.

Declarations

Conflict of interest The authors declare that they have no conflicts of interest.

References

Adam L, Otheim T (2013) Elastic laboratory measurements and modeling of saturated basalts. J Geophys Res Solid Earth 118(3):840–851

Adelinet M, Fortin J, Schubnel A, Guéguen Y (2013) Deformation modes in an Icelandic basalt: from brittle failure to localized deformation bands. J Volcanol Geotherm Res 255:15–25

Ahmed AS, Revil A, Byrdina S, Coperey A, Gailler L, Grobbe N et al (2018) 3D electrical conductivity tomography of volcanoes. J Volcanol Geotherm Res 356:243–263

Aldeeky H, Al Hattamleh O (2018) Prediction of engineering properties of basalt rock in Jordan using ultrasonic pulse velocity test. Geotech Geol Eng 36(6):3511–3525

Al-Harthi AA, Al-Amri RM, Shehata WM (1999) The porosity and engineering properties of vesicular basalt in Saudi Arabia. Eng Geol 54(3-4):313–320

Alm O, Jaktlund LL, Shaoquan K (1985) The influence of microcrack density on the elastic and fracture mechanical properties of Stripa granite. Phys Earth Planet Inter 40(3):161–179

Apuani T, Corazzato C, Cancelli A, Tibaldi A (2005) Physical and mechanical properties of rock masses at Stromboli: a dataset for volcano instability evaluation. Bull Eng Geol Environ 64(4):419

Ashby MF, Sammis CG (1990) The damage mechanics of brittle solids in compression. Pure Appl Geophys 133(3):489–521

Atkinson BK, Avdis V (1980) Fracture mechanics parameters of some rock-forming minerals determined using an indentation technique. Int J Rock Mech Min Sci Geomech Abstr 17(6):383–386

Austria DC, Benson PM (2020) Fracture, fluid and saturation effects on the seismic attributes of rocks from the Southern Negros geothermal field, Philippines. J Volcanol Geotherm Res 107099

Ayday C, Göktan RM (1990) A preliminary engineering geology study directed to the conservation of Midas monument. In: Proc. International Earth Sciences Colloquium on the Aegean Region (IESCA), DE University, Izmir, pp 102–108

Bakker RR, Violay ME, Vinciguerra S, Fazio M, Benson PM (2019) Constitutive laws for Etnean basement and edifice lithologies. J Geophys Res Solid Earth 124(10):10074–10088

Ball JL, Calder ES, Hubbard BE, Bernstein ML (2013) An assessment of hydrothermal alteration in the Santiaguito lava dome complex, Guatemala: implications for dome collapse hazards. Bull Volcanol 75(1):676

Ball JL, Stauffer PH, Calder ES, Valentine GA (2015) The hydrothermal alteration of cooling lava domes. Bull Volcanol 77(12):102

Ball JL, Taron J, Reid ME, Hurwitz S, Finn C, Bedrosian P (2018) Combining multiphase groundwater flow and slope stability models to assess stratovolcano flank collapse in the Cascade Range. J Geophys Res Solid Earth 123(4):2787–2805

Balme MR, Rocchi V, Jones C, Sammonds PR, Meredith PG, Boon S (2004) Fracture toughness measurements on igneous rocks using a high-pressure, high-temperature rock fracture mechanics cell. J Volcanol Geotherm Res 132(2-3):159–172

Baud P, Zhu W, Wong T-f (2000a) Failure mode and weakening effect of water on sandstone. J Geophys Res Solid Earth 105(B7):16371–16389

Baud P, Schubnel A, Wong T-f (2000b) Dilatancy, compaction, and failure mode in Solnhofen limestone. J Geophys Res Solid Earth 105(B8):19289–19303

Baud P, Klein E, Wong TF (2004) Compaction localization in porous sandstones: spatial evolution of damage and acoustic emission activity. J Struct Geol 26(4):603–624

Baud P, Vajdova V, Wong T-f (2006) Shear-enhanced compaction and strain localization: Inelastic deformation and constitutive modeling of four porous sandstones. J Geophys Res Solid Earth 111(B12)

Baud P, Wong TF, Zhu W (2014) Effects of porosity and crack density on the compressive strength of rocks. Int J Rock Mech Min Sci 67:202–211

Baud P, Reuschlé T, Ji Y, Cheung CS, Wong T-f (2015) Mechanical compaction and strain localization in Bleurswiller sandstone. J Geophys Res Solid Earth 120(9):6501–6522

Bean CJ, De Barros L, Lokmer I, Métaxian JP, O'Brien G, Murphy S (2014) Long-period seismicity in the shallow volcanic edifice formed from slow-rupture earthquakes. Nat Geosci 7(1):71–75

Behre CD (1929) Volcanic Tuffs and Sandstones used as building stones in the upper Salmon River Valley, Idaho. Contributions to Economic Geology, pp 811–E

Bell AF, Naylor M, Heap MJ, Main IG (2011a) Forecasting volcanic eruptions and other material failure phenomena: an evaluation of the failure forecast method. Geophys Res Lett 38(15)

Bell AF, Greenhough J, Heap MJ, Main IG (2011b) Challenges for forecasting based on accelerating rates of earthquakes at volcanoes and laboratory analogues. Geophys J Int 185(2):718–723

Benson PM, Thompson BD, Meredith PG, Vinciguerra S, Young RP (2007) Imaging slow failure in triaxially deformed Etna basalt using 3D acoustic-emission location and X-ray computed tomography. Geophys Res Lett 34(3)

Benson PM, Vinciguerra S, Meredith PG, Young RP (2008) Laboratory simulation of volcano seismicity. Science 322(5899):249–252

Benson PM, Vinciguerra S, Meredith PG, Young RP (2010) Spatio-temporal evolution of volcano seismicity: A laboratory study. Earth Planet Sci Lett 297(1-2):315–323

Benson PM, Heap MJ, Lavallee Y, Flaws A, Hess KU, Selvadurai APS et al (2012) Laboratory simulations of tensile fracture development in a volcanic conduit via cyclic magma pressurisation. Earth Planet Sci Lett 349:231–239

Bernard K, van Wyk de Vries B (2017) Volcanic avalanche fault zone with pseudotachylite and gouge in French Massif Central. J Volcanol Geotherm Res 347:112–135

Bieniawski ZT (1989) Engineering rock mass classifications: a complete manual for engineers and geologists in mining, civil, and petroleum engineering. John Wiley & Sons

Blower JD, Keating JP, Mader HM, Phillips JC (2003) The evolution of bubble size distributions in volcanic eruptions. J Volcanol Geotherm Res 120(1-2):1–23

Borgia A, Delaney PT, Denlinger RP (2000) Spreading volcanoes. Annu Rev Earth Planet Sci 28(1):539–570

Borselli L, Capra L, Sarocchi D, De la Cruz-Reyna S (2011) Flank collapse scenarios at Volcán de Colima, Mexico: a relative instability analysis. J Volcanol Geotherm Res 208(1-2):51–65

Brace WF, Paulding BW Jr, Scholz CH (1966) Dilatancy in the fracture of crystalline rocks. J Geophys Res 71(16):3939–3953

Brantut N, Heap MJ, Meredith PG, Baud P (2013) Time-dependent cracking and brittle creep in crustal rocks: A review. J Struct Geol 52:17–43

Brenguier F, Campillo M, Takeda T, Aoki Y, Shapiro NM, Briand X et al (2014) Mapping pressurized volcanic fluids from induced crustal seismic velocity drops. Science 345(6192):80–82

Brodsky EE, Gordeev E, Kanamori H (2003) Landslide basal friction as measured by seismic waves. Geophys Res Lett 30(24)

Browning J, Drymoni K, Gudmundsson A (2015) Forecasting magma-chamber rupture at Santorini volcano, Greece. Sci Rep 5:15785

Broz ME, Cook RF, Whitney DL (2006) Microhardness, toughness, and modulus of Mohs scale minerals. Am Mineral 91(1):135–142

Bubeck A, Walker RJ, Healy D, Dobbs M, Holwell DA (2017) Pore geometry as a control on rock strength. Earth Planet Sci Lett 457:38–48

Butcher E, Gibson A, Benson PM, Koor N, Swift G (2019) Near infrared spectroscopic measurement of strain in rocks. J Near Infrared Spectrosc 27(6):432–440

Byerlee JD (1967) Frictional characteristics of granite under high confining pressure. J Geophys Res 72(14):3639–3648

Byerlee J (1978) Friction of rocks. In: Rock friction and earthquake prediction. Birkhäuser, Basel, pp 615–626

Byrdina S, Friedel S, Vandemeulebrouck J, Budi-Santoso A, Suryanto W, Rizal MH, Winata E (2017) Geophysical image of the hydrothermal system of Merapi volcano. J Volcanol Geotherm Res 329:30–40

Carbillet L, Heap MJ, Baud P, Wadsworth FB, Reuschlé T (2021) Mechanical compaction of crustal analogs made of sintered glass beads: the influence of porosity and grain size. J Geophys Res Solid Earth. https://doi.org/10.1029/2020JB021321

Cant JL, Siratovich PA, Cole JW, Villeneuve MC, Kennedy BM (2018) Matrix permeability of reservoir rocks, Ngatamariki geothermal field, Taupo Volcanic Zone, New Zealand. Geotherm Energy 6(1):2

Cashman KV (2020) Crystal size distribution (CSD) analysis of volcanic samples: advances and challenges. Front Earth Sci 8:291

Cassidy M, Manga M, Cashman K, Bachmann O (2018) Controls on explosive-effusive volcanic eruption styles. Nat Commun 9(1):1–16

Cavailhes T, Rotevatn A (2018) Deformation bands in volcaniclastic rocks–Insights from the Shihtiping tuffs, Coastal Range of Taiwan. J Struct Geol 113:155–175

Cecchi E, van Wyk de Vries B, Lavest JM (2004) Flank spreading and collapse of weak-cored volcanoes. Bull Volcanol 67(1):72–91

Celik MY, Ergül A (2015) The influence of the water saturation on the strength of volcanic tuffs used as building stones. Environ Earth Sci 74(4):3223–3239

Çelik MY, Akbulut H, Ergül A (2014) Water absorption process effect on strength of Ayazini tuff, such as the uniaxial compressive strength (UCS), flexural strength and freeze and thaw effect. Environ Earth Sci 71(9):4247–4259

Chen TC, Yeung MR, Mori N (2004) Effect of water saturation on deterioration of welded tuff due to freeze-thaw action. Cold Reg Sci Technol 38(2-3):127–136

Cheung CS, Baud P, Wong, T.-f. (2012) Effect of grain size distribution on the development of compaction localization in porous sandstone. Geophys Res Lett 39(21)

Clarke J, Adam L, Sarout J, van Wijk K, Kennedy B, Dautriat J (2019) The relation between viscosity and acoustic emissions as a laboratory analogue for volcano seismicity. Geology 47(6):499–503

Coats R, Kendrick JE, Wallace PA, Miwa T, Hornby AJ, Ashworth JD et al (2018) Failure criteria for porous dome rocks and lavas: a study of Mt. Unzen, Japan. Solid Earth 9(6):1299–1328

Cole, P. D., Neri, A., & Baxter, P. J. (2015). Hazards from pyroclastic density currents. In The Encyclopedia of Volcanoes (pp. 943-956). Academic Press.

Collettini C, Di Stefano G, Carpenter B, Scarlato P, Tesei T, Mollo S et al (2014) A novel and versatile apparatus for brittle rock deformation. Int J Rock Mech Min Sci 66:114–123

Colombier M, Wadsworth FB, Gurioli L, Scheu B, Kueppers U, Di Muro A, Dingwell DB (2017) The evolution of pore connectivity in volcanic rocks. Earth Planet Sci Lett 462:99–109

Dahm T (2000) Numerical simulations of the propagation path and the arrest of fluid-filled fractures in the Earth. Geophys J Int 141(3): 623–638

Daoud A, Browning J, Meredith PG, Mitchell TM (2020) Microstructural Controls on Thermal Crack Damage and the Presence of a Temperature-Memory Effect During Cyclic Thermal Stressing of Rocks. Geophys Res Lett 47(19):e2020GL088693

Darmawan H, Walter TR, Troll VR, Budi-Santoso A (2018) Structural weakening of the Merapi dome identified by drone photogrammetry after the 2010 eruption. Nat Hazards Earth Syst Sci (NHESS) 18: 3267–3281

David C, Wong T-f, Zhu W, Zhang J (1994) Laboratory measurement of compaction-induced permeability change in porous rocks: Implications for the generation and maintenance of pore pressure excess in the crust. Pure Appl Geophys 143(1-3):425–456

David EC, Brantut N, Schubnel A, Zimmerman RW (2012) Sliding crack model for nonlinearity and hysteresis in the uniaxial stress–strain curve of rock. Int J Rock Mech Min Sci 52:9–17

de Landro G, Serlenga V, Russo G, Amoroso O, Festa G, Bruno PP et al (2017) 3D ultra-high resolution seismic imaging of shallow Solfatara crater in Campi Flegrei (Italy): New insights on deep hydrothermal fluid circulation processes. Sci Rep 7(1):1–10

del Potro R, Hürlimann M (2008) Geotechnical classification and characterisation of materials for stability analyses of large volcanic slopes. Eng Geol 98(1-2):1–17

del Potro R, Hürlimann M (2009) The decrease in the shear strength of volcanic materials with argillic hydrothermal alteration, insights from the summit region of Teide stratovolcano, Tenerife. Eng Geol 104(1-2):135–143

Di Muro A, Schwarzlmüller F, Kueppers U, Heap MJ, Dingwell DB (2021) Petrophysical characterisation of volcanic ejecta to constrain subsurface lithological heterogeneities: implications for edifice stability at basaltic volcanoes. Volcanica 4(1):41–66

Di Toro G, Hirose T, Nielsen S, Pennacchioni G, Shimamoto T (2006) Natural and experimental evidence of melt lubrication of faults during earthquakes. Science 311(5761):647–649

Dieterich JH (1972) Time-dependent friction in rocks. J Geophys Res 77(20):3690–3697

Dondin FJ, Heap MJ, Robertson REA, Dorville JM, Carey S (2017) Flank instability assessment at Kick-'em-Jenny submarine volcano (Grenada, Lesser Antilles): a multidisciplinary approach using experiments and modeling. Bull Volcanol 79(1):5

Douma LA, Regelink JA, Bertotti G, Boersma QD, Barnhoorn A (2019) The mechanical contrast between layers controls fracture containment in layered rocks. JStruct Geol 127:103856

Duclos R, Paquet J (1991) High-temperature behaviour of basalts—role of temperature and strain rate on compressive strength and KIC toughness of partially glassy basalts at atmospheric pressure. International Journal of Rock Mechanics and Mining Sciences & Geomechanics Abstracts, 28. No. 1:71–76

Edmonds M, Oppenheimer C, Pyle DM, Herd RA, Thompson G (2003) SO2 emissions from Soufrière Hills Volcano and their relationship to conduit permeability, hydrothermal interaction and degassing regime. J Volcanol Geotherm Res 124(1-2):23–43

Eggertsson GH, Lavallée Y, Kendrick JE, Markússon SH (2020) Improving fluid flow in geothermal reservoirs by thermal and mechanical stimulation: The case of Krafla volcano, Iceland. J Volcanol Geotherm Res 391:106351

Eichelberger JC, Carrigan CR, Westrich HR, Price RH (1986) Non-explosive silicic volcanism. Nature 323(6089):598–602

Erdoğan M (1986) Nevşehir-Ürgup yöresi tüflerinin malzeme jeolojisi aÇısından araştırılması. Unpublished doctoral dissertation, Istanbul Technical University (ITU), Faculty of Mining, Istanbul

Erguler ZA, Ulusay R (2009) Water-induced variations in mechanical properties of clay-bearing rocks. Int J Rock Mech Min Sci 46(2): 355–370

Erguvanlı K, Yorulmaz M, Çılı F, Ahunbay Z, Erdoğan M (1989) Göreme yapısal koruma ve sağlamlaştırma projesi, E1 Nazar kilisesi, Istanbul Technical University (ITU). Faculty of Mining, Istanbul, p 46

Ersoy A, Atici U (2007) Correlation of P and S-Waves with Cutting Specific Energy and Dominant Properties of Volcanic and Carbonate Rocks. Rock Mech Rock Eng 40(5):491–504

Evans B, Fredrich JT, Wong T-f (1990) The brittle-ductile transition in rocks: Recent experimental and theoretical progress. The Brittle-Ductile Transition in Rocks. Geophys Monogr Ser 56:1–20

Fagereng Å, Biggs J (2019) New perspectives on 'geological strain rates' calculated from both naturally deformed and actively deforming rocks. J Struct Geol 125:100–110

Fakhimi A, Gharahbagh EA (2011) Discrete element analysis of the effect of pore size and pore distribution on the mechanical behavior of rock. Int J Rock Mech Min Sci 48(1):77–85

Farquharson J, Heap MJ, Varley NR, Baud P, Reuschlé T (2015) Permeability and porosity relationships of edifice-forming andesites: a combined field and laboratory study. J Volcanol Geotherm Res 297:52–68

Farquharson JI, Heap MJ, Baud P (2016) Strain-induced permeability increase in volcanic rock. Geophys Res Lett 43(22):11–603

Farquharson JI, Baud P, Heap MJ (2017) Inelastic compaction and permeability evolution in volcanic rock. Solid Earth 8(2):561

Farquharson JI, Wild B, Kushnir AR, Heap MJ, Baud P, Kennedy B (2019) Acid-induced dissolution of andesite: evolution of permeability and strength. J Geophys Res Solid Earth 124(1):257–273

Fazio M, Benson PM, Vinciguerra S (2017) On the generation mechanisms of fluid-driven seismic signals related to volcano-tectonics. Geophys Res Lett 44(2):734–742

Fener M, Ince I (2015) Effects of the freeze–thaw (F–T) cycle on the andesitic rocks (Sille-Konya/Turkey) used in construction building. J Afr Earth Sci 109:96–106

Forbes Inskip ND, Browning J, Meredith PG, Gudmundsson A (2020) Conditions for fracture arrest in layered rock sequences. Results Geophys Sci:100001

Fortin J, Stanchits S, Vinciguerra S, Guéguen Y (2011) Influence of thermal and mechanical cracks on permeability and elastic wave velocities in a basalt from Mt. Etna volcano subjected to elevated pressure. Tectonophysics 503(1-2):60–74

Frolova J, Ladygin VL, Rychagov S, Zukhubaya D (2014) Effects of hydrothermal alterations on physical and mechanical properties of rocks in the Kuril–Kamchatka island arc. Eng Geol 183:80–95

Frolova JV, Chernov MS, Rychagov SN, Ladygin VM, Sokolov VN, Kuznetsov RA (2020) The influence of hydrothermal argillization on the physical and mechanical properties of tuffaceous rocks: a case study from the Upper Pauzhetsky thermal field, Kamchatka. Bull Eng Geol Environ:1–17

Funatsu T, Seto M, Shimada H, Matsui K, Kuruppu M (2004) Combined effects of increasing temperature and confining pressure on the fracture toughness of clay bearing rocks. Int J Rock Mech Min Sci 41(6):927–938

Geshi N, Kusumoto S, Gudmundsson A (2012) Effects of mechanical layering of host rocks on dike growth and arrest. J Volcanol Geotherm Res 223:74–82

Ghorbani A, Revil A, Coperey A, Ahmed AS, Roque S, Heap MJ et al (2018) Complex conductivity of volcanic rocks and the geophysical mapping of alteration in volcanoes. J Volcanol Geotherm Res 357: 106–127

Giacomel P, Spagnuolo E, Nazzari M, Marzoli A, Passelegue F, Youbi N, Di Toro G (2018) Frictional Instabilities and Carbonation of Basalts Triggered by Injection of Pressurized H2O-and CO2-Rich Fluids. Geophys Res Lett 45(12):6032–6041

Glicken H (1996) Rockslide-debris avalanche of May 18, 1980, Mount St. Helens volcano, Washington (No. 96-677). US Geological Survey

Graue B, Siegesmund S, Middendorf B (2011) Quality assessment of replacement stones for the Cologne Cathedral: mineralogical and petrophysical requirements. Environ Earth Sci 63(7-8):1799–1822

Griffiths L, Heap MJ, Baud P, Schmittbuhl J (2017a) Quantification of microcrack characteristics and implications for stiffness and strength of granite. Int J Rock Mech Min Sci 100:138–150

Griffiths L, Heap MJ, Xu T, Chen CF, Baud P (2017b) The influence of pore geometry and orientation on the strength and stiffness of porous rock. J Struct Geol 96:149–160

Gudmundsson A (1987) Formation and mechanics of magma reservoirs in Iceland. Geophys J Int 91(1):27–41

Gudmundsson A (2002) Emplacement and arrest of sheets and dykes in central volcanoes. J Volcanol Geotherm Res 116(3-4):279–298

Gudmundsson A (2006) How local stresses control magma-chamber ruptures, dyke injections, and eruptions in composite volcanoes. Earth Sci Rev 79(1-2):1–31

Gudmundsson A (2009) Toughness and failure of volcanic edifices. Tectonophysics 471(1-2):27–35

Gudmundsson A (2011) Rock fractures in geological processes. Cambridge University Press

Gudmundsson A (2012) Strengths and strain energies of volcanic edifices: implications for eruptions, collapse calderas, and landslides. Nat Hazards Earth Syst Sci 12(7):2241–2258

Gudmundsson A (2017) The glorious geology of Iceland's golden circle (p. 334). Springer International Publishing, Cham

Gudmundsson A (2020) Volcanotectonics: Understanding the structure, deformation and dynamics of volcanoes. Cambridge University Press

Gupta AS, Rao KS (2000) Weathering effects on the strength and deformational behaviour of crystalline rocks under uniaxial compression state. Eng Geol 56(3-4):257–274

Hacker BR, Christie JM (1991) Experimental deformation of a glassy basalt. Tectonophysics 200(1-3):79–96

Handin J (1969) On the Coulomb-Mohr failure criterion. J Geophys Res 74(22):5343–5348

Harnett CE, Benson PM, Rowley P, Fazio M (2018a) Fracture and damage localization in volcanic edifice rocks from El Hierro, Stromboli and Tenerife. Sci Rep 8(1):1–8

Harnett CE, Thomas ME, Purvance MD, Neuberg J (2018b) Using a discrete element approach to model lava dome emplacement and collapse. J Volcanol GeothermRes 359:68–77

Harnett CE, Kendrick JE, Lamur A, Thomas ME, Stinton A, Wallace PA et al (2019) Evolution of mechanical properties of lava dome rocks across the 1995–2010 eruption of Soufrière Hills Volcano, Montserrat. Front Earth Sci 7:7

Hashiba K, Fukui K (2015) Effect of water on the deformation and failure of rock in uniaxial tension. Rock Mech Rock Eng 48(5):1751–1761

Hashiba K, Fukui K, Kataoka M (2019) Effects of water saturation on the strength and loading-rate dependence of andesite. Int J Rock Mech Min Sci 117:142–149

Hawkes I, Mellor M (1970) Uniaxial testing in rock mechanics laboratories. Eng Geol 4(3):179–285

Healy D, Rizzo RE, Cornwell DG, Farrell NJ, Watkins H, Timms NE et al (2017) FracPaQ: A MATLAB™ toolbox for the quantification of fracture patterns. J Struct Geol 95:1–16

Heap MJ, Kennedy BM (2016) Exploring the scale-dependent permeability of fractured andesite. Earth Planet Sci Lett 447:139–150

Heap MJ, Wadsworth FB (2016) Closing an open system: pore pressure changes in permeable edifice rock at high strain rates. J Volcanol Geotherm Res 315:40–50

Heap MJ, Vinciguerra S, Meredith PG (2009) The evolution of elastic moduli with increasing crack damage during cyclic stressing of a basalt from Mt. Etna volcano. Tectonophysics 471(1-2):153–160

Heap MJ, Baud P, Meredith PG, Vinciguerra S, Bell AF, Main IG (2011) Brittle creep in basalt and its application to time-dependent volcano deformation. Earth Planet Sci Lett 307(1-2):71–82

Heap MJ, Lavallée Y, Laumann A, Hess KU, Meredith PG, Dingwell DB (2012) How tough is tuff in the event of fire? Geology 40(4):311–314

Heap MJ, Lavallée Y, Petrakova L, Baud P, Reuschlé T, Varley NR, Dingwell DB (2014a) Microstructural controls on the physical and mechanical properties of edifice-forming andesites at Volcán de Colima, Mexico. J Geophys Res Solid Earth 119(4):2925–2963

Heap MJ, Xu T, Chen C-f (2014b) The influence of porosity and vesicle size on the brittle strength of volcanic rocks and magma. Bull Volcanol 76(9):856

Heap MJ, Baud P, Meredith PG, Vinciguerra S, Reuschlé T (2014c) The permeability and elastic moduli of tuff from Campi Flegrei, Italy: implications for ground deformation modelling. Solid Earth 5(1): 25–44

Heap MJ, Farquharson JI, Wadsworth FB, Kolzenburg S, Russell JK (2015a) Timescales for permeability reduction and strength recovery in densifying magma. Earth Planet Sci Lett 429:223–233

Heap MJ, Farquharson JI, Baud P, Lavallée Y, Reuschlé T (2015b) Fracture and compaction of andesite in a volcanic edifice. Bull Volcanol 77(6):55

Heap MJ, Kennedy BM, Pernin N, Jacquemard L, Baud P, Farquharson JI et al (2015c) Mechanical behaviour and failure modes in the

Whakaari (White Island volcano) hydrothermal system, New Zealand. J Volcanol Geotherm Res 295:26–42

Heap MJ, Wadsworth FB, Xu T, Chen CF (2016a) The strength of heterogeneous volcanic rocks: a 2D approximation. J Volcanol Geotherm Res 319:1–11

Heap MJ, Russell JK, Kennedy LA (2016b) Mechanical behaviour of dacite from Mount St. Helens (USA): A link between porosity and lava dome extrusion mechanism (dome or spine)? J Volcanol Geotherm Res 328:159–177

Heap MJ, Violay M, Wadsworth FB, Vasseur J (2017) From rock to magma and back again: the evolution of temperature and deformation mechanism in conduit margin zones. Earth Planet Sci Lett 463: 92–100

Heap MJ, Coats R, Chen CF, Varley N, Lavallée Y, Kendrick J et al (2018a) Thermal resilience of microcracked andesitic dome rocks. J Volcanol Geotherm Res 367:20–30

Heap MJ, Farquharson JI, Kushnir AR, Lavallée Y, Baud P, Gilg HA, Reuschlé T (2018b) The influence of water on the strength of Neapolitan Yellow Tuff, the most widely used building stone in Naples (Italy). Bull Volcanol 80(6):51

Heap M, Kushnir A, Griffiths L, Wadsworth F, Marmoni GM, Fiorucci M et al (2018c) Fire resistance of the Mt. Epomeo Green Tuff, a widely-used building stone on Ischia Island (Italy). Volcanica 1(1): 33–48

Heap MJ, Reuschlé T, Farquharson JI, Baud P (2018d) Permeability of volcanic rocks to gas and water. J Volcanol Geotherm Res 354:29–38

Heap MJ, Villeneuve M, Kushnir AR, Farquharson JI, Baud P, Reuschlé T (2019a) Rock mass strength and elastic modulus of the Buntsandstein: an important lithostratigraphic unit for geothermal exploitation in the Upper Rhine Graben. Geothermics 77:236–256

Heap MJ, Troll VR, Kushnir AR, Gilg HA, Collinson AS, Deegan FM et al (2019b) Hydrothermal alteration of andesitic lava domes can lead to explosive volcanic behaviour. Nat Commun 10(1):1–10

Heap MJ, Baud P, McBeck JA, Renard F, Carbillet L, Hall SA (2020a) Imaging strain localisation in porous andesite using digital volume correlation. J Volcanol Geotherm Res 107038

Heap MJ, Villeneuve M, Albino F, Farquharson JI, Brothelande E, Amelung F et al (2020b) Towards more realistic values of elastic moduli for volcano modelling. J Volcanol Geotherm Res 390: 106684

Heap MJ, Gravley DM, Kennedy BM, Gilg HA, Bertolett E, Barker SL (2020c) Quantifying the role of hydrothermal alteration in creating geothermal and epithermal mineral resources: The Ohakuri ignimbrite (Taupō Volcanic Zone, New Zealand). J Volcanol Geotherm Res 390:106703

Heidari M, Khanlari GR, Torabi-Kaveh M, Kargarian S, Saneie S (2014) Effect of porosity on rock brittleness. Rock Mech Rock Eng 47(2): 785–790

Hoek E, Brown ET (2019) The Hoek–Brown failure criterion and GSI–2018 edition. J Rock Mech Geotech Eng 11(3):445–463

Hoek E, Diederichs MS (2006) Empirical estimation of rock mass modulus. Int J Rock Mech Min Sci 43(2):203–215

Holohan EP, Sudhaus H, Walter TR, Schöpfer MP, Walsh JJ (2017) Effects of host-rock fracturing on elastic-deformation source models of volcano deflation. Sci Rep 7(1):1–12

Hornby AJ, Kendrick JE, Lamb OD, Hirose T, De Angelis S, von Aulock FW et al (2015) Spine growth and seismogenic faulting at Mt. Unzen, Japan. J Geophys Res Solid Earth 120(6):4034–4054

Hornby AJ, Lavallée Y, Kendrick JE, De Angelis S, Lamur A, Lamb OD et al (2019) Brittle-ductile deformation and tensile rupture of dome lava during inflation at Santiaguito, Guatemala. J Geophys Res Solid Earth 124(10):10107–10131

Hughes A, Kendrick JE, Salas G, Wallace PA, Legros F, Di Toro G, Lavallée Y (2020) Shear localisation, strain partitioning and frictional melting in a debris avalanche generated by volcanic flank collapse. J Struct Geol 140:104132

Hürlimann M, Garcia-Piera JO, Ledesma A (2000) Causes and mobility of large volcanic landslides: application to Tenerife, Canary Islands. J Volcanol Geotherm Res 103(1-4):121–134

Husen S, Smith RB, Waite GP (2004) Evidence for gas and magmatic sources beneath the Yellowstone volcanic field from seismic tomographic imaging. J Volcanol Geotherm Res 131(3-4):397–410

Ikari MJ, Wilckens FK, Saffer DM (2020) Implications of basement rock alteration in the Nankai Trough, Japan for subduction megathrust slip behavior. Tectonophysics 774:228275

Jackson MD, Marra F, Hay RL, Cawood C, Winkler EM (2005) The judicious selection and preservation of tuff and travertine building stone in ancient Rome. Archaeometry 47(3):485–510

Jaeger JC (1959) The frictional properties of joints in rock. Geofisica Pura Applicata 43(1):148–158

Kahraman S, Yeken T (2010) Electrical resistivity measurement to predict uniaxial compressive and tensile strength of igneous rocks. Bull Mater Sci 33(6):731–735

Karakuş A, Akatay M (2013) Determination of basic physical and mechanical properties of basaltic rocks from P-wave velocity. Nondestruct Test Eval 28(4):342–353

Karaman K, Kesimal A (2015) Evaluation of the influence of porosity on the engineering properties of volcanic rocks from the Eastern Black Sea Region: NE Turkey. Arab J Geosci 8(1):557–564

Kavanagh JL, Rogers BD, Boutelier D, Cruden AR (2017) Controls on sill and dyke-sill hybrid geometry and propagation in the crust: The role of fracture toughness. Tectonophysics 698:109–120

Kendrick JE, Smith R, Sammonds P, Meredith PG, Dainty M, Pallister JS (2013a) The influence of thermal and cyclic stressing on the strength of rocks from Mount St. Helens, Washington. Bull Volcanol 75(7): 728

Kendrick JE, Lavallée Y, Hess KU, Heap MJ, Gaunt HE, Meredith PG, Dingwell DB (2013b) Tracking the permeable porous network during strain-dependent magmatic flow. J Volcanol Geotherm Res 260: 117–126

Kendrick JE, Lavallée Y, Hirose T, Di Toro G, Hornby AJ, De Angelis S, Dingwell DB (2014) Volcanic drumbeat seismicity caused by stick-slip motion and magmatic frictional melting. Nat Geosci 7(6):438–442

Kendrick JE, Schaefer LN, Schauroth J, Bell AF, Lamb OD, Lamur A, ..., Kennedy BM (2021) Physical and mechanical rock properties of a heterogeneous volcano; the case of Mount Unzen, Japan. Solid Earth 12(3):633–664

Kennedy LA, Russell JK (2012) Cataclastic production of volcanic ash at Mount Saint Helens. Phys Chem Earth A/B/C 45:40–49

Kennedy LA, Russell JK, Nelles E (2009) Origins of Mount St. Helens cataclasites: experimental insights. Am Mineral 94(7):995–1004

Kennedy BM, Farquhar A, Hilderman R, Villeneuve MC, Heap MJ, Mordensky S et al (2020) Pressure Controlled Permeability in a Conduit Filled with Fractured Hydrothermal Breccia Reconstructed from Ballistics from Whakaari (White Island), New Zealand. Geosciences 10(4):138

Kereszturi G, Schaefer LN, Miller C, Mead S (2020) Hydrothermal Alteration on Composite Volcanoes–Mineralogy, Hyperspectral Imaging and Aeromagnetic Study of Mt Ruapehu, New Zealand. Geochem Geophys Geosyst:e2020GC009270

Kilburn CR (2003) Multiscale fracturing as a key to forecasting volcanic eruptions. J Volcanol Geotherm Res 125(3-4):271–289

Kilburn C (2012) Precursory deformation and fracture before brittle rock failure and potential application to volcanic unrest. J Geophys Res Solid Earth 117(B2)

Kilburn CR, Voight B (1998) Slow rock fracture as eruption precursor at Soufriere Hills volcano, Montserrat. Geophys Res Lett 25(19): 3665–3668

Kılıç A, Teymen A (2008) Determination of mechanical properties of rocks using simple methods. Bull Eng Geol Environ 67(2):237

Kolzenburg S, Heap M, Lavallée Y, Russell J, Meredith P, Dingwell DB (2012) Strength and permeability recovery of tuffisite-bearing andesite. Solid Earth 3(2):191–198

Komorowski JC, Jenkins S, Baxter PJ, Picquout A, Lavigne F, Charbonnier S et al (2013) Paroxysmal dome explosion during the Merapi 2010 eruption: Processes and facies relationships of associated high-energy pyroclastic density currents. J Volcanol Geotherm Res 261:260–294

Koulakov I, Gordeev EI, Dobretsov NL, Vernikovsky VA, Senyukov S, Jakovlev A, Jaxybulatov K (2013) Rapid changes in magma storage beneath the Klyuchevskoy group of volcanoes inferred from time-dependent seismic tomography. J Volcanol Geotherm Res 263:75–91

Kushnir AR, Martel C, Bourdier JL, Heap MJ, Reuschlé T, Erdmann S et al (2016) Probing permeability and microstructure: unravelling the role of a low-permeability dome on the explosivity of Merapi (Indonesia). J Volcanol Geotherm Res 316:56–71

Lamb OD, De Angelis S, Wall RJ, Lamur A, Varley NR, Reyes-Dávila G et al (2017) Seismic and experimental insights into eruption precursors at Volcán de Colima. Geophys Res Lett 44(12):6092–6100

Lamur A, Kendrick JE, Eggertsson GH, Wall RJ, Ashworth JD, Lavallée Y (2017) The permeability of fractured rocks in pressurised volcanic and geothermal systems. Sci Rep 7(1):1–9

Lavallée Y, Meredith PG, Dingwell DB, Hess KU, Wassermann J, Cordonnier B et al (2008) Seismogenic lavas and explosive eruption forecasting. Nature 453(7194):507–510

Lavallée Y, Varley NR, Alatorre-Ibargüengoitia MA, Hess KU, Kueppers U, Mueller S et al (2012a) Magmatic architecture of dome-building eruptions at Volcán de Colima, Mexico. Bull Volcanol 74(1):249–260

Lavallée Y, Mitchell TM, Heap MJ, Vasseur J, Hess KU, Hirose T, Dingwell DB (2012b) Experimental generation of volcanic pseudotachylytes: Constraining rheology. J Struct Geol 38:222–233

Lavallée Y, Benson PM, Heap MJ, Hess KU, Flaws A, Schillinger B et al (2013) Reconstructing magma failure and the degassing network of dome-building eruptions. Geology 41(4):515–518

Lavallée Y, Hirose T, Kendrick JE, De Angelis S, Petrakova L, Hornby AJ, Dingwell DB (2014) A frictional law for volcanic ash gouge. Earth Planet Sci Lett 400:177–183

Lavallée Y, Heap MJ, Kendrick JE, Kueppers U, Dingwell DB (2019) The fragility of Volcán de Colima—a material constraint. In: Volcán de Colima. Springer, Berlin, Heidelberg, pp 241–266

Legros F, Cantagrel JM, Devouard B (2000) Pseudotachylyte (frictionite) at the base of the Arequipa volcanic landslide deposit (Peru): implications for emplacement mechanisms. J Geol 108(5):601–611

Li Z, Fortin J, Nicolas A, Deldicque D, Guéguen Y (2019) Physical and mechanical properties of thermally cracked andesite under pressure. Rock Mech Rock Eng 52(10):3509–3529

Lipman PW, Mullineaux DR (Eds) (1982) The 1980 eruptions of Mount St. Helens, Washington (Vol. 1250). US Department of the Interior, US Geological Survey

Loaiza S, Fortin J, Schubnel A, Guéguen Y, Vinciguerra S, Moreira M (2012) Mechanical behavior and localized failure modes in a porous basalt from the Azores. Geophys Res Lett 39(19)

Lockner D (1993) The role of acoustic emission in the study of rock fracture. Int J Rock Mech Min Sci Geomech Abstr 30(7):883–899

Lockner DA, Morrow CA (2008) Energy dissipation in Calico Hills tuff due to pore collapse. AGUFM 2008:T51A–T1856A

López DL, Williams SN (1993) Catastrophic volcanic collapse: relation to hydrothermal processes. Science 260(5115):1794–1796

Louis L, Baud P, Wong T-f (2007) Characterization of pore-space heterogeneity in sandstone by X-ray computed tomography. Geol Soc Lond, Spec Publ 284(1):127–146

Ma L, Daemen JJK (2006) An experimental study on creep of welded tuff. Int J Rock Mech Min Sci 43(2):282–291

Mair K, Frye KM, Marone C (2002) Influence of grain characteristics on the friction of granular shear zones. J Geophys Res Solid Earth 107(B10):ECV-4

Malik A, Chakraborty T, Rao KS, Kumar D (2017) Experiments to determine static and dynamic tensile strength of deccan trap rocks, India. Procedia Eng 191:946–953

Marmoni GM, Martino S, Heap MJ, Reuschlé T (2017) Gravitational slope-deformation of a resurgent caldera: New insights from the mechanical behaviour of Mt. Nuovo tuffs (Ischia Island, Italy). J Volcanol Geotherm Res 345:1–20

Martin RJ, Boyd PJ, Noel JS, Price RH (1994) Bulk and mechanical properties of the Paintbrush Tuff recovered from Borehole USW NRG-6: data report (No. SAND—93-4020). Sandia National Labs., Albuquerque, NM (United States)

Martin RJ, Noel JS, Boyd PJ, Price RH (1997) Creep and static fatigue of welded tuff from Yucca Mountain, Nevada. Int J Rock Mech Min Sci 34(3-4):190–1e1

McBeck JA, Cordonnier B, Vinciguerra S, Renard F (2019) Volumetric and shear strain localization in Mt. Etna basalt. Geophys Res Lett 46(5):2425–2433

McNutt SR (1996) Seismic monitoring and eruption forecasting of volcanoes: a review of the state-of-the-art and case histories. Monit Mitig Volcano Hazards:99–146

McNutt SR, Roman DC (2015) Volcanic seismicity. In: The Encyclopedia of Volcanoes. Academic Press, pp 1011–1034

Menéndez B, Zhu W, Wong TF (1996) Micromechanics of brittle faulting and cataclastic flow in Berea sandstone. J Struct Geol 18(1):1–16

Meredith PG, Atkinson BK (1985) Fracture toughness and subcritical crack growth during high-temperature tensile deformation of Westerly granite and Black gabbro. Phys Earth Planet Inter 39(1):33–51

Meredith PG, Atkinson BK, Hillman NB (1981) KIC measurements on rock using a short-rod apparatus, In: Process in Experimental Petrology, 5, 297-298, NERC Publications Series D, No. 18

Mogi K (2007) Experimental rock mechanics (Vol. 3). CRC Press

Mollo S, Tuccimei P, Heap MJ, Vinciguerra S, Soligo M, Castelluccio M et al (2011) Increase in radon emission due to rock failure: An experimental study. Geophys Res Lett 38(14)

Montanaro C, Scheu B, Mayer K, Orsi G, Moretti R, Isaia R, Dingwell DB (2016) Experimental investigations on the explosivity of steam-driven eruptions: A case study of Solfatara volcano (Campi Flegrei). J Geophys Res Solid Earth 121(11):7996–8014

Moon K, Yang SB (2020) Cohesion and Internal Friction Angle Estimated from Brazilian Tensile Strength and Unconfined Compressive Strength of Volcanic Rocks in Jeju Island. J Korean Geotech Soc 36(2):17–28

Mordensky SP, Villeneuve MC, Kennedy BM, Heap MJ, Gravley DM, Farquharson JI, Reuschlé T (2018) Physical and mechanical property relationships of a shallow intrusion and volcanic host rock, Pinnacle Ridge, Mt. Ruapehu, New Zealand. J Volcanol Geotherm Res 359:1–20

Mordensky SP, Heap MJ, Kennedy BM, Gilg HA, Villeneuve MC, Farquharson JI, Gravley DM (2019) Influence of alteration on the mechanical behaviour and failure mode of andesite: implications for shallow seismicity and volcano monitoring. Bull Volcanol 81(8):44

Mueller S, Scheu B, Spieler O, Dingwell DB (2008) Permeability control on magma fragmentation. Geology 36(5):399–402

Nara Y, Hiroyoshi N, Yoneda T, Kaneko K (2010a) Effects of relative humidity and temperature on subcritical crack growth in igneous rock. Int J Rock Mech Min Sci 47(4):640–646

Nara Y, Takada M, Mori D, Owada H, Yoneda T, Kaneko K (2010b) Subcritical crack growth and long-term strength in rock and cementitious material. Int J Fract 164(1):57–71

Nara Y, Meredith PG, Yoneda T, Kaneko K (2011) Influence of macro-fractures and micro-fractures on permeability and elastic wave velocities in basalt at elevated pressure. Tectonophysics 503(1-2):52–59

Nara Y, Morimoto K, Hiroyoshi N, Yoneda T, Kaneko K, Benson PM (2012) Influence of relative humidity on fracture toughness of rock: implications for subcritical crack growth. Int J Solids Struct 49(18):2471–2481

Nicolas A, Lévy L, Sissmann O, Li Z, Fortin J, Gibert B, Sigmundsson F (2020) Influence of hydrothermal alteration on the elastic behaviour and failure of heat-treated andesite from Guadeloupe. Geophys J Int 223:2038–2053

Niemeijer A, Di Toro G, Nielsen S, Di Felice F (2011) Frictional melting of gabbro under extreme experimental conditions of normal stress, acceleration, and sliding velocity. J Geophys Res Solid Earth 116(B7)

Okubo CH (2004) Rock mass strength and slope stability of the Hilina slump, Kīlauea volcano, Hawai'i. J Volcanol Geotherm Res 138(1-2):43–76

Okubo CH (2014) Brittle deformation and slope failure at the North Menan butte tuff cone, eastern Snake River plain, Idaho. J Volcanol Geotherm Res 278:86–95

Okubo S, Chu SY (1994) Uniaxial compression creep of Tage and Oya tuff in air-dried and water-saturated conditions. J Soc Mater Sci 43(490):819–825

Ougier-Simonin A, Fortin J, Guéguen Y, Schubnel A, Bouyer F (2011) Cracks in glass under triaxial conditions. Int J Eng Sci 49(1):105–121

Parisio F, Vinciguerra S, Kolditz O, Nagel T (2019) The brittle-ductile transition in active volcanoes. Sci Rep 9(1):1–10

Parisio F, Lehmann C, Nagel T (2020) A model of failure and localization of basalt at temperature and pressure conditions spanning the brittle-ductile transition. J Geophys Res Solid Earth:e2020JB020539

Patanè D, Barberi G, Cocina O, De Gori P, Chiarabba C (2006) Time-resolved seismic tomography detects magma intrusions at Mount Etna. Science 313(5788):821–823

Paterson MS, Olgaard DL (2000) Rock deformation tests to large shear strains in torsion. J Struct Geol 22(9):1341–1358

Paterson MS, Wong T-f (2005) Experimental rock deformation-the brittle field. Springer Science & Business Media

Perras MA, Diederichs MS (2014) A review of the tensile strength of rock: concepts and testing. Geotech Geol Eng 32(2):525–546

Persson BNJ (2000) Lubricated Friction Dynamics. In: Sliding Friction. NanoScience and Technology. Springer, Berlin, Heidelberg

Peruzzetto M, Komorowski JC, Le Friant A, Rosas-Carbajal M, Mangeney A, Legendre Y (2019) Modeling of partial dome collapse of La Soufrière of Guadeloupe volcano: implications for hazard assessment and monitoring. Sci Rep 9(1):1–15

Pola A, Crosta GB, Fusi N, Castellanza R (2014) General characterization of the mechanical behaviour of different volcanic rocks with respect to alteration. Eng Geol 169:1–13

Price RH (1983) Analysis of the rock mechanics properties of volcanic tuff units from Yucca Mountain, Nevada Test Site. Sandia National Labs., Albuquerque, NM (United States)

Price RH, Jones AK (1982) Uniaxial and triaxial compression test series on Calico Hills tuff (No. SAND—82-1314). Sandia National Labs., Albuquerque, NM (United States)

Reid ME (2004) Massive collapse of volcano edifices triggered by hydrothermal pressurization. Geology 32(5):373–376

Reid ME, Christian SB, Brien DL (2000) Gravitational stability of three-dimensional stratovolcano edifices. J Geophys Res Solid Earth 105(B3):6043–6056

Reid ME, Sisson TW, Brien DL (2001) Volcano collapse promoted by hydrothermal alteration and edifice shape, Mount Rainier, Washington. Geology 29(9):779–782

Revil A, Coperey A, Heap MJ, Carbillet L (2020) A geophysical index to map alteration, permeability, and mechanical properties within volcanoes. Application to the soft volcanic rocks from Whakaari/White Island (New Zealand). J Volcanol Geotherm Res:106945

Rivalta E, Taisne B, Bunger AP, Katz RF (2015) A review of mechanical models of dike propagation: Schools of thought, results and future directions. Tectonophysics 638:1–42

Rizzo RE, Healy D, Heap MJ, Farrell NJ (2018) Detecting the Onset of Strain Localization Using Two-Dimensional Wavelet Analysis on Sandstone Deformed at Different Effective Pressures. J Geophys Res Solid Earth 123(12):10–460

Rocchi V, Sammonds PR, Kilburn CR (2003) Flow and fracture maps for basaltic rock deformation at high temperatures. J Volcanol Geotherm Res 120(1-2):25–42

Rocchi V, Sammonds PR, Kilburn CRJ (2004) Fracturing of Etnean and Vesuvian rocks at high temperatures and low pressures. Journal of Volcanology and Geothermal Research 132(2–3):137–157

Rodríguez-Losada JA, Hernández-Gutiérrez LE, Olalla C, Perucho A, Serrano A, Eff-Darwich A (2009) Geomechanical parameters of intact rocks and rock masses from the Canary Islands: implications on their flank stability. J Volcanol Geotherm Res 182(1-2):67–75

Rosas-Carbajal M, Komorowski JC, Nicollin F, Gibert D (2016) Volcano electrical tomography unveils edifice collapse hazard linked to hydrothermal system structure and dynamics. Sci Rep 6:29899

Rosas-Carbajal M, Jourde K, Marteau J, Deroussi S, Komorowski JC, Gibert D (2017) Three-dimensional density structure of La Soufrière de Guadeloupe lava dome from simultaneous muon radiographies and gravity data. Geophys Res Lett 44(13):6743–6751

Rowley P, Benson P, Bean C (2020) Deformation controlled Long-Period seismicity in low cohesion volcanic sediments. EarthArXiv. https://doi.org/10.31223/osf.io/7rkzv

Rutter EH (1986) On the nomenclature of mode of failure transitions in rocks. Tectonophysics 122(3-4):381–387

Ryan AG, Heap MJ, Russell JK, Kennedy LA, Clynne MA (2020) Cyclic shear zone cataclasis and sintering during lava dome extrusion: Insights from Chaos Crags, Lassen Volcanic Center (USA). J Volcanol Geotherm Res 106935

Sammis CG, Ashby MF (1986) The failure of brittle porous solids under compressive stress states. Acta Metall 34(3):511–526

Schaefer LN, Oommen T, Corazzato C, Tibaldi A, Escobar-Wolf R, Rose WI (2013) An integrated field-numerical approach to assess slope stability hazards at volcanoes: the example of Pacaya, Guatemala. Bull Volcanol 75(6):720

Schaefer LN, Kendrick JE, Oommen T, Lavallée Y, Chigna G (2015) Geomechanical rock properties of a basaltic volcano. Front Earth Sci 3:29

Scheidl KS, Schaeffer AK, Petrishcheva E, Habler G, Fischer FD, Schreuer J, Abart R (2014) Chemically induced fracturing in alkali feldspar. Phys Chem Miner 41(1):1–16

Scheu B, Kueppers U, Mueller S, Spieler O, Dingwell DB (2008) Experimental volcanology on eruptive products of Unzen volcano. J Volcanol Geotherm Res 175(1-2):110–119

Scholz CH (1968) Experimental study of the fracturing process in brittle rock. J Geophys Res 73(4):1447–1454

Schubnel A, Benson PM, Thompson BD, Hazzard JF, Young RP (2006) Quantifying damage, saturation and anisotropy in cracked rocks by inverting elastic wave velocities. In: Rock Damage and Fluid Transport, Part I. Birkhäuser, Basel, pp 947–973

Schultz R (1995) Limits on strength and deformation properties of jointed basaltic rock masses. Rock Mech Rock Eng 28(1):1–15

Schultz RA, Li Q (1995) Uniaxial strength testing of non-welded Calico Hills tuff, Yucca Mountain, Nevada. Eng Geol 40(3-4):287–299

Shea T, Houghton BF, Gurioli L, Cashman KV, Hammer JE, Hobden BJ (2010) Textural studies of vesicles in volcanic rocks: an integrated methodology. J Volcanol Geotherm Res 190(3-4):271–289

Shimada M (1986) Mechanism of deformation in a dry porous basalt at high pressures. Tectonophysics 121(2-4):153–173

Shimada M (2000) Mechanical behaviour of rocks under high pressure conditions, vol 2. CRC Press

Shimada M, Ito K, Cho A (1989) Ductile behavior of a fine-grained porous basalt at room temperature and pressures to 3 GPa. Phys Earth Planet Inter 55(3-4):361–373

Shimamoto T (1994) A new rotary-shear high-speed frictional testing machine: its basic design and scope of research. J Tectonic Res Group Jpn 39:65–78

Singh RN, Pathan AG (1988) Fracture toughness of some British rocks by diametral loading of discs. Min Sci Technol 6(2):179–190

Siratovich PA, Heap MJ, Villeneuve MC, Cole JW, Reuschlé T (2014) Physical property relationships of the Rotokawa Andesite, a significant geothermal reservoir rock in the Taupo Volcanic Zone, New Zealand. Geotherm Energy 2(1):10

Siratovich PA, von Aulock FW, Lavallée Y, Cole JW, Kennedy BM, Villeneuve MC (2015) Thermoelastic properties of the Rotokawa Andesite: a geothermal reservoir constraint. J Volcanol Geotherm Res 301:1–13

Siratovich PA, Heap MJ, Villeneuve MC, Cole JW, Kennedy BM, Davidson J, Reuschlé T (2016) Mechanical behaviour of the Rotokawa Andesites (New Zealand): Insight into permeability evolution and stress-induced behaviour in an actively utilised geothermal reservoir. Geothermics 64:163–179

Smith R, Sammonds PR, Kilburn CR (2009) Fracturing of volcanic systems: experimental insights into pre-eruptive conditions. Earth Planet Sci Lett 280(1-4):211–219

Smith R, Sammonds PR, Tuffen H, Meredith PG (2011) Evolution of the mechanics of the 2004–2008 Mt. St. Helens lava dome with time and temperature. Earth Planet Sci Lett 307(1-2):191–200

Sosio R, Crosta GB, Hungr O (2012) Numerical modeling of debris avalanche propagation from collapse of volcanic edifices. Landslides 9(3):315–334

Stanchits S, Vinciguerra S, Dresen G (2006) Ultrasonic velocities, acoustic emission characteristics and crack damage of basalt and granite. Pure Appl Geophys 163(5-6):975–994

Tembe S, Baud P, Wong T-f (2008) Stress conditions for the propagation of discrete compaction bands in porous sandstone. J Geophys Res Solid Earth 113(B9)

Topal T, Doyuran V (1997) Engineering geological properties and durability assessment of the Cappadocian tuff. Eng Geol 47(1-2):175–187

Topal T, Sözmen B (2003) Deterioration mechanisms of tuffs in Midas monument. Eng Geol 68(3-4):201–223

Toramaru A (1990) Measurement of bubble size distributions in vesiculated rocks with implications for quantitative estimation of eruption processes. J Volcanol Geotherm Res 43(1-4):71–90

Török A, Gálos M, Kocsanyi-Kopecsko K (2004) Experimental weathering of rhyolite tuff building stones and the effect of an organic polymer conserving agent. In: Stone Decay: Its Causes and Controls, pp 109–127

Tuğrul A, Gürpinar O (1997) A proposed weathering classification for basalts and their engineering properties (Turkey). Bull Eng Geol Environ 55(1):139–149

Tuncay E (2009) Rock rupture phenomenon and pillar failure in tuffs in the Cappadocia region (Turkey). Int J Rock Mech Min Sci 46(8): 1253–1266

Tuncay E, Özcan NT, Kalender A (2019) An approach to predict the length-to-diameter ratio of a rock core specimen for uniaxial compression tests. Bull Eng Geol Environ 78(7):5467–5482

Tutluoglu L, Keles C (2011) Mode I fracture toughness determination with straight notched disk bending method. Int J Rock Mech Min Sci 48(8):1248–1261

Ündül Ö, Er S (2017) Investigating the effects of micro-texture and geomechanical properties on the abrasiveness of volcanic rocks. Eng Geol 229:85–94

Vajdova V, Baud P, Wong T-f (2004) Compaction, dilatancy, and failure in porous carbonate rocks. J Geophys Res Solid Earth 109(B5)

van Wyk de Vries B, Francis PW (1997) Catastrophic collapse at stratovolcanoes induced by gradual volcano spreading. Nature 387(6631): 387–390

van Wyk de Vries B, Matela R (1998) Styles of volcano-induced deformation: numerical models of substratum flexure, spreading and extrusion. J Volcanol Geotherm Res 81(1-2):1–18

van Wyk de Vries B, Kerle N, Petley D (2000) Sector collapse forming at Casita volcano, Nicaragua. Geology 28(2):167–170

van Wyk de Vries B, Self S, Francis PW, Keszthelyi L (2001) A gravitational spreading origin for the Socompa debris avalanche. J Volcanol Geotherm Res 105(3):225–247

Vásárhelyi B, Ván P (2006) Influence of water content on the strength of rock. Eng Geol 84(1-2):70–74

Vasseur J, Wadsworth FB, Lavallée Y, Hess KU, Dingwell DB (2013) Volcanic sintering: timescales of viscous densification and strength recovery. Geophys Res Lett 40(21):5658–5664

Vasseur J, Wadsworth FB, Lavallée Y, Bell AF, Main IG, Dingwell DB (2015) Heterogeneity: the key to failure forecasting. Sci Rep 5(1):1–7

Vasseur J, Wadsworth FB, Heap MJ, Main IG, Lavallée Y, Dingwell DB (2017) Does an inter-flaw length control the accuracy of rupture forecasting in geological materials? Earth Planet Sci Lett 475:181–189

Vinciguerra S, Trovato C, Meredith PG, Benson PM (2005) Relating seismic velocities, thermal cracking and permeability in Mt. Etna and Iceland basalts. Int J Rock Mech Min Sci 42(7-8):900–910

Violay M, Gibert B, Mainprice D, Evans B, Dautria JM, Azais P, Pezard P (2012) An experimental study of the brittle-ductile transition of basalt at oceanic crust pressure and temperature conditions. J Geophys Res Solid Earth 117(B3)

Violay M, Di Toro G, Gibert B, Nielsen S, Spagnuolo E, Del Gaudio P et al (2014) Effect of glass on the frictional behavior of basalts at seismic slip rates. Geophys Res Lett 41(2):348–355

Violay M, Gibert B, Mainprice D, Burg JP (2015a) Brittle versus ductile deformation as the main control of the deep fluid circulation in oceanic crust. Geophys Res Lett 42(8):2767–2773

Violay M, Di Toro G, Nielsen S, Spagnuolo E, Burg JP (2015b) Thermo-mechanical pressurization of experimental faults in cohesive rocks during seismic slip. Earth Planet Sci Lett 429:1–10

Voight B (1988) A method for prediction of volcanic eruptions. Nature 332(6160):125–130

Voight B (1989) A relation to describe rate-dependent material failure. Science 243(4888):200–203

Voltolini M, Zandomeneghi D, Mancini L, Polacci M (2011) Texture analysis of volcanic rock samples: quantitative study of crystals and vesicles shape preferred orientation from X-ray microtomography data. J Volcanol Geotherm Res 202(1-2):83–95

Walker RJ, Holdsworth RE, Armitage PJ, Faulkner DR (2013) Fault zone permeability structure evolution in basalts. Geology 41(1):59–62

Walter TR, Harnett CE, Varley N, Bracamontes DV, Salzer J, Zorn EU, Thomas ME (2019) Imaging the 2013 explosive crater excavation and new dome formation at Volcán de Colima with TerraSAR-X, time-lapse cameras and modelling. J Volcanol GeothermRes 369: 224–237

Wang B, Chen Y, Wong T-f (2008) A discrete element model for the development of compaction localization in granular rock. J Geophys Res Solid Earth 113(B3)

Watters RJ, Zimbelman DR, Bowman SD, Crowley JK (2000) Rock mass strength assessment and significance to edifice stability, Mount Rainier and Mount Hood, Cascade Range volcanoes. Pure Appl Geophys 157(6-8):957–976

Weaver J, Eggertsson GH, Utley JE, Wallace PA, Lamur A, Kendrick JE et al (2020) Thermal liability of hyaloclastite in the Krafla geothermal reservoir, Iceland: the impact of phyllosilicates on permeability and rock strength. Geofluids.

Wedekind W, López-Doncel R, Dohrmann R, Kocher M, Siegesmund S (2013) Weathering of volcanic tuff rocks caused by moisture expansion. Environ Earth Sci 69(4):1203–1224

Weydt LM, Ramírez-Guzmán ÁA, Pola A, Lepillier B, Kummerow J, Mandrone G et al (2020) Petrophysical and mechanical rock property database of the Los Humeros and Acoculco geothermal fields (Mexico). Earth Syst Sci Data Discuss:1–39

Whitney DL, Broz M, Cook RF (2007) Hardness, toughness, and modulus of some common metamorphic minerals. Am Mineral 92(2-3): 281–288

Wiederhorn SM (1969) Fracture surface energy of glass. J Am Ceram Soc 52(2):99–105

Wilson JE, Goodwin LB, Lewis CJ (2003) Deformation bands in nonwelded ignimbrites: Petrophysical controls on fault-zone deformation and evidence of preferential fluid flow. Geology 31(10): 837–840

Wong T-f, Baud P (1999) Mechanical compaction of porous sandstone. Oil Gas Sci Technol 54(6):715–727

Wong T-f, Baud P (2012) The brittle-ductile transition in porous rock: A review. J Struct Geol 44:25–53

Wong T-f, David C, Zhu W (1997) The transition from brittle faulting to cataclastic flow in porous sandstones: Mechanical deformation. J Geophys Res Solid Earth 102(B2):3009–3025

Wright HM, Cashman KV, Gottesfeld EH, Roberts JJ (2009) Pore structure of volcanic clasts: Measurements of permeability and electrical conductivity. Earth Planet Sci Lett 280(1-4):93–104

Wyering LD, Villeneuve MC, Wallis IC, Siratovich PA, Kennedy BM, Gravley DM, Cant JL (2014) Mechanical and physical properties of hydrothermally altered rocks, Taupo Volcanic Zone, New Zealand. J Volcanol Geotherm Res 288:76–93

Yasar S, Komurlu E (2020) Water saturation induced changer in the indirect (Brazilian) tensile strength and the failure mode of some igneous rock materials. Geosci Eng 66:60–68

Yassaghi A, Salari-Rad H, Kanani-Moghadam H (2005) Geomechanical evaluations of Karaj tuffs for rock tunnelling in Tehran–Shomal Freeway, Iran. Eng Geol 77(1):83–98

Yavuz AB (2012) Durability assessment of the AlaÇatı tuff (Izmir) in western Turkey. Environ Earth Sci 67(7):1909–1925

Yavuz AB, Kaputoglu SA, Çolak M, Tanyu BF (2017) Durability assessments of rare green andesites widely used as building stones in Buca (Izmir), Turkey. Environ Earth Sci 76(5):211

Ye GL, Nishimura T, Zhang F (2015) Experimental study on shear and creep behaviour of green tuff at high temperatures. Int J Rock Mech Min Sci 79:19–28

Zhan Y, Gregg PM (2019) How Accurately Can We Model Magma Reservoir Failure With Uncertainties in Host Rock Rheology? J Geophys Res Solid Earth 124(8):8030–8042

Zhang J, Wong TF, Davis DM (1990) Micromechanics of pressure-induced grain crushing in porous rocks. J Geophys Res Solid Earth 95(B1):341–352

Zhang L, He C, Liu Y, Lin J (2017) Frictional properties of the South China Sea oceanic basalt and implications for strength of the Manila subduction seismogenic zone. Mar Geol 394:16–29

Zhu W, Baud P, Wong T-f (2010) Micromechanics of cataclastic pore collapse in limestone. J Geophys Res Solid Earth 115(B4)

Zhu W, Baud P, Vinciguerra S, Wong T-f (2011) Micromechanics of brittle faulting and cataclastic flow in Alban Hills tuff. J Geophys Res Solid Earth 116(B6)

Zhu W, Baud P, Vinciguerra S, Wong T-f (2016) Micromechanics of brittle faulting and cataclastic flow in Mount Etna basalt. J Geophys Res Solid Earth 121(6):4268–4289

Zoback MD, Byerlee JD (1975) The effect of microcrack dilatancy on the permeability of Westerly granite. J Geophys Res 80(5):752–755

Zorn EU, Rowe MC, Cronin SJ, Ryan AG, Kennedy LA, Russell JK (2018) Influence of porosity and groundmass crystallinity on dome rock strength: a case study from Mt. Taranaki, New Zealand. Bull Volcanol 80(4):35